



**HAL**  
open science

# AC Connection of Wind Farms to Transmission System : from Grid-Following to Grid-Forming

Artur Avazov

## ► To cite this version:

Artur Avazov. AC Connection of Wind Farms to Transmission System : from Grid-Following to Grid-Forming. Electric power. Centrale Lille Institut; Katholieke universiteit te Leuven (1970-..). Faculteit Geneeskunde, 2022. English. NNT : 2022CLIL0024 . tel-04074095

**HAL Id: tel-04074095**

**<https://theses.hal.science/tel-04074095v1>**

Submitted on 19 Apr 2023

**HAL** is a multi-disciplinary open access archive for the deposit and dissemination of scientific research documents, whether they are published or not. The documents may come from teaching and research institutions in France or abroad, or from public or private research centers.

L'archive ouverte pluridisciplinaire **HAL**, est destinée au dépôt et à la diffusion de documents scientifiques de niveau recherche, publiés ou non, émanant des établissements d'enseignement et de recherche français ou étrangers, des laboratoires publics ou privés.



**KU LEUVEN**



**Centrale Lille**

**THESE**

présentée en vue  
d'obtenir le grade de

**DOCTEUR**

en

Spécialité: Génie Électrique

par

**Artur AVAZOV**

**DOCTORAT délivré conjointement par CENTRALE LILLE et KU Leuven**

Titre de la thèse:

**AC Connection of Wind Farms to Transmission System: from Grid-Following to Grid-Forming**

**Connexion en AC de grandes fermes éoliennes au réseau de transport: d'un raccordement en source de courant au raccordement en source de tension**

Soutenue le 08 Décembre 2022 devant le jury d'examen:

<b>Président</b>	Serge Pierfederici, Professor, Ecole Nationale Supérieure d'Electricité et de Mécanique (ENSEM)
<b>Rapporteur</b>	Sibylle Dieckerhoff, Professor, Berlin Institute of Technology
<b>Rapporteur</b>	Nicolaos Cutululis, Professor, Technical University of Denmark
<b>Examineur</b>	Dirk Van Hertem, Associate Professor, KU Leuven
<b>Invité</b>	Hendrik Van Brussel, Professor, KU Leuven
<b>Invité</b>	Frédéric Colas, Research Engineer, Arts et Métiers ParisTech
<b>Directeur de thèse</b>	Xavier Guillaud, Professor, Centrale Lille Institut
<b>Co-directeur de thèse</b>	Jef Beerten, Associate Professor, KU Leuven

Thèse préparée dans le Laboratoire L2EP  
Ecole Doctorale ENGSYS 632



This PhD is financially supported by the foundation I-SITE Université Lille Nord – Europe in a joint PhD collaboration with KU Leuven.

# Acknowledgement

This thesis is the research outcome of a four-year PhD program which was conducted in a joint collaboration between Centrale Lille and KU Leuven. The end of this journey has been reached thanks to a significant number of people, each of whom contributed to my progress at different times in this period.

Firstly, I would like to express enormous gratitude to my supervisors Prof. Xavier Guillaud, Prof. Jef Beerten and Dr. Frédéric Colas for giving me the opportunity to start the PhD program, for guiding me, for providing valuable feedback. I believe that your invaluable input allowed me to gain skills that will help me to grow professionally in a chosen field. Additionally, I am full of gratitude to Prof. Xavier Guillaud for answering my weekend e-mails and motivating me to speak French during our meetings.

I acknowledge that the financial support for this PhD program has been received from the foundation I-SITE Université Lille Nord – Europe (ULNE).

I am highly grateful to the members of the examination committee who agreed to spend their precious time on reading this thesis and provided me with their comments to improve the thesis quality. Thank you, Prof. Dirk Van Hertem, Prof. Sibylle Dieckerhoff, Prof. Nicolaos Cutululis, Prof. Serge Pierfederici and Prof. Hendrik Van Brussel.

Additionally, I would like to thank Prof. Cutululis for sharing the data of the wind power plant for a case study, Prof. Johan Meyers and Luca Lanzilao from KU Leuven for letting me use the wind distribution modelling tool you have designed. This has helped me a lot to get valuable and realistic results for the third chapter of the thesis.

Special thanks go to the permanent and temporary L2EP and ENSAM members I was lucky enough to get acquainted with: Ebrahim, Taoufik, Nnaemeka, Martin, Pierre, Quentin, Ragav, François, Shiyi, Moez, Riad, Hicham and Amine. You were always ready to share your feedback on my work and discuss an interesting topic. Also, teşekkürler, Özgür, for always helping me to unravel the administrative and day-to-day issues at KU Leuven.

A huge thanks to my family, my mother and my beloved wife, Leisian, for your endless love, your encouragement and support.

Artur Avazov

December 2022

## Outline

Acknowledgement .....	iv
List of figures.....	vii
List of tables .....	xi
Résumé étendu.....	1
Introduction.....	5
1. Background .....	5
2. Current context and motivation .....	6
3. Thesis objectives and contributions .....	8
4. Outline of the thesis .....	9
5. List of publications .....	10
1. Modelling and control of a grid-forming wind turbine .....	11
1.1. Classification of converter controls .....	11
1.1.1. Power control with a converter .....	11
1.1.2. Grid-following control .....	13
1.1.3. Grid-forming control .....	16
1.2. Wind turbine modelling .....	24
1.2.1. Aerodynamic model .....	25
1.2.2. Mechanical model .....	26
1.2.3. Generator model.....	28
1.2.4. Turbine control.....	30
1.3. Control of a B2B converter in a Type-IV wind turbine.....	31
1.3.1. Classical control for a grid-following wind turbine.....	31
1.3.2. Control strategies for a grid-forming wind turbine .....	33
Conclusions.....	41
2. Electromechanical couplings in a grid-forming wind turbine .....	42
2.1. Influence of the wind turbine dynamics on the grid-forming control.....	42
2.2. Impact of the grid-forming control on mechanical structure of the wind turbine.....	47
2.3. Mitigation of torsional vibrations in a grid-forming wind turbine.....	51
2.3.1. Methods for vibration damping in a grid-forming wind turbine.....	51
2.3.2. Comparison of damping methods efficiency .....	55
2.4. Analysis of the damping based on the input shaping method.....	57

2.4.1. Impact of the DC bus voltage controller on damping efficiency .....	57
2.4.2. Minimization of the negative effect of the vibration damping .....	59
2.4.3. Robustness against parametric variations .....	65
Conclusions .....	69
3. Aggregation of a grid-forming wind power plant.....	70
3.1. Types of dynamic equivalent models.....	70
3.1.1. Multi-Machine equivalent Model (MMM) .....	70
3.1.2. Single-machine equivalent model .....	78
3.2. Wind distribution modelling .....	78
3.2.1. General description .....	78
3.2.2. Application of the wind distribution model to the case study WPP .....	81
3.3. Clustering algorithm .....	89
3.3.1. Description of the clustering algorithm.....	89
3.3.2. Selection of the optimal number of clusters.....	91
3.4. Algorithm for determining the optimal number of clusters as a function of wind conditions .....	96
3.4.1. Selection of the optimal number of clusters for one wind direction .....	97
3.4.2. Generalization of the algorithm .....	98
3.4.3. Algorithm verification for all wind directions and wind speeds.....	99
Conclusions.....	105
General conclusion .....	106
Future perspectives .....	108
References.....	110

## List of figures

Figure 1. 2030 wind energy installed capacity by country according to Central Scenario in the EU [28] .....	7
Figure 1.1. VSC connected to the grid .....	11
Figure 1.2. Single-line diagram .....	12
Figure 1.3. Phasor representation of the system.....	12
Figure 1.4. Active power control with the active current.....	13
Figure 1.5. Reactive power control with the reactive current .....	14
Figure 1.6. VSC with a grid-following control .....	15
Figure 1.7. Active power control with the voltage angle .....	16
Figure 1.8. VSC with a grid-forming control .....	17
Figure 1.9. VSM-based grid-forming control .....	18
Figure 1.10. Frequency droop regulation .....	19
Figure 1.11. Droop-based grid-forming control .....	19
Figure 1.12. IP-controller based active power control .....	20
Figure 1.13. Power regulation with a grid-forming control .....	21
Figure 1.14. VI structure .....	23
Figure 1.15. TCL .....	24
Figure 1.16. General structure of a Type-IV wind turbine.....	24
Figure 1.17. General components of a wind turbine .....	25
Figure 1.18. Torque coefficient characteristic as a function of TSR and pitch angle..	26
Figure 1.19. One-mass model of a drivetrain .....	27
Figure 1.20. Two-mass model of a drivetrain [73] .....	27
Figure 1.21. Two-mass model of a drivetrain in a per-unit system .....	28
Figure 1.22. PMSG mathematical model and control in a d-q frame .....	29
Figure 1.23. Wind turbine operating zones as a function of the wind speed [75].....	30
Figure 1.24. Pitch control .....	31
Figure 1.25. Type-IV wind turbine with a grid-following control.....	33
Figure 1.26. $U_{dc}$ – control strategy .....	34
Figure 1.27. Simplified model of a wind turbine with $p$ – control strategy.....	36
Figure 1.28. DC bus voltage control with an anti-windup .....	37

Figure 1.29. Behavior of a grid-forming wind turbine with $p$ – control strategy: a) – grid frequency, b) active power at PCC, c) DC-bus voltage, d) electromagnetic torque....	40
Figure 2.1. Coupling between MPPT and grid-forming control .....	42
Figure 2.2. Impact of power reference on the inertial response provision, a) grid-forming VSC connected to an infinite power source, b) grid-forming VSC interfacing a wind turbine.....	44
Figure 2.3. Impact of reduced effective inertia on the grid frequency .....	44
Figure 2.4. Impact of increased inertia constant in a grid-forming control on the grid frequency .....	45
Figure 2.5. Position of the LPF for the MPPT power reference .....	45
Figure 2.6. Effect of the MPPT’ LPF on the wind turbine behaviour: a) grid frequency, b) active power at PCC, c) DC bus voltage, c) generator-side rotational speed .....	46
Figure 2.7. Impact of increased inertia constant in a grid-forming control on the grid frequency (the LPF is added to the MPPT reference) .....	46
Figure 2.8. Wind turbine dynamics with different values of inertia constants: a) active power at PCC, b) DC bus voltage, c) electromagnetic torque, d) generator-side rotational speed, e) turbine-side rotational speed .....	49
Figure 2.9. Analysis of the DC bus voltage controller’ time response variation: a) active power at PCC, b) DC bus voltage, c) electromagnetic torque, d) generator-side rotational speed.....	50
Figure 2.10. Results on variation of the measurement delay: a) active power at PCC, b) DC bus voltage, c) electromagnetic torque, d) generator-side rotational speed .....	50
Figure 2.11. Block diagram of the electromagnetic torque reference modification with a damping torque derived with a HPF.....	51
Figure 2.12. Block diagram of the electromagnetic torque reference modification with a damping torque derived with a BPF .....	52
Figure 2.13. Block diagram for a combined damping method.....	53
Figure 2.14. 2-pulse ZV filter shaping the reference of the electromagnetic torque ...	54
Figure 2.15. Model of a grid-forming wind turbine with the indicated damping block	55
Figure 2.16. Comparison of damping with a HPF and a ZV filter: a) active power at PCC, b) DC bus voltage, c) electromagnetic torque, d) generator-side rotational speed, e) turbine-side rotational speed .....	57
Figure 2.17. Variation of the DC bus voltage controller’ settling time: a) active power at PCC, b) DC bus voltage, c) electromagnetic torque, d) generator-side rotational speed, e) turbine-side rotational speed .....	58
Figure 2.18. System model, damping + sharing of damping effect .....	60

Figure 2.19. Variation of gain $k$ in the term $\Delta p$ for sharing the damping effect: a) active power at PCC, b) DC bus voltage, c) electromagnetic torque, d) generator-side rotational speed, e) turbine-side rotational speed, f) $\Delta p$ power.....	61
Figure 2.20. Description of the damping block with de-activation based on the DC bus voltage criterion .....	62
Figure 2.21. Damping de-activation for a RoCoF event: a) active power at PCC, b) DC bus voltage, c) electromagnetic torque, d) generator-side rotational speed, e) turbine-side rotational speed .....	63
Figure 2.22. Description of the damping block with de-activation based on DC and AC voltage criteria.....	64
Figure 2.23. Damping de-activation for a 100-ms three-phase fault: a) active power at PCC, b) DC bus voltage, c) electromagnetic torque, d) generator-side rotational speed, e) turbine-side rotational speed .....	65
Figure 2.24. Variation of drivetrain shaft stiffness: a) active power at PCC, b) DC bus voltage, c) electromagnetic torque, d) generator-side rotational speed, e) turbine-side rotational speed.....	66
Figure 2.25. Scenarios S1, S2: a) active power at PCC, b) DC bus voltage, c) electromagnetic torque, d) generator-side rotational speed.....	68
Figure 3.1. Generic WPP aggregation into the MMM based on electrical topology ...	71
Figure 3.2. Generic WPP with highlighted clusters .....	74
Figure 3.3. Generic WPP for cluster 2 .....	75
Figure 3.4. Cluster-based MMM.....	77
Figure 3.6. Illustration of the wake effect with Jensen model .....	80
Figure 3.7. Wind speed distribution in a string of wind turbines.....	81
Figure 3.8. Geographical location of Thanet WPP .....	82
Figure 3.9. Collector network of Thanet WPP [143] .....	82
Figure 3.10. WPP model .....	84
Figure 3.11. Wind turbine locations in Thanet WPP .....	87
Figure 3.12. Wind speed distribution in a case study WPP, eastern wind direction....	87
Figure 3.13. North-eastern (a) and northern (b) wind direction.....	88
Figure 3.14. Clusters formation with indicated centroids .....	90
Figure 3.15. Main code elements for the $k$ – means clustering algorithm [152] .....	91
Figure 3.16. WPP map with highlighted clustering for a) 2 clusters, b) 3 clusters, c) 4 clusters.....	93
Figure 3.17. Eastern wind direction, upstream wind speed 13.5 m/s.....	94

Figure 3.18. The active power response from detailed model and DEMs in the low- and high-wind speed regions, a) 9 m/s, b) 18 m/s.....	95
Figure 3.19. RMSPE for eastern wind direction .....	97
Figure 3.20. Optimal number of clusters for one wind direction .....	98
Figure 3.21. Generalized algorithm for determination of the optimal number of clusters.....	99
Figure 3.22. Multi-segment round plot for $RoCoF = 2 \text{ Hz/s}$ .....	100
Figure 3.23. Multi-segment round plot for $RoCoF = 2.5 \text{ Hz/s}$ .....	101
Figure 3.24. Multi-segment round plot for $RoCoF = 3 \text{ Hz/s}$ .....	102
Figure 3.25. Universal multi-segment round plot .....	103
Figure 3.26. Universal multi-segment round plot with extended zone for the cluster-based MMM .....	104

## List of tables

Table 1. Pilot grid-forming projects [27] .....	6
Table 2. Parameters of the modern wind turbines .....	7
Table 1.1. Base values for per-unit conversion .....	14
Table 1.2. System modelling and assumptions .....	37
Table 1.3. Grid parameters .....	38
Table 1.4. Parameters of wind turbine generator and DC bus .....	38
Table 1.5. Controller parameters .....	39
Table 2.1. Parameters of damping filters .....	56
Table 2.2. Drivetrain oscillatory modes estimation error scenarios.....	67
Table 3.1. Cable electrical parameters .....	83
Table 3.2. Grid parameters .....	84
Table 3.3. PCC transformer parameters .....	85
Table 3.4. Grid-side converter and transformer parameters.....	85
Table 3.5. Parameters of wind turbine .....	85
Table 3.6. Controller parameters .....	86
Table 3.7. RMSPE, direction: east, upstream wind speed: 13.5 m/s.....	94
Table 3.8. RMSPE, direction: east, upstream wind speed: 9 m/s.....	96
Table 3.9. RMSPE, direction: east, upstream wind speed: 18 m/s.....	96

## Résumé étendu

Les activités de la société postindustrielle impliquent l'utilisation de grandes quantités d'énergie extraites de la combustion de combustibles fossiles telles que le charbon, le gaz naturel et le pétrole brut. En 2021, selon le rapport Global Energy Review de l'Agence Internationale de l'Energie [1], les émissions de CO<sub>2</sub> provenant de la combustion d'énergie et des processus industriels ont atteint la valeur de 36,3 gigatonnes, soit une augmentation de 6 % par rapport à 2020. Cette tendance s'applique également à d'autres émissions telles que le méthane et le protoxyde d'azote qui, avec le CO<sub>2</sub>, constituent les émissions de gaz à effet de serre (GES). Avec l'augmentation des émissions de GES, le changement climatique continue de s'accélérer. Afin d'atténuer les effets irréversibles du changement climatique, les pays ont accepté l'accord de Paris, qui stipule les actions nécessaires à entreprendre pour limiter l'augmentation de la température mondiale à un niveau de 1,5 à 2 degrés. La transition énergétique des fossiles vers les sources d'énergie renouvelables (ENR) permettra de contribuer à l'accord de Paris. Pour assurer une transition stable et facilitée, l'UE adopte des initiatives politiques telles que le "Green Deal" européen, qui discute d'un plan visant à réduire les émissions de GES de 50 % d'ici 2030 par rapport à 1990, et le Système d'échange de quotas d'émission de l'UE (SEQUE-UE), qui permet aux entreprises d'échanger leurs droits d'émission de GES. L'adoption de ces nouvelles politiques et de ces nouveaux systèmes crée des conditions propices à une intégration rapide des ENR dans le mix énergétique mondial.

La plupart des unités ENR sont reliées au réseau électrique par des convertisseurs d'électronique de puissance. La commande classique du convertisseur utilisée dans les unités ENR actuelles est connue comme le convertisseur grid-following. Un convertisseur grid-following régule la puissance injectée au point de raccordement grâce à un contrôle du courant et est généralement synchronisé avec le réseau à l'aide d'une boucle à verrouillage de phase (PLL). Cette PLL suppose une connexion à une tension de réseau relativement forte ou, en d'autres termes, à un système électrique dont elle peut simplement "suivre" la tension. Ces unités ENR interfacées au réseau avec des convertisseurs électroniques de puissance sont également appelées unités de génération interfacées par convertisseur (CIG). La part croissante de ces unités CIG dans le mix de production induit des transformations inévitables dans le système électrique, notamment :

- Réduction de l'inertie totale du système;
- Augmentation du taux de variation de la fréquence du réseau (RoCoF);
- Réduction des valeurs de la puissance court-circuit

Dans les conditions susmentionnées, les convertisseurs grid-following peuvent être susceptibles d'avoir un comportement instable en raison de leur mécanisme de synchronisation du réseau. Par conséquent, un système électrique comprenant une part importante d'unités CIG interfacées avec des convertisseurs grid-following risque d'être instable. Pour pallier les inconvénients de la commande grid-following, la commande grid-forming est considérée comme une solution viable. La principale distinction d'un convertisseur grid-forming par rapport à un convertisseur grid-following est le fait qu'il est capable de former indépendamment la magnitude et l'angle de la tension à la borne de sortie. Au départ, les convertisseurs grid-forming ont été utilisés dans les micro-réseaux. Aujourd'hui, ils sont en train d'être déployés dans un certain nombre de projets pilotes et leur fonctionnement dans les réseaux de très haute tension est étudié par de nombreux groupes de recherche.

Il existe plusieurs types de contrôle grid-forming. La plupart d'entre eux émulent les dynamiques de l'équation du swing ou les dynamiques de la machine synchrone. Parmi ces contrôles, il y a le statisme puissance-fréquence, machine virtuelle synchrone (VSM), synchronverter, et le contrôle de la synchronisation de la puissance. Un autre type de commande grid-forming est la commande "matching control" où la synchronisation avec le réseau est basée sur l'analogie de la dynamique du rotor de la machine synchrone et des variations de tension du bus continu.

Les fonctionnalités d'une commande grid-forming et son application à un convertisseur électronique de puissance ont été étudiées dans des projets tels que MIGRATE, PROMOTION, OSMOSE et TotalControl. De multiples projets pilotes avec contrôle grid-forming ont été installés dans le monde entier. Parmi eux, un lien HVDC, une centrale éolienne (WPP), des centrales photovoltaïques (PV) et des systèmes de stockage d'énergie par batterie (BESS).

## Contexte actuel et motivation

Parmi les différentes sources d'énergie renouvelables, l'énergie éolienne est l'une des principales contributions à la transition énergétique. La collecte de l'énergie éolienne a une longue histoire. Cependant, la tendance actuelle à l'intégration de l'énergie éolienne à l'échelle du GW dans les processus de production d'électricité a commencé dans les années 90. À ce jour, le développement et le déploiement des WPP dans le système électrique ne cessent de croître. Selon le scénario de WindEurope, la capacité installée cumulée de la puissance éolienne à terre et en mer en Europe devrait atteindre respectivement 253 GW et 70 GW en 2030. L'énergie prévue produite par cette capacité installée pourrait couvrir jusqu'à 29,6 % de la demande totale d'électricité de l'UE.

De nos jours, les progrès technologiques permettent d'améliorer la technologie des éoliennes en termes de capacité nominale et de rendement. L'augmentation de la capacité nominale implique l'augmentation de la hauteur de l'éolienne et du diamètre de son rotor. Selon la configuration de l'éolienne, il existe 4 types d'éoliennes. Les deux premiers types correspondent aux anciens types d'éoliennes, tandis que les deux derniers types sont les éoliennes qui sont actuellement installées.

- **Type-I** : éolienne à vitesse fixe avec un générateur à induction à cage d'écureuil (SCIG);
- **Type-II** : éolienne à vitesse partiellement variable avec un générateur à induction à rotor bobiné (WRIG);
- **Type III** : éolienne à vitesse variable équipée d'un générateur à induction doublement alimenté (DFIG);
- **Type IV** : éolienne à vitesse variable avec générateur synchrone à aimant permanent (PMSG).

L'éolienne de type IV est couramment déployée pour les nouveaux projets WPP. Dans ce type d'éolienne, le rotor de la turbine est connecté à une PMSG qui est ensuite interfacée au réseau avec un convertisseur back-to-back (B2B). Le convertisseur B2B contient les convertisseurs côté machine (MSC) et côté générateur (GSC). Le GSC peut fonctionner aussi bien en mode grid-following qu'en mode grid-forming. Par conséquent, les particularités de la transition entre grid-following et grid-forming sont pertinentes pour une éolienne de type IV.

L'application d'une commande grid-forming aux éoliennes de type IV a fait l'objet d'une attention particulière dans les travaux de recherche. Dans la plupart des travaux de recherche, les éoliennes sont assimilées soit à une source de courant contrôlable, soit à une éolienne avec un modèle de transmission simplifié qui n'est pas assez précis pour décrire complètement la dynamique de l'éolienne. De ce fait, l'impact d'une commande grid-forming sur la structure mécanique de l'éolienne et vice versa n'a pas pu être analysé de manière exhaustive. L'intégration d'un modèle double masse de la partie mécanique permet d'améliorer l'étude de l'impact du convertisseur grid-forming sur l'éolienne.

Les WPP comportent généralement un grand nombre d'éoliennes, qui fournissent de l'énergie au point de raccordement. Afin d'effectuer une analyse du réseau électrique pour le réseau de très haute tension auquel le WPP est connecté, un modèle dynamique équivalent (DEM) représentant l'ensemble des éoliennes est nécessaire. Bien que l'agrégation des WPPs grid-following ait été étudiée en détail au cours des dernières décennies, l'utilisation d'un tel DEM pour les WPPs grid-forming n'a pas été largement abordée dans la littérature. L'agrégation d'un WPP grid-forming dans un modèle équivalent à une seule machine (SMM) a été étudiée. Cependant, l'effet de la distribution de la vitesse du vent à travers un WPP sur la validité du SMM peut être significatif. En effet, la distribution hétérogène du vent peut influencer la précision du DEM. Par conséquent, il est important d'utiliser un DEM qui peut refléter la dynamique du WPP pour différentes conditions de vent.

## **Objectifs de la thèse**

Les sujets de recherche susmentionnés, notamment l'impact du contrôle grid-forming sur la structure mécanique d'une éolienne de type IV et la dérivation d'un modèle équivalent précis pour un WPP grid-forming dans différentes conditions de vent, n'ont pas reçu suffisamment d'attention dans la littérature. Pour remplir ces lacunes, les objectifs principaux de la thèse ont été formulés par l'auteur de ce manuscrit sous la forme des questions de recherche suivantes :

1. Quel est l'impact d'une commande grid-forming sur l'éolienne et vice versa, si les principaux modes du système mécanique de l'éolienne sont conservés ? Si une commande grid-forming a un effet négatif sur l'éolienne, comment cet effet peut-il être atténué ?

2. Quels sont les types de DEM qui existent et comment les obtenir ? Puisque la distribution du vent peut influencer la précision du DEM, comment peut-on la prendre en compte dans le processus d'agrégation ? Comment s'assurer que, pour certaines conditions de vent, le DEM développé pour une WPP connectée au réseau via HVAC est choisi correctement ?

Pour répondre à ces questions, des activités de recherche ont été menées pendant la période de ce programme de doctorat et les résultats sont documentés dans ce manuscrit. Dans ce qui suit, les principales conclusions du chapitre sont résumées :

## **Principales conclusions**

1 - Le chapitre 1 présente la base de modélisation de l'éolienne grid-forming. La discussion et les simulations de ce chapitre démontrent qu'il est possible d'intégrer une commande grid-forming dans le GSC d'une éolienne de type IV. La configuration classique de commande du

convertisseur B2B utilisée dans le cas d'une commande grid-following n'est pas adaptée à une éolienne grid-forming, car le GSC devient sujet à des instabilités en raison de la nécessité de réaliser plusieurs fonctions de commande simultanément. Ainsi, afin d'améliorer la contrôlabilité de l'éolienne grid-forming, la stratégie de contrôle classique est modifiée en permutant les contrôles entre le Machine Side Converter (MSC) et le Grid Side Converter (GSC). Cette stratégie modifiée est appelée stratégie de p-contrôle. Cependant, il a été souligné que la stratégie p-control peut créer des couplages électromécaniques entre la dynamique d'une éolienne et la dynamique d'une commande grid-forming.

2 – Le chapitre 2 traite deux couplages électromécaniques existants dans une éolienne grid-forming. Alors que l'impact de la dynamique de la commande MPPT sur les performances de la commande grid-forming peut être partiellement ou totalement éliminé, l'impact de la commande grid-forming sur la structure mécanique du générateur de l'éolienne requiert plus d'attention. Les vibrations de torsion, qui sont une conséquence de ce couplage, doivent être atténuées ou supprimées. Parmi les solutions d'amortissement présentées, l'amortissement basé sur la méthode d'input shaping a montré une bonne performance. Les résultats de l'analyse complète de cette méthode ont montré que cette méthode d'amortissement est très efficace pour la suppression des vibrations de torsion et est également robuste par rapport aux variations paramétriques. Cependant, il a été souligné qu'il existe un effet secondaire lié à l'amortissement appliqué, notamment des variations accrues de la tension du bus continu. Comme discuté dans ce chapitre, cet effet secondaire peut être atténué par des actions de contrôle supplémentaires.

3 – Le chapitre 3 présente l'agrégation d'un WPP grid-forming. Plusieurs types de DEMs et leur dérivation ont été présentés. Afin d'inclure des conditions de vent réalistes à travers d'un WPP, un modèle de vent de pointe prenant en compte la distribution hétérogène du vent a été implémenté. Le modèle de distribution du vent ainsi que le clustering k - means ont permis d'obtenir des modèles équivalents basés sur des clusters capables de refléter avec précision les caractéristiques dynamiques du modèle détaillé du WPP. Le critère pour la sélection du nombre optimal de clusters dans le modèle équivalent basé sur les clusters a été expliqué. Il a été démontré que pour des conditions de vent spécifiques, en particulier pour les vitesses de vent faibles et élevées, le modèle équivalent classique - SMM, est généralement suffisant pour représenter la dynamique du modèle détaillé du WPP, tandis que pour les vitesses de vent moyennes, le modèle équivalent basé sur les clusters - MMM, devient indispensable. De plus, afin de fournir des informations sur le DEM optimal à utiliser dans telle ou telle condition de vent, un algorithme généralisé pour déterminer le nombre optimal de clusters en fonction des conditions de vent a été proposé. La performance de l'algorithme a été démontrée en l'appliquant à un cas d'étude de WPP. Les résultats de l'application de l'algorithme sont résumés par des diagrammes circulaires universels à segments multiples, qui présentent graphiquement les recommandations du DEM le plus approprié pour différentes conditions de vitesse de vent.

# Introduction

## 1. Background

The activities of the post-industrial society entail the use of vast amounts of energy extracted from the combustion of fossil fuels such as coal, natural gas and crude oil. In 2021, according to the Global Energy Review report by the International Energy Agency [1], the CO<sub>2</sub> emissions from energy combustion and industrial processes reached the value of 36.3 gigatons, which is 6% higher compared to 2020. This trend also applies to other emissions such as methane and nitrous oxide which, along with CO<sub>2</sub>, constitute the green-house gas (GHG) emissions. With the increasing amount of GHG emissions, the climate change continues to accelerate. In order to mitigate the irreversible effects of climate change, countries have accepted the Paris agreement [2], which stipulates the necessary actions to be undertaken to limit the global temperature rise to a 1.5 – 2-degree level. The energy transition from fossils to renewable energy sources (RES) will allow contributing to the Paris agreement. To ensure a steady and alleviated transition, the EU adopts policy initiatives such as the European Green Deal, discussing a plan to reduce GHG emissions to 50% by 2030 compared with 1990 [3], and the EU Emissions Trading System allowing companies to trade the GHG emission rights [4]. Adoption of such new policies and systems lays out propitious conditions for a rapid integration of RES to the global energy mix.

Most of the RES units are interfaced to the electrical grid with power electronic converters. The classical converter control employed in current-day RES units is known as grid-following [5]. A grid-following converter regulates the output power thanks to a current control and is typically synchronized to the grid with a phase-locked loop (PLL). This PLL assumes a connection to a relatively stiff grid voltage, or put differently, to a power system whose voltage it can just ‘follow’. These RES units interfaced with power electronic converters are also called converter-interfaced generation (CIG) units. The increasing share of these CIG units in the generation mix induces inevitable transformations in the power system, including:

- Reduction of the total system inertia;
- Increase of the Rate-of-Change of Frequency (RoCoF);
- Reduction of the grid strength and short-circuit levels.

Grid-following converters under abovementioned conditions can become prone to unstable behavior due to their grid synchronization mechanism. Hence, a power system with a high share of CIG units interfaced with grid-following converters is at risk of facing instability. To overcome the grid-following control's drawbacks, grid-forming control is perceived as a viable solution. The main distinction of a grid-forming converter from a grid-following one is that it can form the magnitude and angle of the voltage at the output terminal independently. Initially, grid-forming converters have been used in microgrids [5]–[7]. Nowadays, they are being rapidly deployed in a number of pilot projects and their operation in transmission systems is being investigated by numerous research groups [8], [9].

Several types of grid-forming controls exist. Most of them emulate swing equation dynamics or additional inner dynamics of a synchronous machine. Among them are power-frequency droop [5]–[7], [10]–[13], virtual synchronous machine (VSM) [14]–[16], synchronverter [17], and power synchronization control [18]. Another type of a grid-forming control is the matching control where

the synchronization to the grid is based on the analogy of the synchronous machine rotor dynamics and the DC bus voltage variations [19]–[22].

The functionalities of a grid-forming control and its application to a power electronic converter have been studied in projects such as MIGRATE, PROMOTION, OSMOSE and TotalControl [23]–[26]. Multiple pilot projects with grid-forming control have been installed around the world. Among them, an HVDC link, a wind power plant (WPP), photovoltaic (PV) plants and battery energy storage systems (BESS). These projects are described in [27] and are listed below in Table 1. In the last column, the application purposes are mentioned. These are:

- Ancillary Services (AS) provided by the fast frequency response;
- Participation of the CIG unit(s) in the wholesale Energy Market (EM);
- The ability of the CIG unit(s) to isolate from the main grid during severe faults by switching to Islanded Operation (IO);
- The Black Start capability (BS) implying the ability of the CIG unit(s) to re-energize the electrical grid.

Table 1. Pilot grid-forming projects [27]

Project	Year	Rated Power [MW]	Capacity, [MWh]	Applications
Zurich BESS	2012	1	0.58	AS, EM, IO
Ausnet Gess	2012	1	1	AS, IO
Mackinac HVDC	2012	200	-	HVDC
SMA projects	2017 – 2019	0.8 – 15	0.4 – 15	IO
Dersalloch Wind Farm	2019	69	-	AS, BS, IO
Hornsdale Power Reserve	2017 – 2020	150	194	AS, EM
ESCRI-SA Project	2018 – 2019	30	8	AS, EM
Democrat demonstrator	2018	0.23	0.22	BS, EM, IO
NREL Campus	2019	1.25	1.25	AS

## 2. Current context and motivation

Among the various RES, wind energy is one of the key contributors towards the energy transition. The harvesting of the wind energy has a long story. However, the actual trend of the GW-scale wind energy integration into the processes of the electricity generation has started in 90's. By now, the development and deployment of WPPs into the power system is ever-increasing. According to WindEurope' central scenario [28], the cumulative installed capacity of the onshore and offshore wind power in Europe is projected to rise to 253 GW and 70 GW by 2030, respectively. The prospected energy produced by this installed capacity could cover up to 29.6%

of the total EU electricity demand. The distribution of the installed wind capacity by country is represented in Figure 1.

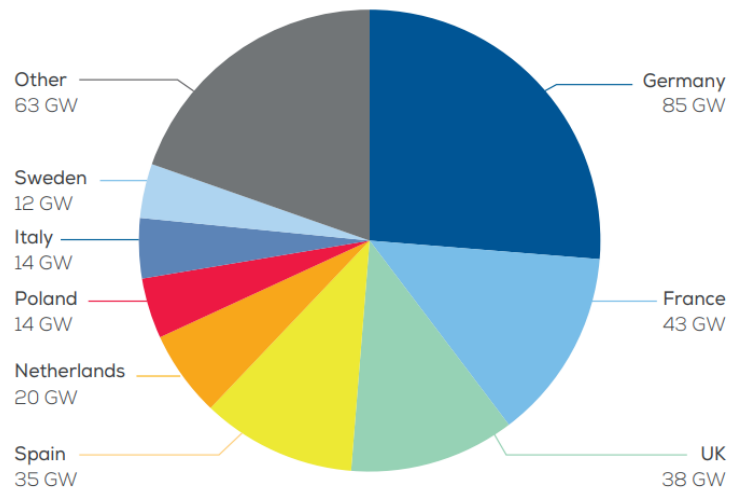


Figure 1. 2030 wind energy installed capacity by country according to Central Scenario in the EU [28]

Nowadays, technological progress results in an improvement of the wind turbine technology in terms of rated capacity and efficiency. The increase of the rated capacity involves the increase of the wind turbine height and turbine rotor diameter. The biggest wind turbines in terms of the rated capacity are listed in Table 2. These are mostly represented by the wind turbines with a hybrid drivetrain or direct drivetrain technology. The biggest offshore and onshore wind turbines with the rated capacity of 16 MW and 7.2 MW, respectively, are currently in the prototype stage.

Table 2. Parameters of the modern wind turbines

Wind turbine	Manufacturer	Capacity, MW	Hub height, m	Rotor diameter, m
<b>Offshore</b>				
MySE 16.0-242	MingYang Smart Energy	16	264	242
V236-15.0	Vestas	15	280	236
SG 14-236 DD	Siemens Gamesa	14 - 15	Site-specific	236
Haliade-X	GE	14	260	220
<b>Onshore</b>				
V172-7.2	Vestas	7.2	166	172
GE-158	GE	6.1	161	158
N163/6.X	Nordex	6.0	164	163
GW 165-6.0	Goldwind	6.0	100	165

Depending on the wind turbine configuration, there are 4 types of wind turbines. The first two types correspond to older types of wind turbines, while the last two types are the wind turbines which are currently installed.

- **Type-I**, fixed-speed wind turbine with a squirrel-cage induction generator (SCIG);
- **Type-II**, partially variable-speed wind turbine with a wound-rotor induction generator (WRIG);
- **Type-III**, variable-speed wind turbine with a doubly-fed induction generator (DFIG);
- **Type-IV**, variable-speed wind turbine with a permanent-magnet synchronous generator (PMSG).

The Type-IV wind turbine is being commonly deployed for new WPP projects. In this type, the turbine rotor is connected to a PMSG that is then interfaced to the grid with a fully-rated back-to-back converter. The back-to-back (B2B) converter contains the machine-side (MSC) and the generator-side (GSC) converters. The GSC can operate in grid-following as well as in grid-forming mode. Hence, the peculiarities of transition from grid-following to grid-forming are relevant for a Type-IV wind turbine.

The application of a grid-forming control to Type-IV wind turbines have received significant attention in research works. For example, the integration of a grid-forming control into the wind turbine has been studied in [26], [29]–[36]. The black-start of the WPP with grid-forming wind turbines has been investigated in [37]–[40]. The fault-ride through capability of a grid-forming wind turbine was analyzed in [41]. In most research works the wind turbines are simplified either to a controllable current source or to a wind turbine with a simplified drivetrain model that is not accurate enough to completely depict wind turbine dynamics. Due to that, the impact of a grid-forming control on mechanical structure of the wind turbine and vice versa could not be comprehensively analyzed. Therefore, to evaluate this impact, it is important to use a more detailed mechanical model of a wind turbine.

WPP's typically have a large number of wind turbines, all supplying power to the same point of common coupling. In order to conduct a power system analysis for the transmission system with WPPs connected to it, a dynamic equivalent model (DEM) representing the WPP is required. Although the aggregation of classical grid-following WPP's has been studied in detail over the past decades, the derivation of such a DEM for the grid-forming WPP has not been widely addressed in literature. The aggregation of a grid-forming WPP into a single-machine equivalent model (SMM) has been discussed in [24], [42], [43]. However, the effect of the wind speed distribution across a WPP on the validity of the DEM was not addressed. Indeed, the heterogeneous wind distribution can significantly influence the accuracy of the DEM. Therefore, it is important to have a DEM that can reflect the WPP dynamics for different wind conditions.

### 3. Thesis objectives and contributions

The abovementioned research subjects, namely the impact of grid-forming control on the mechanical structure of a Type-IV wind turbine and a derivation of an accurate DEM for a grid-forming WPP under different wind conditions have not received enough attention in literature. To fill these gaps, the main thesis objectives were formulated by the author of this manuscript in the form of the following research questions:

1. What is the impact of a grid-forming control on the wind turbine and vice versa, if the main modes of the wind turbine mechanical system are retained? If a grid-forming control has a negative effect on the wind turbine, how can this effect be mitigated?

2. What are the types of DEMs which exist and how can they be obtained? Since the wind distribution can influence the accuracy of the DEM, how it can be taken into account in the aggregation process? How to be sure that for certain wind conditions, the DEM developed for a grid-forming WPP connected to the grid via HVAC is chosen correctly?

To answer these questions the research activities have been conducted during the period of this joint PhD program. The final research outcomes listed below are the **main contributions** of this thesis.

Firstly, the electromechanical couplings in a grid-forming wind turbine are identified. The main coupling identified in this thesis is between the dynamics of a grid-forming control and the wind turbine generator. Due to this coupling, the disturbances in the external power system have a very strong effect on the electromechanical torque and may induce mechanical vibrations in the wind turbine structure. The methods for vibration damping in a grid-forming wind turbine are presented and discussed in detail with a focus on the input shaping method which is proposed in this thesis. The positive impact of the proposed damping on the suppression of torsional vibrations as well as its robustness against parametric variations are confirmed through simulations.

Secondly, the aggregation of the grid-forming WPP connected to the transmission system and composed of multiple grid-forming wind turbines is analyzed with consideration of the heterogeneous wind distribution across a WPP. The outcome of this analysis is the proposition of the generalized algorithm that provides recommendations for the optimal DEM to be used for any possible wind condition. The algorithm is verified by applying it to the case study WPP. The algorithm can be used for the dynamic analysis of the WPPs connected to the transmission system where the WPPs are to be accurately represented by its equivalent models with a focus on frequency events.

#### **4. Outline of the thesis**

The remainder of the thesis manuscript is organized in three chapters.

The first chapter presents the fundamentals of the power electronic converter control based on the grid-following and grid-forming concept. It is followed by the modelling of the main wind turbine components such as the aerodynamic model, mechanical model, generator model and turbine controls. Then, the classical control of a grid-following Type-IV wind turbine is recalled. By substituting the grid-following control with the grid-forming control, two possible control configurations for a grid-forming wind turbine are derived and compared.

The second chapter is devoted to the investigation of the electromechanical couplings that exist in a grid-forming wind turbine due to the selected control configuration of the B2B converter. These interactions include the impact of the wind turbine speed regulation by means of the MPPT on the grid-forming control and, also, the impact of the grid-forming control on the mechanical structure of the wind turbine. The latter is represented by the fast variations of the electromagnetic torque that induce torsional vibrations originating at the wind turbine drivetrain and propagating to all wind turbine components and to the electrical network. Hence, the damping methods for mitigation of the torsional vibrations are analyzed. The proposed damping based on the input

shaping method is described and its effectiveness and robustness are verified by applying the designed damping solution to a 5-MW wind turbine.

In the third chapter, the aggregation of the WPP with numerous grid-forming wind turbines is analyzed. The wind turbines used in this chapter are the grid-forming wind turbines studied in the previous chapter and have been equipped with vibration damping function. Different types of DEMs, such as the SMM and the cluster-based Multi-Machine equivalent Model (MMM) are presented. The derivation of the cluster-based MMM requires the application of the clustering algorithm. The clustering algorithm as well as the selection of the optimal number of clusters are introduced. The optimal DEM selection process is presented for a case study where several wind speeds in one wind direction are imposed to the WPP. The presented studies highlight the situations in which the cluster-based MMM is bringing a significant accuracy improvement over the SMM. Then, the algorithm that determines the optimal number of clusters in a DEM for any wind condition is generalized and verified. The outcomes of the proposed algorithm are recommendations of the optimal DEM to be utilized for given wind conditions.

## 5. List of publications

The publications that are result of the work conducted in the scope of this thesis are listed below:

- **Journal I:** “*Application of input shaping method to vibrations damping in a Type-IV wind turbine interfaced with a grid-forming converter*”, **Artur Avazov**, Frédéric Colas, Jef Beerten, Xavier Guillaud, Electric Power Systems Research, 210, 2022.
- **Conference I:** “*Influence of the frequency support provided by a grid-forming control-based wind turbine on the loading of its mechanical system*”, **Artur Avazov**, Frédéric Colas, Jef Beerten, Xavier Guillaud, 19th Wind Integration Workshop, 2020.
- **Conference II:** “*Damping of Torsional Vibrations in a Type-IV Wind Turbine Interfaced to a Grid-Forming Converter*”, **Artur Avazov**, Frédéric Colas, Jef Beerten, Xavier Guillaud, 2021 IEEE Madrid PowerTech, 2021.

# 1. Modelling and control of a grid-forming wind turbine

In order to investigate in detail the operation of a grid-forming wind turbine, it is necessary to present the control of a power electronic converter operating in the classical grid-following as well as in the grid-forming mode and interfacing a Type-IV wind turbine to the electrical grid.

In the first section, the classification of the converter controls with regards to the power transfer is presented. The classification includes grid-following and grid-forming controls. Both controls are described and their dynamic implementation is demonstrated with a VSC connected to a generic power source. In the second section, the main components of a wind turbine such as aerodynamic, mechanical, electrical models and general controls are described. Further, in the third section, the control configurations of a B2B converter are analyzed while the GSC is equipped with a grid-forming control. The descriptions are followed by a comparison of the analyzed control configurations on a test case consisting of a 5-MW Type-IV wind turbine.

## 1.1. Classification of converter controls

In this section, the formulations for the power transfer through a power electronic converter are discussed. Based on these formulations, the grid-following and grid-forming control strategies are derived and described, along with the presentation of its dynamic implementation for a VSC connected to a primary power source.

### 1.1.1. Power control with a converter

The interface of a CIG to the power system can involve several stages of current conversion. For example, PV panels generate DC current at a low-voltage level. Then, a DC-DC voltage amplification is used to increase the voltage level. Finally, a PV unit is connected to the grid with a DC-AC converter. For a modern Type-IV wind turbine, a generator is interfaced to the grid with a B2B converter ensuring the AC-DC-AC conversion. A generic system connecting a DC power source to the AC grid is shown in Figure 1.1. It consists of a power source linked to a VSC with a DC capacitor.

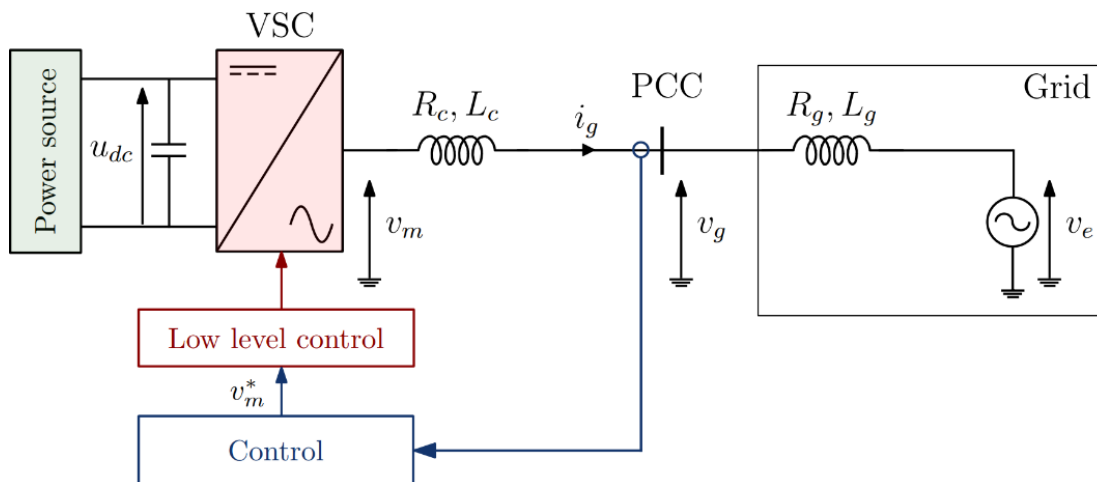


Figure 1.1. VSC connected to the grid

In Figure 1.1,  $v_m = [v_{m,a}, v_{m,b}, v_{m,c}]$  corresponds to the three-phase phase-to-ground voltages modulated by the VSC controls from the DC bus voltage. The low-level control generates the corresponding modulation indices to regulate the converter output voltage according to a three-phase modulated voltage reference,  $v_m^*$ . This includes a pulse-width modulation (PWM) and switching dynamics. Since the interest in this thesis is on slow wind turbine dynamics, the PWM and switching dynamics are not considered further, and only the classical average model of the VSC is used throughout this entire work. The converter is connected to the AC grid by means of a connection impedance ( $R_c, L_c$ ). The reactance of the connection impedance accounts for the leakage reactance of the connecting transformer,  $X_c$ . The AC grid is balanced and modeled as a Thévenin equivalent comprised of a voltage source and the grid impedance ( $R_g, L_g$ ). The  $v_g$  and  $v_e$  are respectively the PCC voltage and the grid voltage, and  $i_g$  is the grid current. The resistive part is assumed to be much smaller than the inductance ( $R_g \ll X_g$ ), where  $X_g = L_g \omega_g$ .

To describe the power transfer from the VSC to the PCC, a single line diagram is shown in Figure 1.2 where  $\delta_m$ ,  $\delta_g$  and  $\delta_e$  are the phasor angles of corresponding voltages, and  $\phi$  is the angle between the voltage  $\bar{V}_g$  and the current  $\bar{I}_g$ .

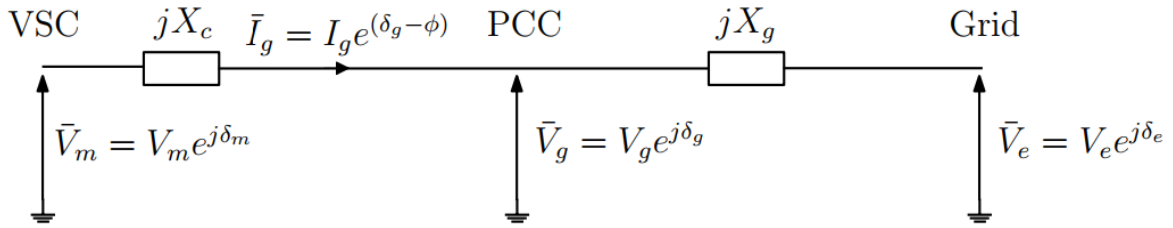


Figure 1.2. Single-line diagram

The phasor representation of this system is shown in Figure 1.3.

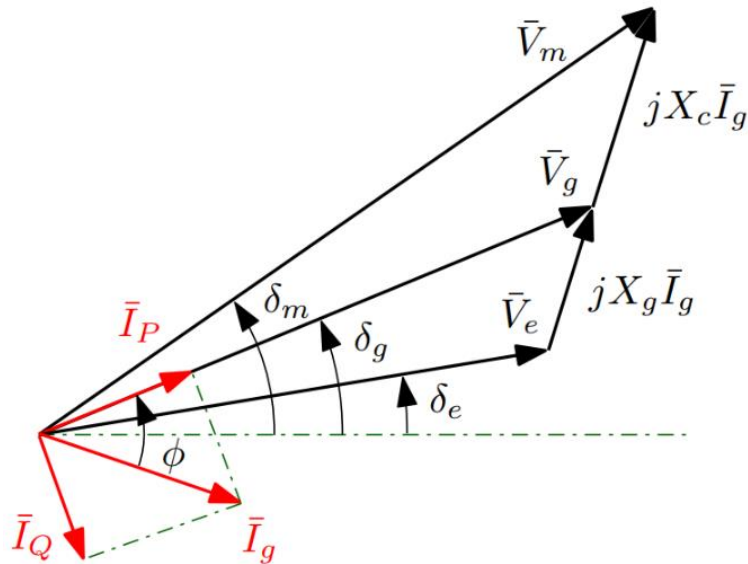


Figure 1.3. Phasor representation of the system

The active power transfer and reactive power circulation can be expressed as:

$$P = V_g I_P = V_g I_g \cos(\phi) \quad (1.1)$$

$$Q = V_g I_Q = V_g I_g \sin(\phi) \quad (1.2)$$

Where  $V_g$  is the voltage magnitude,  $I_P$  is the active current magnitude,  $I_Q$  is the reactive current magnitude.

Another formulation is based on the modulated voltage,  $V_m$ :

$$P = \frac{V_m V_g}{x_c} \sin(\delta_m - \delta_g) \quad (1.3)$$

$$Q = \frac{V_m^2}{x_c} - \frac{V_m V_g}{x_c} \cos(\delta_m - \delta_g) \quad (1.4)$$

Knowing that the difference in voltage angles between two nodes is small, Equations 1.3 – 1.4 can be re-written as:

$$P = \frac{V_m V_g}{x_c} (\delta_m - \delta_g) = \frac{V_m V_g}{x_c} \psi \quad (1.5)$$

$$Q = \frac{V_m^2}{x_c} - \frac{V_m V_g}{x_c} \quad (1.6)$$

where  $\psi = \delta_m - \delta_g$ .

As will be made clear in the subsequent sections, these two formulations correspond to two different ways of converter control: grid-following and grid-forming. The grid-following control adheres to the first formulation based on the active and reactive current. The grid-forming control corresponds to the second formulation based on the modulated voltage.

### 1.1.2. Grid-following control

In the first formulation the active and reactive power depend on a current control. Simplified control block diagrams for active and reactive power regulation are shown in Figure 1.4 – Figure 1.5.  $C(s)$  is a control stage that usually consists of a PI controller. The controller's integrator keeps zero steady-state error and compensates for disturbances.

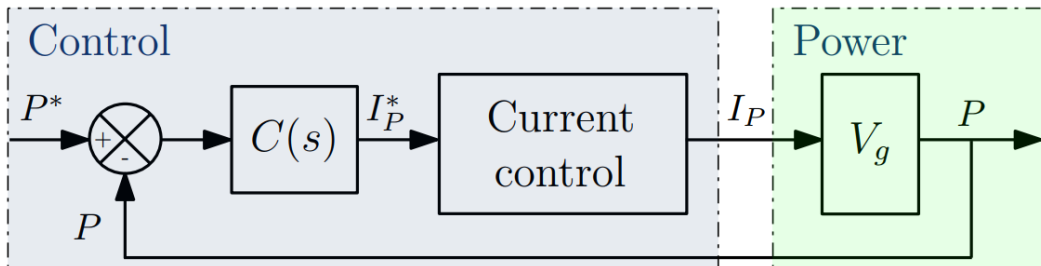


Figure 1.4. Active power control with the active current

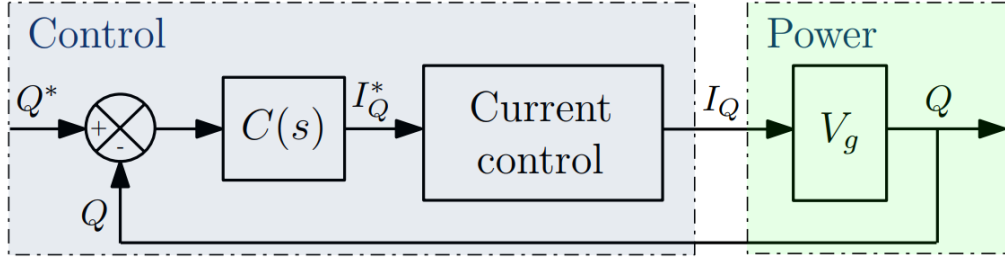


Figure 1.5. Reactive power control with the reactive current

As shown in Figure 1.4, when the active current is controlled, the grid voltage angle has to be known to ensure the alignment of the active current to the grid voltage at the PCC. Put differently, an accurate estimation of the grid voltage angle is necessary. The grid-following principle indicates that whenever the grid voltage changes, the modulated converter voltage has to follow this change in order to keep a constant current output.

The dynamic implementation of the converter control based on grid-following control principles in a d-q frame is shown in Figure 1.6. The corresponding modeling and control of the VSC are undertaken in a per-unit system, with the base quantities for this per unit conversion defined in Table 1.1.

Table 1.1. Base values for per-unit conversion

Base quantity	Value	Base quantity	Value
Base power, $S_b$	5 MW	Base impedance, $Z_b$	$\frac{3V_b^2}{S_b} = 0.095 \Omega$
Base line-to-line voltage, $U_b$	690 V	Base impedance, $L_b$	$\frac{Z_b}{\omega_b^{el}} = 0.0003 \text{ H}$
Base line-to-ground voltage, $V_b$	$\frac{U_b}{\sqrt{3}} = 398 \text{ V}$	Base capacitance, $C_b$	$\frac{1}{\left(\frac{Z_b}{\omega_b^{el}}\right)} = 3305 \text{ F}$
Base electrical angular frequency, $\omega_b^{el}$	314.16 rad/s	Base DC bus voltage, $U_{b_{dc}}$	1500 V
Base frequency, $f_b$	$\frac{\omega_b^{el}}{2\pi} = 50 \text{ Hz}$	Base DC current, $I_{b_{dc}}$	$\frac{S_b}{U_{b_{dc}}} = 3334 \text{ A}$
Base AC current, $I_b$	$\frac{S_b}{3V_b} = 4187 \text{ A}$		

The estimate of the grid voltage angle is provided by a PLL. The estimated phasor angle,  $\hat{\delta}_g$ , is converted into a time-domain angle as  $\hat{\theta}_g = \hat{\omega}_g t + \hat{\delta}_g$ , where  $\hat{\omega}_g$  is the estimated grid frequency.

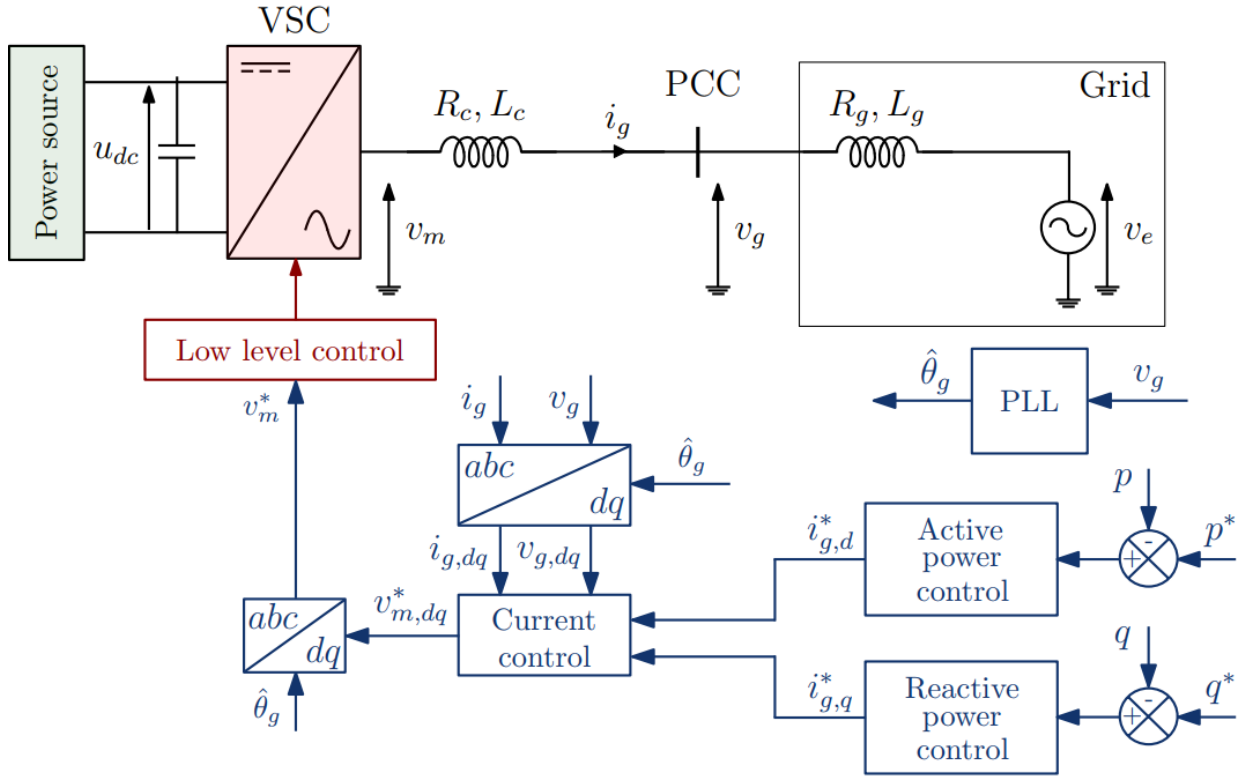


Figure 1.6. VSC with a grid-following control

By definition, a grid-following converter follows the grid voltage during normal grid operation and after grid disturbances. However, the integration of a vast number of CIG units all operating in grid-following mode can undermine the stable operation of the power system especially when it experiences a phase-out of traditional synchronous machines forming the grid frequency and grid voltage.

Firstly, there is a risk of unstable operation of grid-following converters in the weak grid. This issue is often related to the functioning of the PLL, imposing a delay in frequency estimation and prone to instabilities while being connected to the weak grid point [44]–[50]. To increase stability margin, the PLL control can be improved by different solutions such as SOGI-PLL, slowing down of a PLL, a backup PLL, a frequency locked loop (FLL) proposed in [51], [52]. It should be noted that also the design of other control loops and overall control configuration in grid-following converters become more challenging when moving to weak system conditions.

Secondly, grid-following converters able to operate under weak grid conditions can still become unstable during system splits in a power system. Unstable operation after a system split depends in part on the share of CIG units in the split areas. If the share of CIG units becomes significant and these CIG units operate in grid-following mode, instability issues are likely to arise. Otherwise, a system can remain stable.

To mitigate or resolve these challenges in a power system with a high share of CIG units, converter controls switching from grid-following to grid-forming may be required in the future for certain CIG units [53]. In order to explain the concept properly, the use of the second formulation of the power transfer can help to describe the principles behind grid-forming control.

### 1.1.3. Grid-forming control

In the second active power formulation in Equation 1.5, the active power and the converter voltage can be controlled with the references of the voltage angle,  $\delta_m^*$ , and voltage magnitude,  $V^*$ , respectively. A simplified control block for active power control is provided in Figure 1.7. With this control block the synchronization to the grid is based on the phase angle of the converter output voltage.

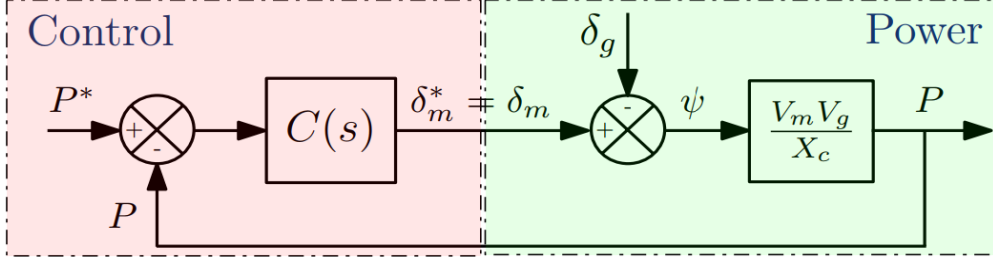


Figure 1.7. Active power control with the voltage angle

The dynamic implementation of a converter based on a grid-forming control in a d-q frame is shown in Figure 1.8. For the active power regulation there is no need to know the information about the grid voltage angle. To properly control the active power, the power measurements at the PCC are sufficient. The converter voltage magnitude can be defined by a constant voltage set-point,  $V^*$ , or it can be complemented with a reactive power droop gain,  $n_q$ , if parallel operation of several converters is expected. The reactive power droop function is expressed as follows:

$$V_m^* = V^* + n_q \left[ q^* - q \left( \frac{\omega_q}{s + \omega_q} \right) \right] \quad (1.7)$$

where  $q^*$  is the reactive power reference,  $\omega_q$  is the cut-off frequency of a LPF.

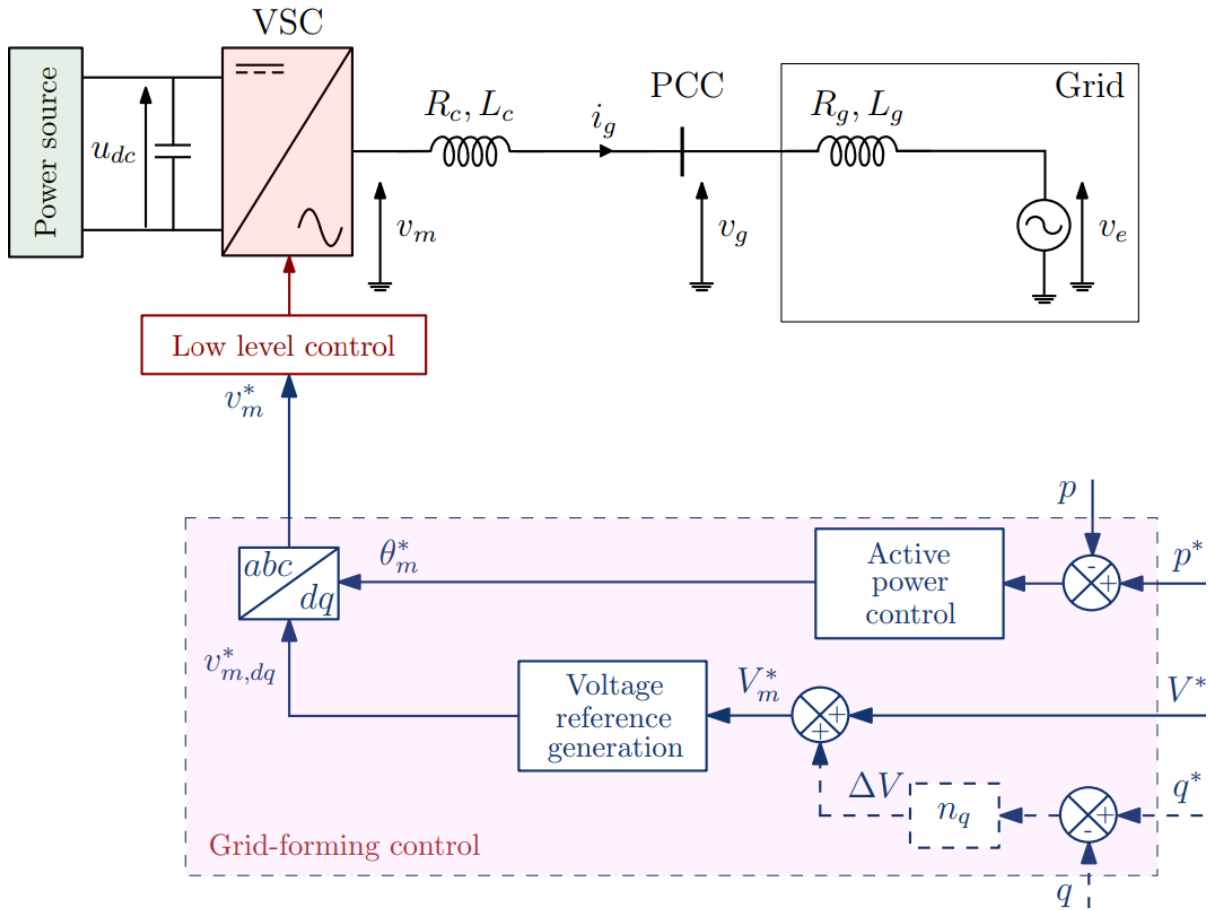


Figure 1.8. VSC with a grid-forming control

There are two main functions in a grid-forming control: control of the active power and control of the converter voltage magnitude. The control structure for both functions will be discussed separately.

### Active power regulation.

The term grid-forming was firstly introduced in [54]. Initially, the grid-forming converters were successfully used in microgrids [5]–[7]. With an increasing share of CIG units, this concept has been extended to the level of a transmission system [8], [9]. So far, many different grid-forming control structures have been proposed in literature:

- a) power-frequency droop [5]–[7], [10]–[13],
- b) virtual synchronous machine (VSM) [14]–[16],
- c) synchronverter [17],
- d) power synchronization control [18],
- e) matching control [19]–[22],
- f) (distributed) virtual oscillator [55]–[57].

The main difference is in the control of the active power. Most of these controls (a – d) mimic the swing equation or the behavior of a SM. In the following, three types of a grid-forming control will be presented.

- VSM

A conventional SM contributes significantly to power system stability thanks to its inherent properties. Those are natural inertial response and damping, load sharing, voltage or reactive power control and high fault currents. A VSM control is intended to mimic the behavior of a SM by emulating the SM' behavior. As shown in Figure 1.9, the emulation can be based on the swing equation that represents the inertia and damping of a SM.

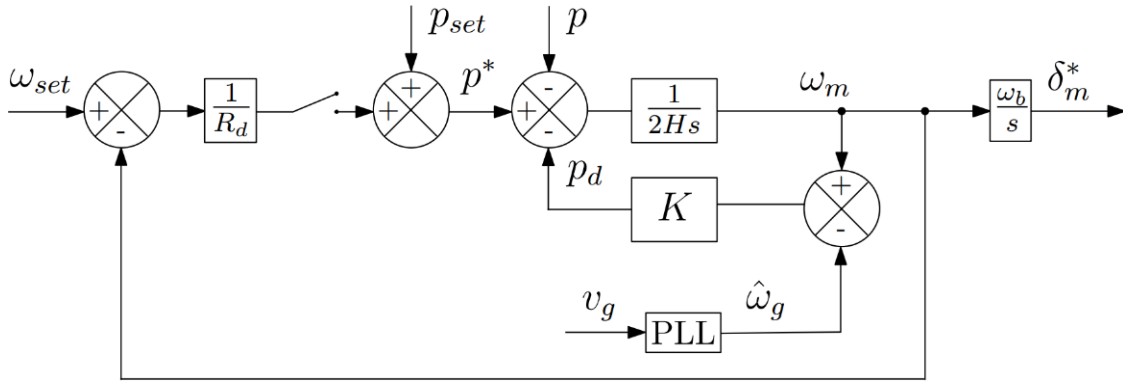


Figure 1.9. VSM-based grid-forming control

The relation of the frequency at converter terminals,  $\omega_m$ , to the active power can be expressed by means of the following differential equations:

$$2H \frac{d\omega_m}{dt} = p^* - p - p_d \quad (1.8)$$

$$2H \frac{d\omega_m}{dt} = p^* - p - K(\omega_m - \hat{\omega}_g) \quad (1.9)$$

where  $p$  is the measured power,  $p^*$  is the power set-point,  $p_d$  is the damping power,  $p_{set}$  is the set power,  $H$  is the inertia constant,  $K$  is the damping constant,  $\omega_{set}$  is the frequency set-point,  $R_d$  is the frequency droop gain.

In Figure 1.9, a PLL serves to decouple the inertial response and frequency support [58]. The latter can be activated if the switch is closed.

- Droop-based grid-forming control

The droop concept is a widely used approach to control parallel operation of SMs connected to a transmission system. It is based on the relation of active power and frequency as shown in Figure 1.10 and expressed in Equation 1.10.

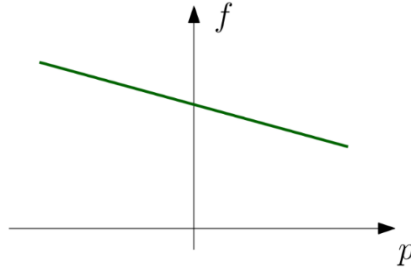


Figure 1.10. Frequency droop regulation

$$f = f_0 - m_p(p - p_0) \quad (1.10)$$

where  $m_p$  is the active power droop gain.

With a droop regulation, generators connected in parallel to the transmission system participate in the load sharing proportionally to the droop settings which are in the range of 1 to 5 % [59]. Thus, a connection of a new load is shared among active generators. A droop-regulated generator uses local measurements and does not require communication with other generating units.

The grid-forming control based on a droop characteristic has been thoroughly elaborated in the Migrate project [60]. Depending on the control needs, different implementations of a droop-based grid-forming control can be selected [58]. In Figure 1.11, one representation of a droop-based type is shown. The low-pass filter (LPF) is added to filter harmonics and power perturbations [61], [62]. It also allows reducing the bandwidth of the power control, so there is less risk of interaction with the inner control loop [63]. Usually, a LPF is placed to the power measurement signal. However, in this scheme, it is in the main path. Such positioning permits to mimic the inertial effect as has been shown in [64]. The inertial effect is the consequence of a slower synchronization to the grid as imposed by the LPF in the path of power regulation. The frequency support in this scheme is decoupled from the inertial effect [58] and can be optionally activated.

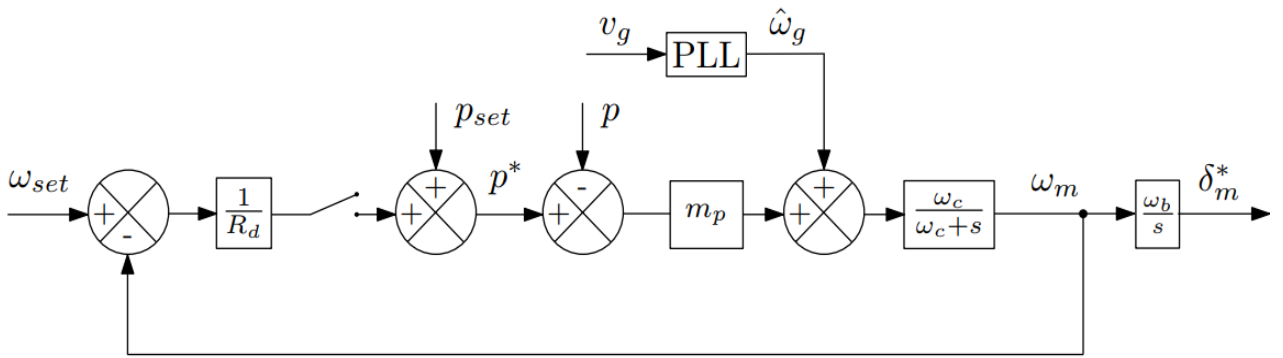


Figure 1.11. Droop-based grid-forming control

The relation of the angular frequency,  $\omega_m$ , to the active power is expressed in Equation 1.11:

$$\frac{1}{m_p \omega_c} \frac{d\omega_m}{dt} = p^* - p - \frac{1}{m_p} (\omega_m - \hat{\omega}_g) \quad (1.11)$$

From Equation 1.9 the analogy between droop-based grid-forming control and a VSM can be drawn and the inertia and damping constant can be deduced as in Equations 1.12 – 1.13:

$$2H = \frac{1}{m_p \omega_c} \quad (1.12)$$

$$K = \frac{1}{m_p} \quad (1.13)$$

- PLL-free grid-forming control

There is another type of a grid-forming control that is also analogous to a VSM [65]. The advantage of this type is that a PLL is not needed to decouple the inertial effect and frequency support. The control block scheme is demonstrated in Figure 1.12. It consists of an IP controller and an integrator to generate the angle reference. The proportional action with a damping gain,  $k_p$ , has to damp potential power oscillations, while the double integrator allows suppressing the error between the active power and its reference. To derive the equivalence with a VSM, a static model of the active power transfer is added. It includes a per-unitized model of the connection impedance ( $x_c$ ) and the grid reactance ( $x_g$ ) because there is no information about the PCC voltage [66]. It means that active power dynamics are sensitive to the value of the grid impedance.

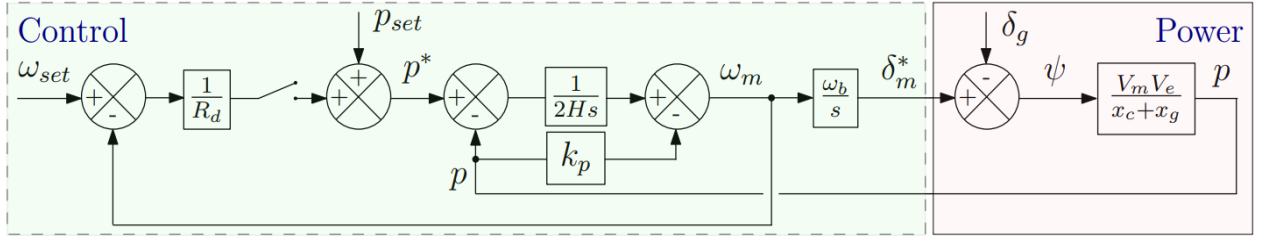


Figure 1.12. IP-controller based active power control

The relation of the frequency,  $\omega_m$ , to the active power for the IP controller is expressed in Equation 1.14:

$$\omega_m = \frac{1}{2Hs} (p^* - p) - k_p p \quad (1.14)$$

Equation 1.5 can be rewritten with angular frequencies instead of phasor angles:

$$p = \frac{V_m V_e}{x_c + x_g} \frac{(\omega_m - \omega_g) \omega_b}{s} = K_c \frac{(\omega_m - \omega_g) \omega_b}{s} \quad (1.15)$$

where  $K_c = \frac{V_m V_e}{x_c + x_g}$

The term  $k_p p$  in Equation 1.14 can be replaced with Equation 1.15:

$$\omega_m = \frac{1}{2Hs} (p^* - p) - k_p K_c \frac{(\omega_m - \omega_g) \omega_b}{s} \quad (1.16)$$

Equation 1.16 can be re-arranged as follows:

$$2H \frac{d\omega_m}{dt} = (p^* - p) - 2H k_p K_c (\omega_m - \omega_g) \omega_b \quad (1.17)$$

This equation resembles the expression of the angular frequency with a VSM in Equation 1.9. It can be noted that the inertia constant is similar, but the damping constant is related as:

$$K = 2Hk_pK_c\omega_b \quad (1.18)$$

Considering that the  $V_m = V_e = 1 pu$ , the power transfer for the IP-controller based active power regulation is expressed as:

$$\frac{p}{p^*} = \frac{1}{\frac{2H(x_c+x_g)}{\omega_b}s^2 + 2Hk_ps + 1} \quad (1.19)$$

Based on Equation 1.19, the damping gain is calculated with respect to a required damping  $\xi$ :

$$k_p = \xi \sqrt{\frac{2(x_c+x_g)}{H\omega_b}} \quad (1.20)$$

The natural frequency of the active power control can be expressed as  $\omega_n = \sqrt{\frac{\omega_b}{2H(x_c+x_g)}}$ .

Based on the requirements for  $\xi$  and  $\omega_n$ , the parameters of the  $k_p$  and  $H$  can be selected.

This type of a grid-forming control does not require a PLL to decouple frequency support and inertial effect. Therefore, it will be used for the rest of the manuscript.

### Converter voltage magnitude regulation

To control the voltage magnitude of a converter, the voltage magnitude reference,  $V_m^*$ , shown in Figure 1. can be set constant or varied with a certain rule. The structure of the voltage reference generation utilized in this thesis is presented in Figure 1.13.

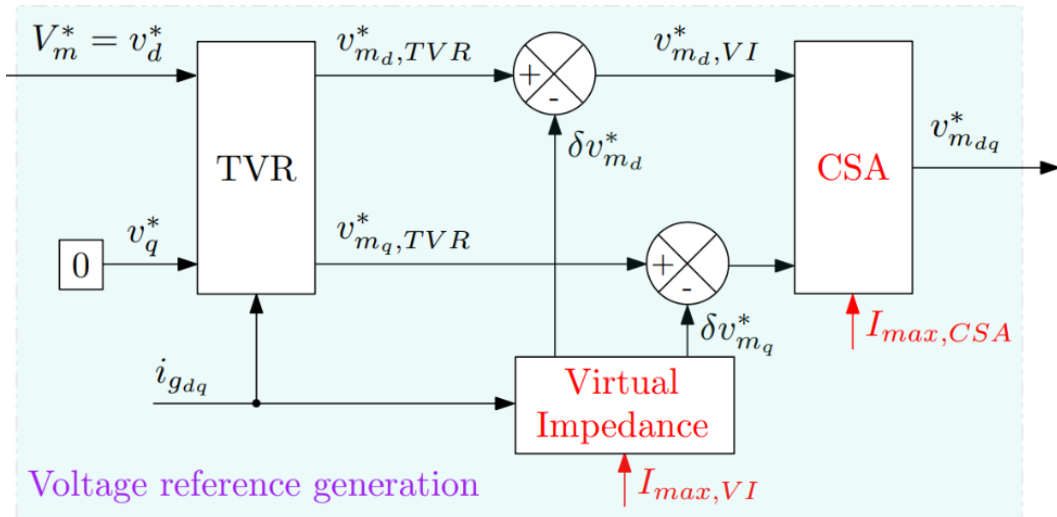


Figure 1.13. Power regulation with a grid-forming control

Figure 1.13 includes a transient virtual resistor (TVR), virtual impedance (VI) and a current saturation algorithm (CSA).

- Transient virtual resistor (TVR)

The voltage output of a converter can be kept constant according to the voltage  $V^*$ . However, it can result in synchronous oscillations since the transmission line dynamics are undamped [18], [67]. This is because the line reactance is significantly greater than the line resistance in a transmission system. To damp the dynamics of the grid current and to ensure frequency decoupling between the grid current and the active power control, a transient virtual resistor (TVR) is added. Its expression is the following:

$$v_{m_{dq},TVR}^* = v_{dq}^* + \frac{r_{TVR}S}{S + \omega_{TVR}} i_{g_{dq}} \quad (1.21)$$

where  $r_{TVR}$  is the TVR resistance,  $\omega_{TVR}$  is the TVR HPF cut-off frequency.

- Virtual impedance (VI)

The VI plays the role of an additional impedance added virtually during overcurrent periods. The VI reduces the output voltage of a converter and allows limiting the output current.

The expressions of a VI are given below:

$$x_{VI} = \begin{cases} k_{p_{RVI}} \delta I \sigma_{x/r} & \text{if } \delta I > 0 \\ 0 & \text{if } \delta I \leq 0 \end{cases} \quad (1.22)$$

$$r_{VI} = x_{VI} \sigma_{x/r}^{-1} \quad (1.23)$$

where  $k_{p_{RVI}} \delta I$  is the VI' proportional gain with a  $k_{p_{RVI}}$  computed based on  $I_{max,VI}$  [68],  $\delta I = I_s - 1$ ,  $I_s$  is the measured current,  $\sigma_{x/r}$  is the VI ratio.

The VI is activated once the  $I_s > 1.0$  pu. Then, the voltage references are modified as:

$$v_{m_{dq},VI}^* = v_{m_{dq},TVR}^* - \delta v_{m_{dq}}^* \quad (1.24)$$

where

$$\delta v_{m_d}^* = r_{VI} i_{g_d} - x_{VI} i_{g_q} \quad (1.25)$$

$$\delta v_{m_q}^* = r_{VI} i_{g_q} + x_{VI} i_{g_d} \quad (1.26)$$

The structure of a VI block is shown in Figure 1.14.

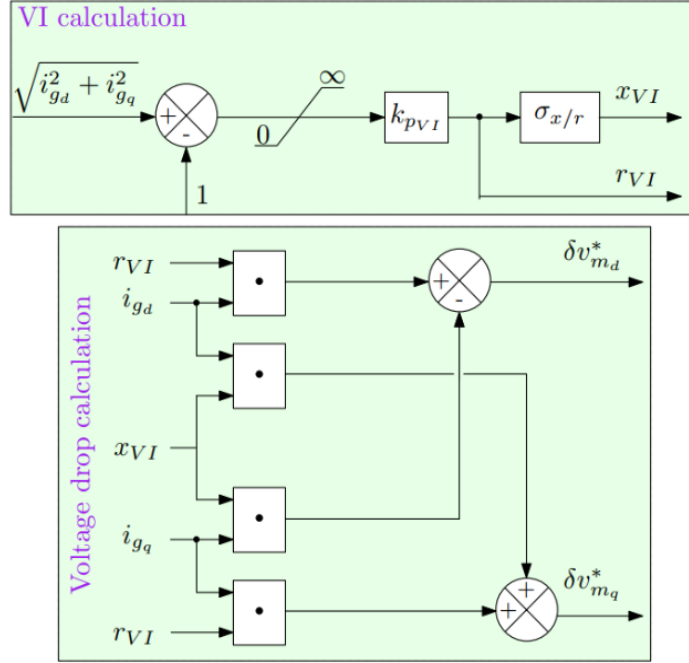


Figure 1.14. VI structure

- Current saturation algorithm (CSA)

Since a VI can be slow in the first moments of an overcurrent, a hybrid current limitation strategy including VI and CSA can be employed as proposed in [69]. The CSA has to serve as a saturation for current references. However, the converter is considered to be connected to the grid with only an RL connection impedance, so there is no extrinsic current control and current references to limit. Therefore, to implement a CSA, a threshold current loop (TCL) is added as demonstrated in [58] and reproduced in Figure 1.15. A solution is to include an inverse current control loop to generate current references, a CSA to limit these references and a current control loop to generate voltage references. The current control and the inverse current control can be implemented with a proportional gain,  $K_{pcc}$ , calculated as:

$$K_{pcc} = \frac{3}{l_f \tau_{cc}} \quad (1.27)$$

where  $\tau_{cc}$  is the settling time for a current controller.

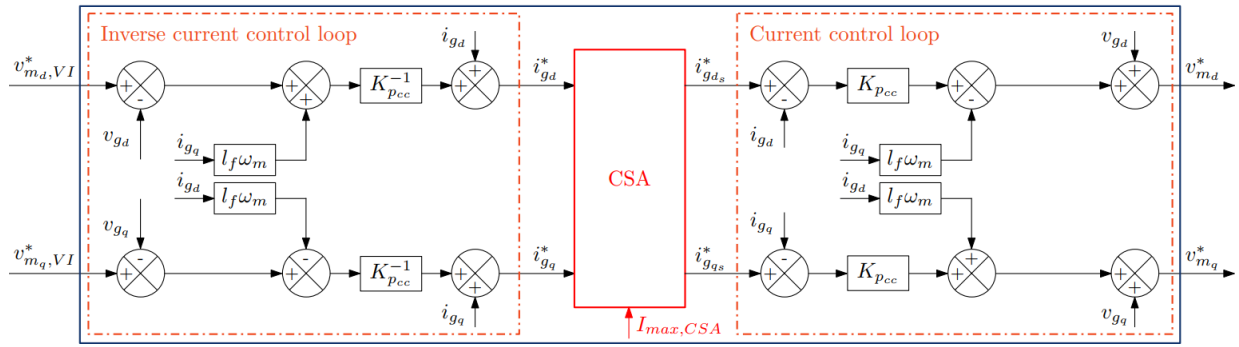


Figure 1.15. TCL

## 1.2. Wind turbine modelling

A wind turbine converts wind energy into the kinetic energy of the rotating parts. This kinetic energy is converted into electrical power by a generator connected to the turbine through a drivetrain. The control of a wind turbine ensures stable operation and maximizes power production. The generic model of a full-converter wind turbine is shown in Figure 1.16, where  $v_{wind}$  is the wind speed and  $\beta$  is the pitch angle.

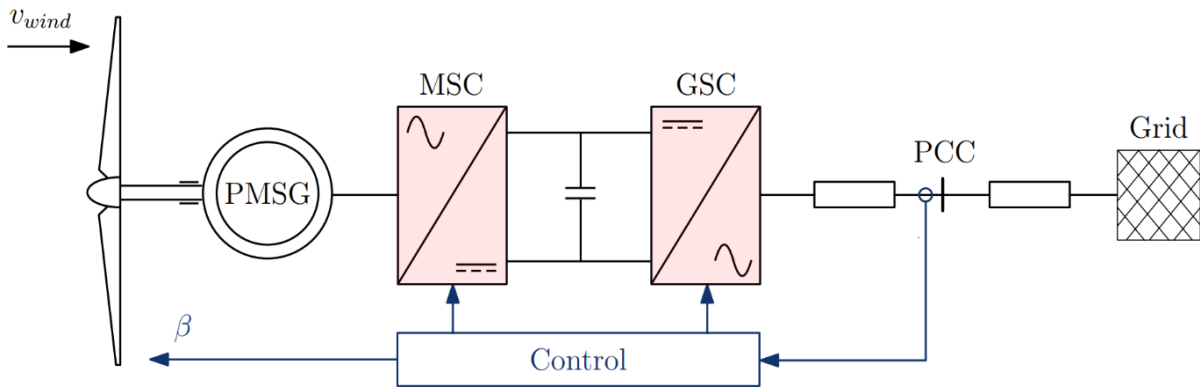


Figure 1.16. General structure of a Type-IV wind turbine

The model includes 5 main components:

- Turbine;
- Shaft;
- Generator;
- B2B converter;
- Control

A simplified block model of a wind turbine is demonstrated in Figure 1.17. To pay attention to the general parts of a wind turbine, the interface to the grid with a B2B converter is omitted. The B2B converter control will be extensively discussed in Section 1.3.

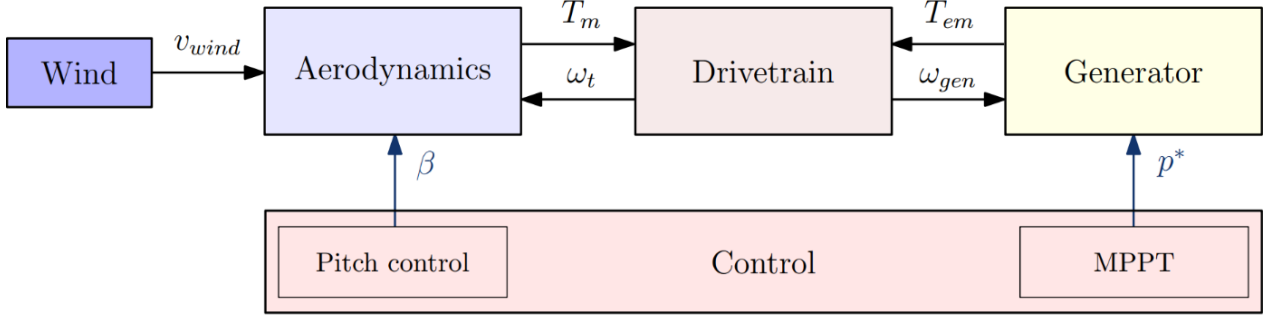


Figure 1.17. General components of a wind turbine

### 1.2.1. Aerodynamic model

The wind turbine rotor converts wind power into mechanical power. The wind power available at a wind turbine location can be calculated as:

$$P_{wind} = \frac{1}{2} \rho \pi R^2 v_{wind}^3 \quad (1.28)$$

where  $\rho$  is the air density,  $R$  is the wind turbine rotor radius,  $v_{wind}$  is the incident wind speed.

However, only a ratio of wind power can be harvested by a wind turbine. This ratio, known as the turbine performance coefficient or power coefficient, is usually expressed as a relation of the mechanical power,  $P_m$ , and wind power:

$$C_p(\lambda, \beta) = \frac{P_m}{P_{wind}} \quad (1.29)$$

The maximum theoretical value of the power coefficient is known as Betz limit and equal to 59.3 % [70]. The power coefficient also depends on the Tip-Speed Ratio (TSR),  $\lambda$ , and the pitch angle of the blades,  $\beta$ . The TSR can be expressed with the following relation:

$$\lambda = \frac{v}{v_{wind}} = \frac{\omega_t R}{v_{wind}} \quad (1.30)$$

where  $v$  is the velocity at the rotor tip.

Hence, the power captured by a wind turbine and the mechanical torque can be found as:

$$P_m = \frac{1}{2} \rho \pi R^2 C_p(\lambda, \beta) v_{wind}^3 \quad (1.31)$$

$$T_m = \frac{P_m}{\omega_t} \quad (1.32)$$

where  $\omega_t$  is the rotational speed of a wind turbine rotor.

The power coefficient can be found analytically by using the blade element method [71] or can be derived from Equation 1.33.

$$C_p(\lambda, \beta) = c_1(c_2 \lambda_i - c_3 \beta - c_4 \beta^x - c_5) e^{-c_6 \lambda_i} \quad (1.33)$$

$$\lambda_i = \frac{1}{\lambda + c_7 \beta} - \frac{c_8}{1 + \beta^3} \quad (1.34)$$

where coefficients  $c_1 - c_8$  and  $x$  depend on the wind turbine rotor type.

The mechanical torque can be also expressed with a torque coefficient as:

$$T_m = \frac{1}{2} \rho \pi R^3 C_t(\lambda, \beta) v_{wind}^2 \quad (1.35)$$

The relationship between power coefficient and torque coefficient is:

$$C_t(\lambda, \beta) = \frac{c_p(\lambda, \beta)}{\lambda} \quad (1.36)$$

The torque coefficient curves for different values of the pitch angle are demonstrated in Figure 1.18.

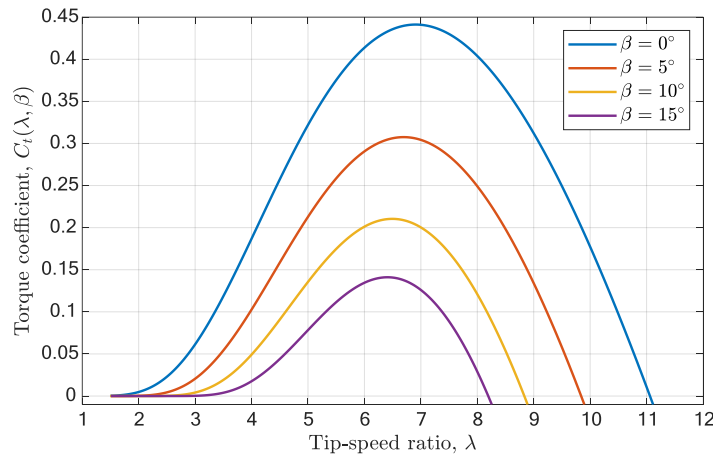


Figure 1.18. Torque coefficient characteristic as a function of TSR and pitch angle

### 1.2.2. Mechanical model

Wind turbine dynamics can contain different effects such as torsional dynamics, 3p torque oscillations and tower vibrations. Torsional dynamics imply torsional vibrations that can be excited in a flexible drivetrain due to the interaction of drivetrain components with wind variations or grid disturbances. 3p torque oscillations are a combination of wind shear and tower shadow effects. Wind shear implies a variation of the wind speed with height, while the tower shadow effect is the variation of the wind speed due to the presence of a tower. The wind shear and tower shadow effect result in mechanical torque oscillations with a frequency of 3p where p is a rotation frequency of the wind turbine rotor. Tower vibrations are generally caused by external dynamic forces. These can be blades vibrations or wind pressure. In this thesis, the focus is only on torsional vibrations.

The mechanical model of a wind turbine includes a drivetrain comprised of a turbine, shaft and a generator. The drivetrain can be represented with a three, two- or one-mass models. Depending on the analysis to be conducted, one of these models can be selected. In general, for the purposes of power system studies, a one-mass or two-mass model is considered. However, more often, a two-mass model is preferred since it can help to reflect the low-frequency turbine dynamics [72].

A one-mass model is depicted in Figure 1.19 and mathematically described by Equation 1.37:

$$(J_t + J_{gen}) \frac{d\omega_{gen}}{dt} = T_m - T_{em} - (D_t + D_{gen})\omega_{gen} \quad (1.37)$$

where  $J_g$  is the rotor inertia,  $J_{gen}$  is the generator inertia,  $\omega_{gen}$  is the rotational speed of a wind turbine generator,  $T_{em}$  is the electromagnetic torque imposed by generator,  $D_t$  and  $D_{gen}$  are the turbine and generator self-damping coefficients expressing losses due to aerodynamic resistance and mechanical friction.

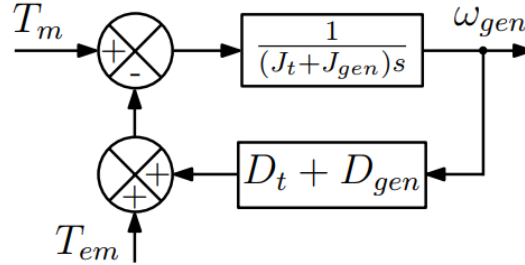


Figure 1.19. One-mass model of a drivetrain

In a two-mass model the mechanical drivetrain consists of separate masses of a wind turbine' and generator' rotor interconnected with a flexible shaft resembling a spring with a damper. Its mathematical representation is shown in Figure 1.20.

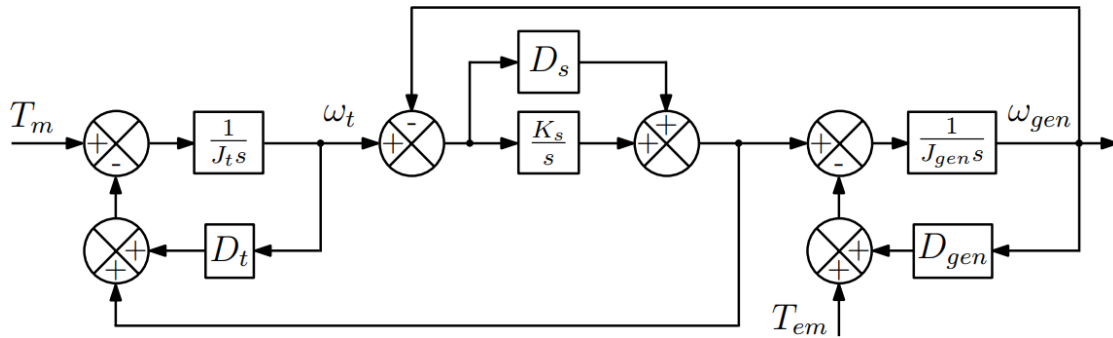


Figure 1.20. Two-mass model of a drivetrain [73]

The mathematical expression of a two-mass model is provided as:

$$J_t \frac{d\omega_t}{dt} = T_m - K_s\theta - D_s\dot{\theta} - D_t\omega_t \quad (1.38)$$

$$J_{gen} \frac{d\omega_{gen}}{dt} = K_s\theta + D_s\dot{\theta} - T_{em} - D_{gen}\omega_{gen} \quad (1.39)$$

where  $K_s$  is the shaft stiffness coefficient,  $D_s$  is the mutual damping coefficient,  $D_t$  is the turbine self-damping,  $D_{gen}$  is the generator' self-damping, and  $\dot{\theta} = (\omega_t - \omega_{gen})$  is the shaft displacement.

The mechanical model can also be represented in a per-unit system. To convert it from the system of international units to the per unit system, Equations 1.38 – 1.39 have to be divided by the base torque,  $T_b = \frac{P_b}{\omega_b^{mech}}$ . The result of a per-unitized model is presented for a turbine mass. For the generator mass, it can be derived analogously.

$$2H_t \frac{d\omega_t^{pu}}{dt^{pu}} = T_m^{pu} - K_s^{pu} \theta - D_s^{pu} \dot{\theta} - D_t^{pu} \omega_t^{pu} \quad (1.40)$$

where  $T^{pu} = \frac{T}{T_b}$  is the torque in per-unit system,  $T_b = \frac{P_b}{\omega_b^{mech}}$  is the base torque,  $P_b$  is the base power,  $\omega_b^{mech}$  is the base mechanical angular speed,  $\omega_t^{pu} = \frac{\omega_t}{\omega_b^{mech}}$  is the per-unitized turbine rotational speed,  $K_b = \frac{T_b}{\omega_b^{mech}}$  is the base stiffness,  $D_b = \frac{T_b}{\omega_b^{mech}}$  is the base damping,  $H_t = \frac{0.5J_t\omega_b}{T_b}$  is the turbine inertia constant.

The graphical representation of the drivetrain model in a per-unit system is shown in Figure 1.21.

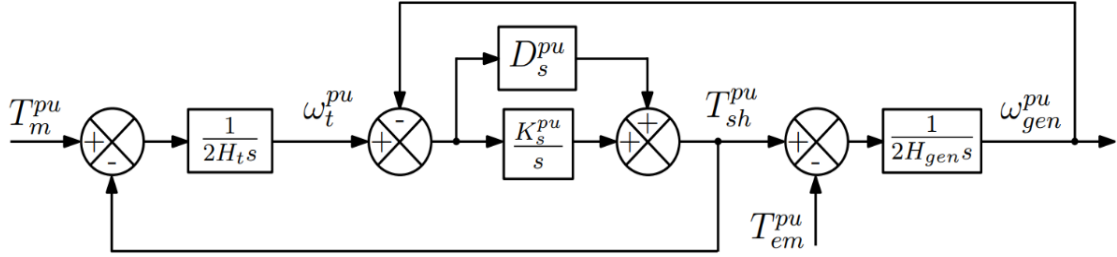


Figure 1.21. Two-mass model of a drivetrain in a per-unit system

The mechanical model of a drivetrain can be also presented in the power form because the power and the torque variations in a per-unit system are of the same order of magnitude. The modelling utilized in this thesis is based on the torque form described in Equation 1.40.

### 1.2.3. Generator model

The mechanical power from the full converter wind turbine topology considered in this thesis is converted to electrical power by a PMSG. The rotation of turbine rotor is transmitted to the PMSG rotor with a shaft between them. The rotation of the PMSG rotor induces the electromotive force and current in the stator windings. A PMSG model can be described in per unit system in a d-q frame as in [74]:

$$u_{sd} = -r_s i_{sd} - l_s \frac{di_{sd}}{dt} - \omega_{elec} l_s i_{sq} \quad (1.41)$$

$$u_{sq} = -r_s i_{sq} - l_s \frac{di_{sq}}{dt} + \psi_m \omega_{elec} + \omega_{elec} l_s i_{sd} \quad (1.42)$$

$$T_{em} = \frac{3}{2} \psi_m i_{sq} \quad (1.43)$$

Where  $i_{sd}$  is the d-axis generator output current,  $i_{sq}$  is the q-axis generator output current,  $u_{sd}$  is the d-axis generator output voltage,  $u_{sq}$  is the q-axis generator output voltage,  $r_s$  is the stator resistance,  $l_s$  is the stator inductance,  $\omega_{elec} = p\omega_{gen}$  is the electrical generator speed,  $p$  is the number of pole pairs of a generator,  $\psi_m$  is the flux linkage produced by a permanent magnet.

The control of a PMSG can be performed with the field-oriented current control, such that the d-q-axis voltage references can be expressed as:

$$v_{sd}^* = \left( K_p + \frac{K_i}{s} \right) (i_{sd}^* - i_{sd}) + l_s \omega_{elec} i_{sq} \quad (1.44)$$

$$v_{sq}^* = \left( K_p + \frac{K_i}{s} \right) (i_{sq}^* - i_{sq}) - l_s \omega_{elec} i_{sd} \quad (1.45)$$

The model of a PMSG and its control in a synchronous d-q frame are depicted in Figure 1.22. The inner control for a PMSG includes a current control that generates the voltage references. The outer loop generating a power/electromagnetic torque reference will be described in Section 1.3.

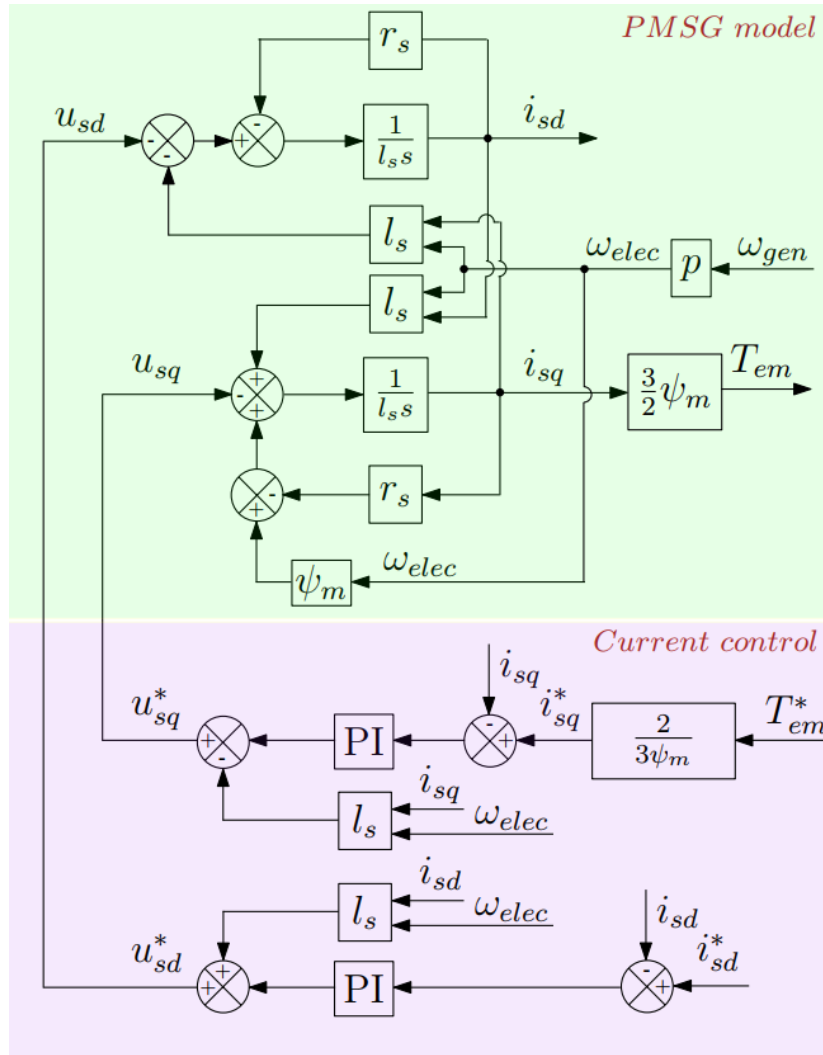


Figure 1.22. PMSG mathematical model and control in a d-q frame

## 1.2.4. Turbine control

A wind turbine can function in several operating zones. The ideal power curve and corresponding operation zones are illustrated in Figure 1.23. Depending on a zone, a different control mode can be active.

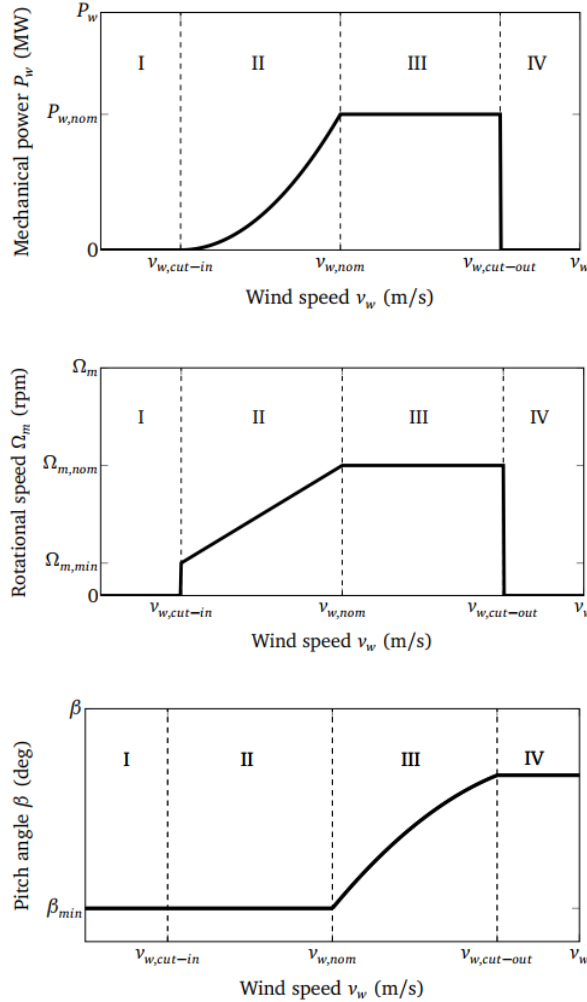


Figure 1.23. Wind turbine operating zones as a function of the wind speed [75]

Zone I. Below the cut-in wind speed, the wind turbine is not rotating due to insufficient mechanical torque, so there is no mechanical power.

Zone II. If the incident wind speed falls between cut-in and nominal wind speed, the wind turbine produces the maximum power available for the given wind speed by following the optimal tip-speed ratio. This is achieved with the regulation of the generator' rotational speed by the MPPT. The MPPT curve can be characterized by the expression below:

$$P_{mppt}^*(\omega_{gen}) = \frac{1}{2} \rho A C_{p,opt} \left( \frac{\omega_{gen} R_{wt}}{\lambda_{opt}} \right)^3 \quad (1.46)$$

Zone III. At nominal wind speed, the wind turbine produces the nominal power. With the increase in wind speed, the rotating speed of the turbine tends to increase. To avoid its increase beyond an operational limit, the pitch control keeps the rotational speed constant at the nominal

value by regulating the angle of turbine blades. The pitch control can be implemented either with a simple PI controller or with a PI controller with a gain scheduling [76]. The latter allows compensating for the variations in the aerodynamic characteristics of the wind turbine. The pitch control implemented with a gain scheduling is shown in Figure 1.24.

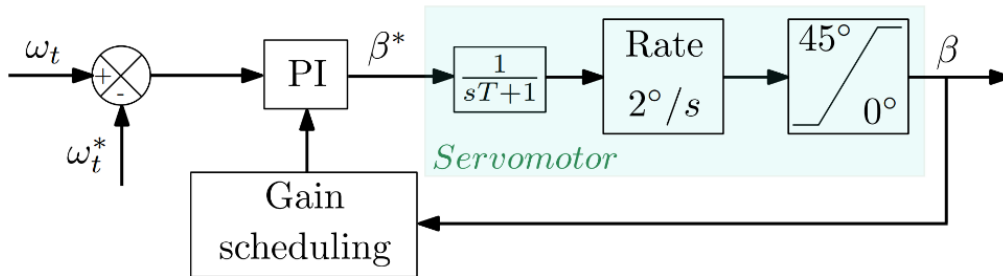


Figure 1.24. Pitch control

Zone IV. At the cut-out wind speed, the pitch angle reaches its maximum. Increasing the wind speed further could thus significantly damage the wind turbine. Therefore, in this zone, the wind turbine rotation is completely prevented and the turbine is halted.

The described zones correspond to the idealized case. In a real wind turbine there is an additional operating zone between Zone II and Zone III where the rotational speed of a wind turbine reaches almost its rated rotational speed, although the rated nominal power is not reached yet [42]. For this zone, the power reference of the MPPT can be set with a steep inclination in order to avoid sudden discontinuity in the power reference.

### 1.3. Control of a B2B converter in a Type-IV wind turbine

In this section, the main focus is on the control strategy of a grid-forming wind turbine. Firstly, the classical control strategy of a grid-following wind turbine is recalled. Secondly, the possible control strategies for a grid-forming wind turbine are presented. Finally, the most suitable control strategy is tested for the case study of a 5 MW wind turbine.

#### 1.3.1. Classical control for a grid-following wind turbine

A Type-IV wind turbine interfaced to the AC grid with a grid-following converter needs to have a proper control so that the available power is supplied to the grid and the power balance between generated and transmitted power is retained. Contrary to the Type-I to Type-III wind turbines, a Type-IV wind turbine is connected to the grid with a fully rated B2B converter [77]. To ensure stable operation of the wind turbine and provide the maximum power output, the MSC and the GSC of the B2B converter have to be properly controlled. A classical control for a grid-following wind turbine implies that the MSC is in charge of controlling the power transfer from the wind turbine generator, while the GSC is responsible for controlling the DC bus voltage by balancing the power coming to the MSC and the power supplied from the GSC. This classical control strategy has been used for years to control Type-IV wind turbines, as it is quite intuitive to control the power flow at the MSC [78]. With such a control, the wind turbine generator is

mechanically decoupled from the grid [79] and supplies only the power defined by the incident wind. In case, however, there is a need for the wind turbine to provide additional services to the grid, such as synthetic inertia or frequency support, it can be coupled by means of additional control modifications [30], [80].

The Type-IV wind turbine with a classical grid-following control is depicted in Figure 1.25. The MSC and the GSC control include outer and inner loops. For the MSC, the outer loop generates the q-axis current reference based on the power reference from the MPPT. The d-axis current,  $i_{sd}^*$ , can be set to 0 to limit the reactive power exchange between the converter and the machine. For the GSC, the outer loop is in charge of controlling the DC bus voltage by modifying the d-axis current reference,  $i_{gd}^*$ . The control of reactive power can also be implemented by controlling the q-axis current reference,  $i_{gq}^*$ . The d-q – abc conversion is based on the PLL's voltage phase angle. The inner loop for both converters contains a fast current controller. If required, inertial support from the wind turbine can be included by adding the control loop generating a power surplus  $\Delta p$  derived from a grid frequency measurement.

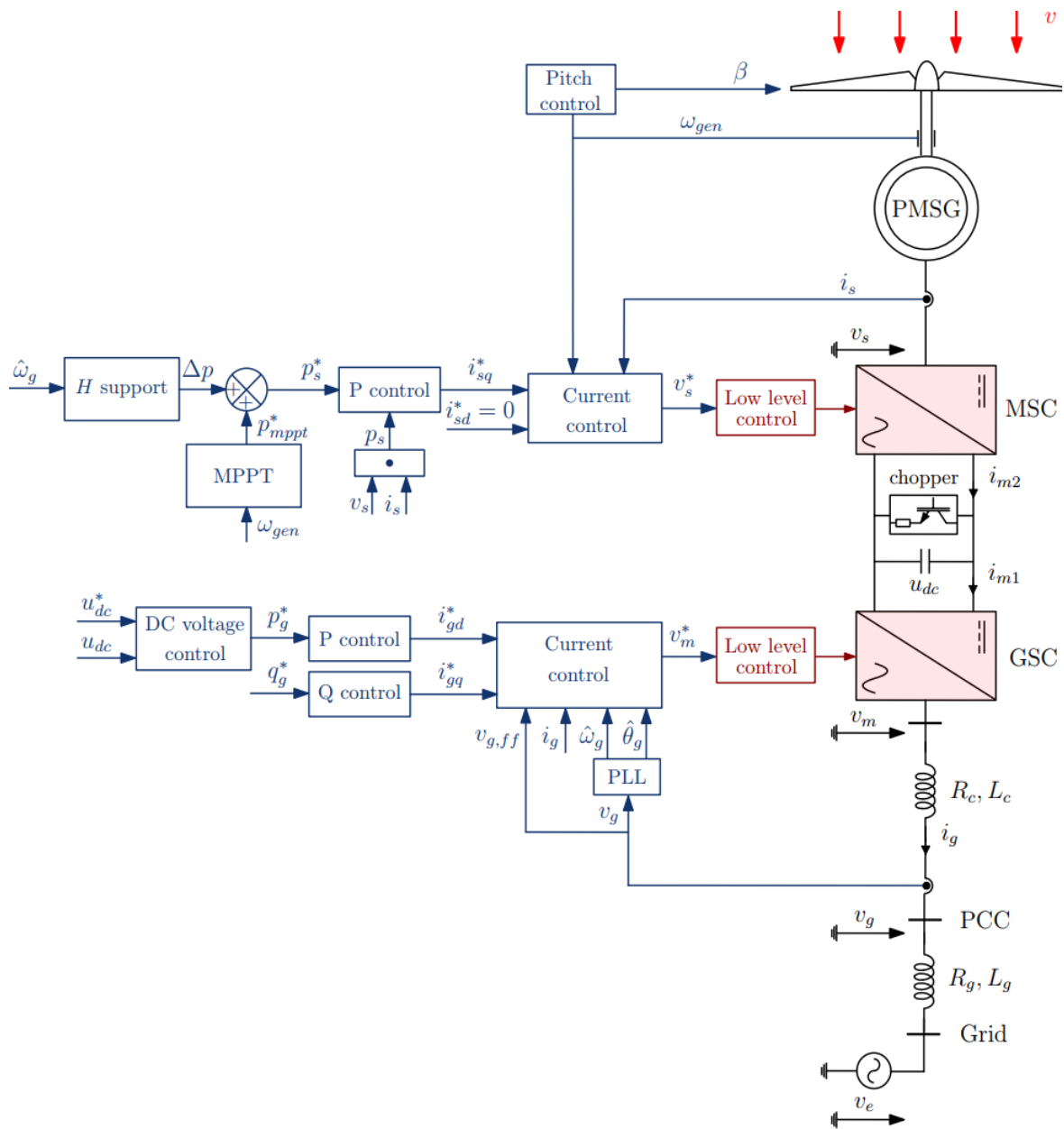


Figure 1.25. Type-IV wind turbine with a grid-following control

### 1.3.2. Control strategies for a grid-forming wind turbine

The classical control strategy can be applied to a grid-forming wind turbine as shown in Figure 1.26 where the reference for a grid-forming control is from the DC bus voltage controller. This control strategy is named as  $U_{dc}$  – control strategy.

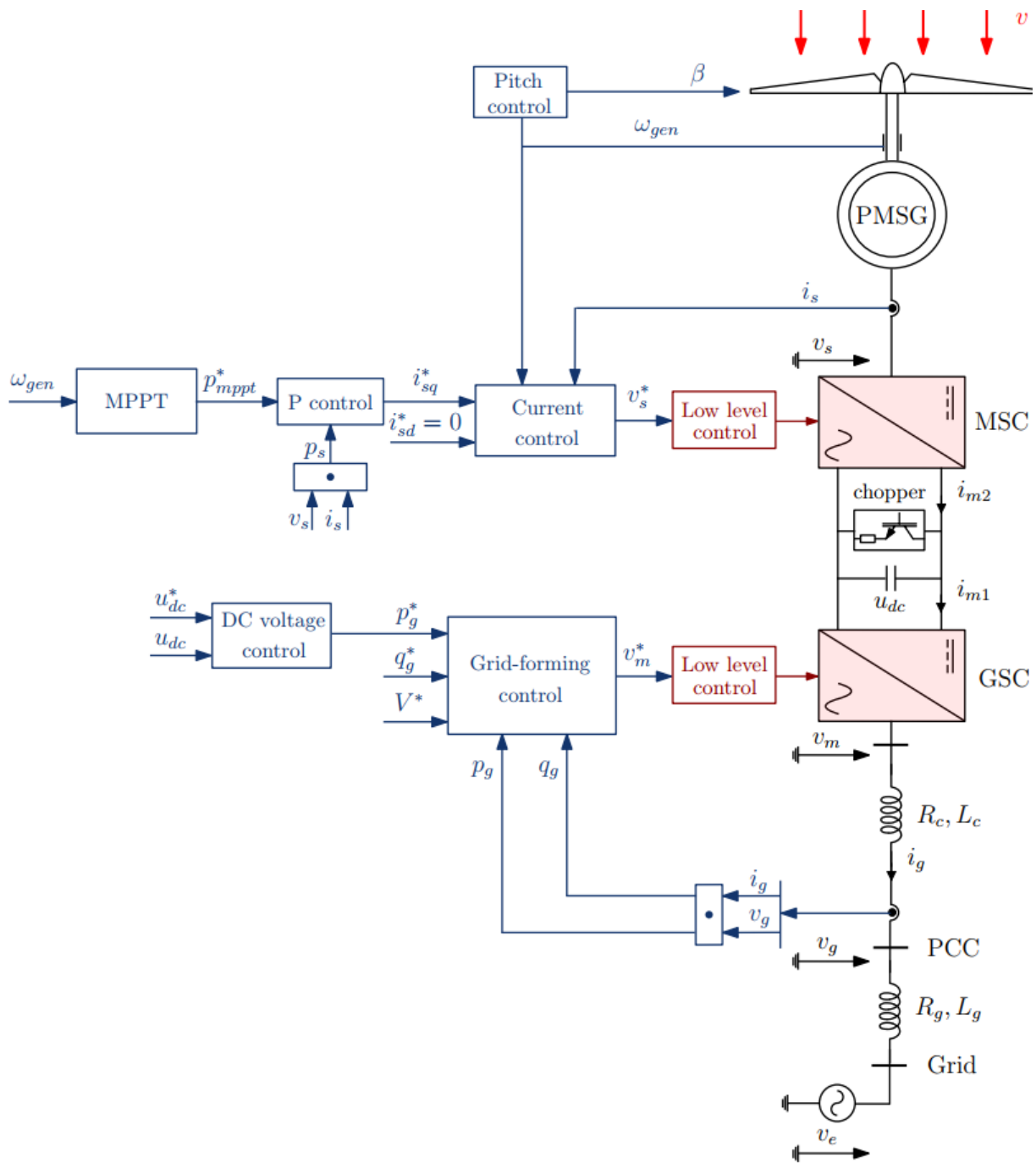


Figure 1.26.  $U_{dc}$  – control strategy

For this strategy, inertia provision is managed by the active power control of the grid-forming control. So, there is no need to have the inertial support block on the MSC. One of the challenges with this control layout, is that the GSC has to achieve two tasks at the same time, namely DC voltage control and inertial support. These two tasks are contradictory. Indeed, in case of inertial support, the active power increases ( $p_g \neq p_g^*$ ). It results in a power imbalance on the DC side and the DC bus voltage decreases. Hence, the DC bus voltage controller tends to decrease the active power reference,  $p_g^*$ . These contradicting control actions can lead to instability, so this solution is not feasible, as mentioned and comprehensively discussed in [34], [42], [81]. Moreover, even if the inertial support is well coordinated between the GSC and the MSC, the outer control loop at

the GSC represented by the DC bus voltage controller has to be slow to prevent interactions with a grid-forming control that has a time response around hundreds of milliseconds. A slow DC bus voltage controller will not be able to rapidly compensate the power imbalance and, as a result, there will be significant variations in the DC bus voltage. Thus, in essence, with the  $U_{dc}$  – control strategy, the dynamics of the DC bus voltage and grid-forming control become coupled in one way or another, which makes this strategy not the right choice for controlling a grid-forming wind turbine.

To decouple the grid-forming control and the DC bus voltage control, another control strategy, implying switching the control responsibilities between the MSC and the GSC, has to be utilized. In this case, the MSC has to control the DC bus voltage, while the GSC maintains optimal power transfer. This strategy is also used for grid-following wind turbines with the purpose of damping of torsional vibrations [76]. In this thesis, this strategy is named as  $p$  – control strategy. The  $p$  – control strategy is presented in Figure 1.27 with a simplified wind turbine model. In this scheme, there is no additional block for inertial support and no need to coordinate the inertia between the MSC and the GSC because the wind turbine generator is linked to the grid by means of the DC bus voltage control.

From a visual analysis of the model in Figure 1.27, it is important to note that the power reference for the grid-forming control relies on the MPPT reference, which in its turn depends on the rotational speed of a turbine. This coupling between the wind turbine and the GSC will have a certain impact on the inertial response provision. In addition, the coupling of the wind turbine generator with the grid-forming control through the DC bus voltage regulator can result in rapid variations of the electromagnetic torque, and these fast torque variations can have a negative effect on the mechanical structure of a wind turbine. These issues will be addressed in detail in Chapter 2.

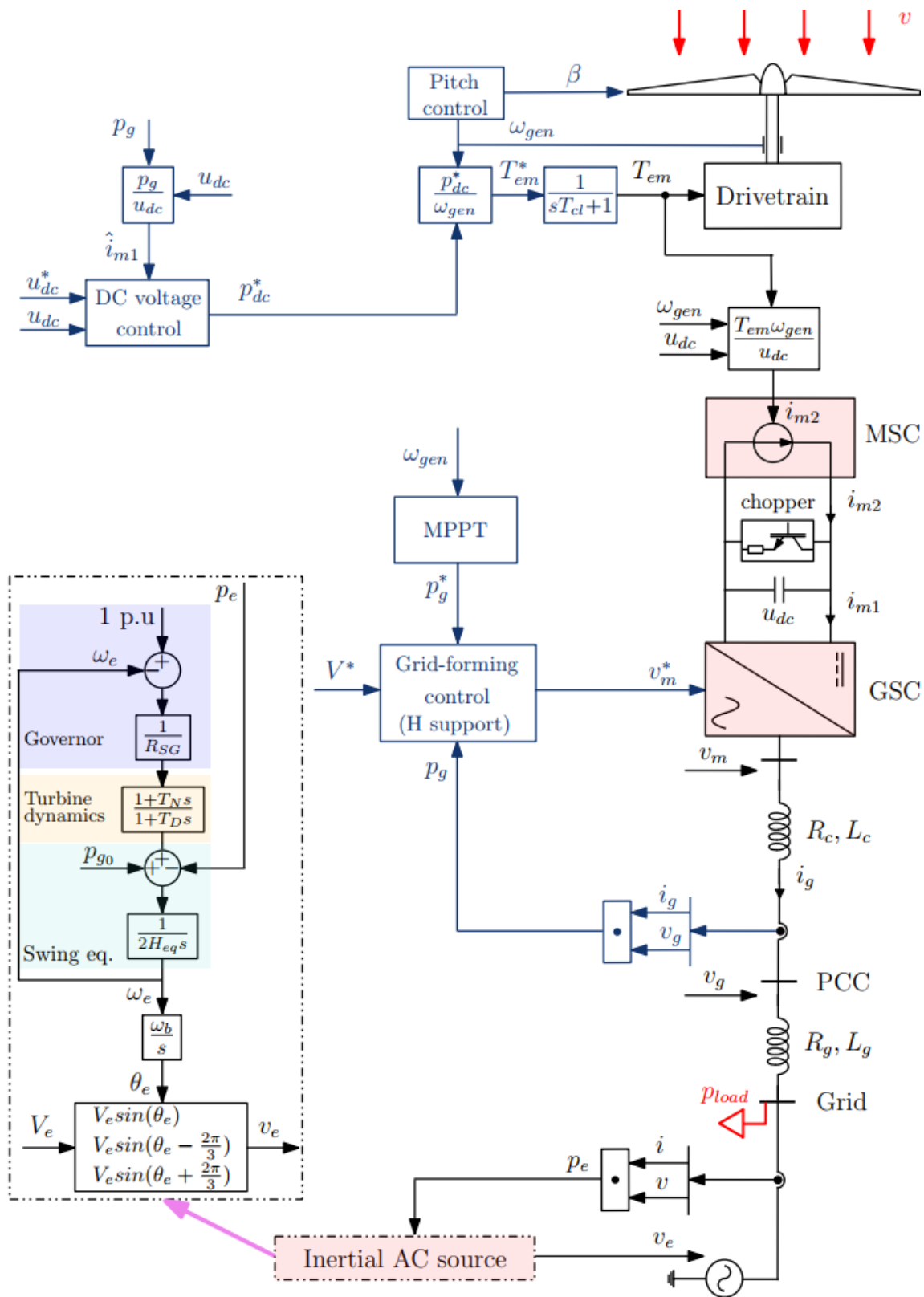


Figure 1.27. Simplified model of a wind turbine with  $p$  – control strategy

To demonstrate the performance of a grid-forming wind turbine with the considered  $p$  – control strategy, an analysis for a case study 5-MW Type-IV wind turbine has been carried out. The modelling of the system elements and corresponding assumptions are provided in Table 1.2.

Table 1.2. System modelling and assumptions

Element	Modelling, assumptions
Grid	<p>simplified SM model including the dynamics of a turbine, a governor and a mechanical model with an equivalent inertia.</p> <p>This model provides an approximation for the behavior of the grid. For the analysis performed in this thesis such model is sufficient. A more detailed grid model can also be used for investigations of a bigger scale.</p>
Load	constant resistive load
Wind speed	constant value
Wind turbine	<ul style="list-style-type: none"> <li>mechanical model with a one-mass drivetrain, the losses in a drivetrain are neglected;</li> <li>PMSG and MSC are simplified to a controlled current source.</li> </ul>
Control	<ul style="list-style-type: none"> <li>MSC current controller is replaced with a LPF with a time constant, <math>T_{cl} = 10 \text{ ms}</math>;</li> <li>MPPT, pitch control is modeled as in Section 1.2;</li> <li>DC bus voltage control shown in Figure 1.28 is modeled as a PI controller with an anti-windup. In addition, a feed-forward compensation term with a delay of 5 ms is used to improve the controllability of the DC bus voltage. The feed-forward term is GSC current, <math>\hat{i}_{m1}</math>; estimated as <math>\frac{p_g}{u_{dc}}</math>;</li> <li>DC chopper is implemented with a resistance, <math>r_{dc}</math>, and a switch controlled with a hysteresis relay, R1. The switch on and off values are <math>u_{dc,on} = u_{dc,max}</math>, <math>u_{dc,off} = 0.99u_{dc,max}</math>. The R1 generates <math>y_{chop}</math> to fix DC bus voltage controller integrator;</li> <li>Grid-forming control includes the IP controller with a de-activated frequency support, and current saturation described in Section 1.1.3.</li> </ul>

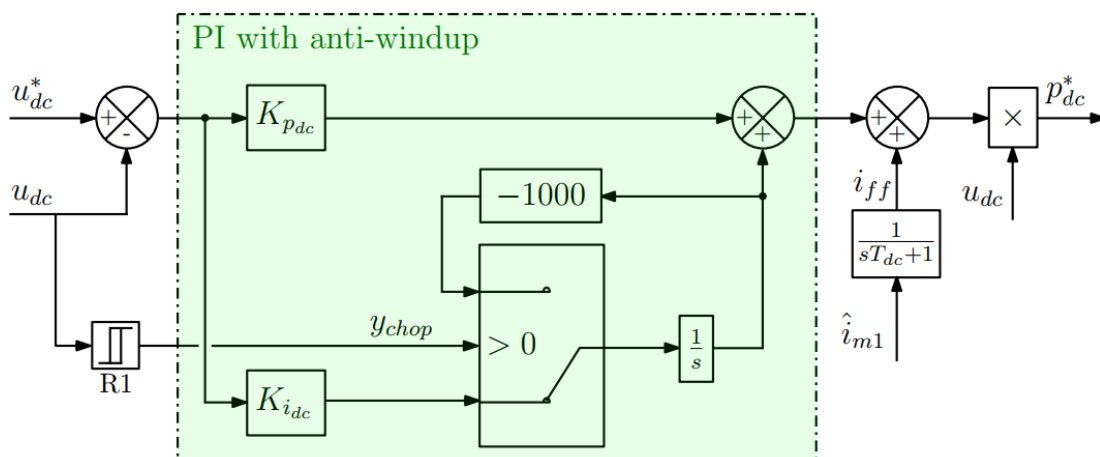


Figure 1.28. DC bus voltage control with an anti-windup

The parameters of the system model are provided in Table 1.3 – Table 1.5.

Table 1.3. Grid parameters

Parameter	Value
Nominal grid power, $S_g$	5 MW
Nominal grid voltage, $U_g$	690 V
Short-circuit ratio, $SCR$	10
$R/X$ ratio	1/10
Converter connection impedance, $r_c, l_c$	0 pu, 0.15 pu
<b>Simplified SM parameters:</b>	
Steam turbine constants: $T_N, T_D$	1, 6
Frequency droop, $R_{SG}$	4 %
Equivalent inertia constant, $H_{eq}$	5 s

Table 1.4. Parameters of wind turbine generator and DC bus

Parameter	Value
Wind turbine nominal power, $P_{wt}$	5 MW
Cut-in, rated rotational speed, $\omega_{t,nom}$	0.56 rad/s, 1.27 rad/s
Cut-in, Rated, Cut-out wind speed, $v$	3 m/s, 11.4 m/s, 25 m/s
Turbine rotor radius, $R_{wt}$	63 m
Optimal tip-speed ratio, $\lambda_{opt}$	7
Optimal power coefficient, $C_{p,opt}$	0.44
Shaft stiffness, $K_s^{pu}$	280 pu
Shaft mutual damping, $D_s^{pu}$	1 pu
Turbine inertia constant, $H_t$	1.93 s
Generator inertia constant, $H_g$	0.8 s
Nominal DC bus voltage, $U_{dc}$	1500 V
DC bus capacitance, $C_{dc}$	0.17 F
Minimal and maximal DC bus voltage deviation, $u_{dc,min/max}$	0.9 pu / 1.1 pu

Table 1.5. Controller parameters

Parameter	Value
Grid-forming control inertia constant, $H$	3.5 s
Grid-forming control damping gain, $k_p$	0.0097
<b>TVR:</b>	
TVR resistance, $r_v$	0.09 pu
TVR HPF cut-off frequency, $\omega_{TVR}$	60 rad/s
<b>VI:</b>	
$x_{VI}, \sigma_{x/r}, k_{p_{RVI}}, I_n, I_{max,VI}$	0.672, 5, 0.672, 1.0 pu, 1.2 pu
<b>TCL, CSA:</b>	
$\tau_{cc}, I_{max,CSA}$	30 ms, 1.25 pu
<b>PLL control:</b>	
Settling time, $\tau_{pll}$ , damping, $\xi_{pll}$	40 ms, 0.707
<b>DC bus voltage control:</b>	
Settling time, $\tau_{dc}$ , damping, $\xi_{dc}, T_{dc}$	2 s, 0.707, 0.005 s
<b>DC chopper:</b>	
DC resistance, $R_{dc}$ ,	0.45 Ohm
<b>Pitch control:</b>	
Settling time, $\tau_{pitch}$ , damping, $\xi_{pitch}$ , time constant, $T_{pitch}$	4 s, 0.707, 0.1 s

The operation of the grid-forming wind turbine with  $p$  – control strategy is verified during a grid disturbance – a grid frequency variation with the RoCoF = 1 Hz/s – caused by a connection of a resistive load at 30 seconds. The incident wind speed is 11 m/s. The simulation results are provided in Figure 1.29, (a) – (d). As shown in Figure 1.29, (a), once the load is connected, there is a power imbalance in the power system, and the grid frequency reduces. Due to the inertial effect, the GSC' voltage angle does not react instantaneously. In Figure 1.29, (b) the difference between the grid angle and the GSC angle induces an increase of the active power. As soon as the transient is finished, the active power comes back to its initial value. The transient depends on the chosen value of the inertia constant of the grid-forming control.

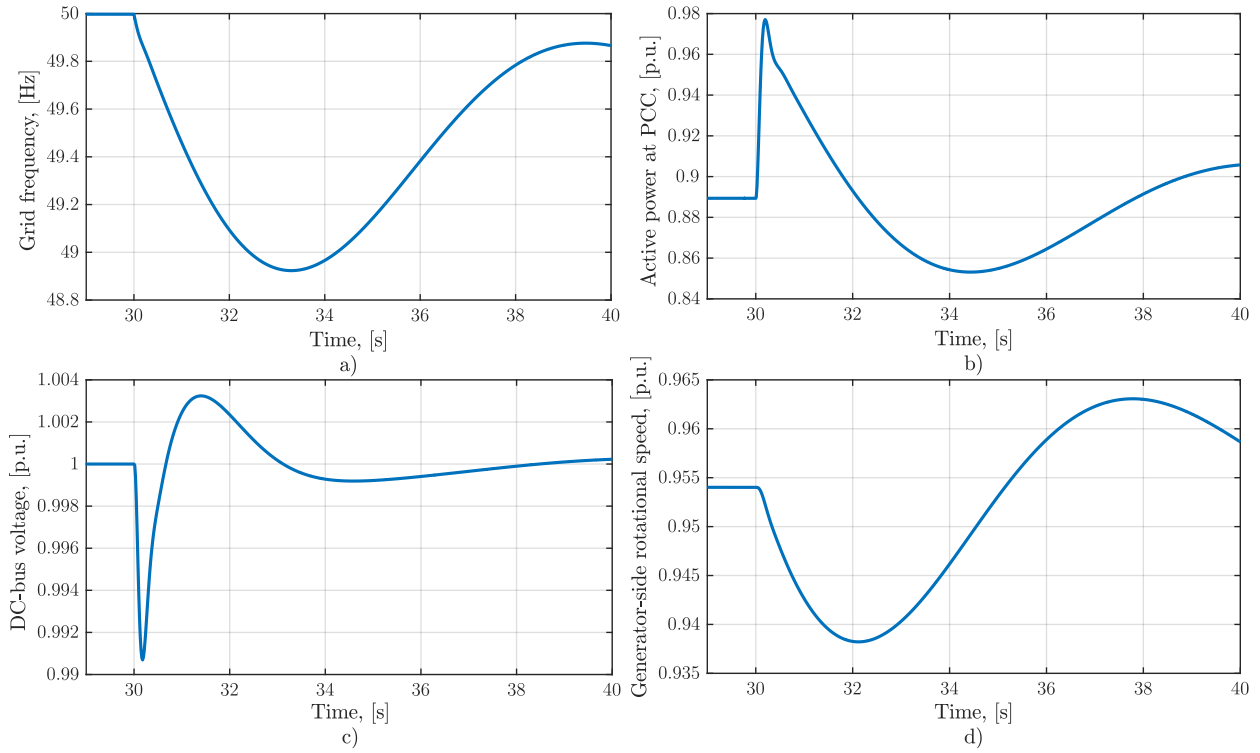


Figure 1.29. Behavior of a grid-forming wind turbine with  $p$  – control strategy: a) – grid frequency, b) active power at PCC, c) DC-bus voltage, d) electromagnetic torque

Given the time response of the DC bus voltage controller set as 2 s, the DC bus voltage reduction shown in Figure 1.29, (c), is within operational limits, which are 0.9 – 1.1 pu. The feed-forward compensation term in the DC bus voltage control allows ensuring the controllability of the DC bus voltage. However, with this term, the grid disturbance also propagates faster to the MSC and results in a rapid reaction of the wind turbine generator’ electromagnetic torque shown in Figure 1.29, (d). The provided results have demonstrated that  $p$  – control strategy can be used to manage the operation of the grid-forming wind turbine.

## Conclusions

In this chapter the modelling base for the grid-forming wind turbine has been prepared. The discussion and simulations in this chapter demonstrate that it is possible to integrate a grid-forming control into the GSC of a Type-IV wind turbine. The classical B2B converter control configuration that is used in case of a grid-following control is not suitable for a grid-forming wind turbine, as the GSC becomes prone to instabilities due to the need to perform several control functions simultaneously. So, in order to improve the controllability of the grid-forming wind turbine, the classical control strategy is modified by switching the controls between the MSC and the GSC. This modified strategy is called as *p-control strategy*. However, it was emphasized that the *p-control strategy* can create electromechanical couplings between the dynamics of a wind turbine and the dynamics of a grid-forming control. This will be the subject of the next chapter.

## 2. Electromechanical couplings in a grid-forming wind turbine

This chapter discusses the electromechanical couplings that exist in a grid-forming wind turbine. In the first section, the coupling between the mechanical dynamics of the wind turbine and the dynamics of a grid-forming control is discussed. This coupling is the consequence of the chosen position of the MPPT in the control configuration of the B2B converter. The negative impact on the grid-forming control, as a result of this coupling, is presented and a solution is proposed to decouple both dynamics. The second section sheds light on a second coupling created due to the position of the DC bus voltage controller and linking the dynamics of the wind turbine generator and the dynamics of the grid-forming control. It is shown how the grid-forming control has an indirect impact on the mechanical structure of the wind turbine generator through the appearance of drivetrain torsional vibrations, affecting the wind turbine components. Possible solutions for damping of these vibrations in a grid-forming wind turbine are presented. Then, a novel damping solution based on the input shaping method is proposed. The control scheme is subjected to the thorough analysis in terms of the damping efficiency and robustness.

### 2.1. Influence of the wind turbine dynamics on the grid-forming control

This section touches the question related to the dynamics of the wind turbine and the grid forming control which are coupled with the MPPT. The objective is to explain this coupling and its effect on the inertial response from a grid-forming wind turbine. According to the  $p$  – control configuration of a grid-forming wind turbine presented in Section 1.3.2, the power reference that a grid-forming control receives depends on the MPPT of a wind turbine. The link between the MPPT and the grid-forming control is depicted in Figure 2.1 on the example of a VSM.

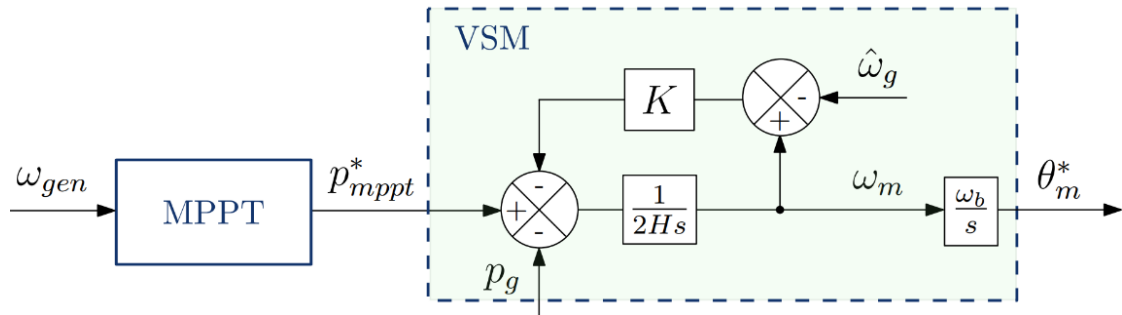


Figure 2.1. Coupling between MPPT and grid-forming control

The relationship between the MPPT and a VSM can be established as:

$$p_{mppt}^*(\omega_{gen}) - p_g = 2H \frac{d\omega_m}{dt} + K(\omega_m - \hat{\omega}_g) \quad (2.1)$$

From Equation 2.1, it is clear that if instead of a wind turbine, the grid-forming VSC is connected to a power source with the infinite amount of energy available at the DC bus, the active power reference entering the grid-forming control can be considered constant, and free from the influence of external dynamics. So, in the case of an infinite amount of energy available, there is no impact on the grid-forming control and on the inertial response from a grid-forming VSC in the sense that it should last until the grid frequency reaches the frequency nadir.

In a wind turbine, however, the power reference,  $p_{mppt}^*$ , is not constant and depends on the mechanical rotational speed of the wind turbine generator and the implementation of the MPPT strategy. The variation of the rotational speed can have an impact on the inertial response. To describe this impact, the one-mass drivetrain model of a wind turbine in the power form is recalled:

$$p_m(\omega_{gen}) - p_{em} = 2H_{wt} \frac{d\omega_{gen}}{dt} \quad (2.2)$$

where  $p_m$  is the mechanical power from the wind turbine,  $p_{em}$  is the electrical power from the wind turbine generator and  $H_{wt}$  is the overall inertia constant of the wind turbine.

Knowing that the wind turbine is linked to the grid with the control of the B2B converter, an approximation for the active power can be used, namely  $p_{em} = p_g$ . Equation 2.2 can now be transformed into:

$$p_m(\omega_{gen}) - p_g = 2H_{wt} \frac{d\omega_{gen}}{dt} \quad (2.3)$$

In steady-state at a constant wind speed, the wind turbine rotational speed is  $\omega_{gen0}$  and the power balance is retained,  $p_m(\omega_{gen0}) = p_g$ . In case of a grid disturbance resulting in a grid frequency reduction, the grid-forming GSC supplies additional power to the grid as if it was a rotating mass with inertia. From Equation 2.3, it can be deduced that in the beginning of the disturbance,  $p_m(\omega_{gen0}) < p_g$ . This power imbalance means that the kinetic energy is being extracted from the rotating masses of the wind turbine, so that the rotational speed reduces to  $\omega_{gen1}$ .

According to Equation 2.2, this decreased rotational speed will result in a reduction of the MPPT power reference  $p_{mppt}^*(\omega_{gen1}) < p_{mppt}^*(\omega_{gen0})$ . This reducing  $p_{mppt}^*$ , in turn will have a negative effect on the inertial response because it will impose a reduction of  $p_g$  during the grid disturbance. So, there are two contradictory effects at work. The first one is the increasing power output from the wind turbine by means of its inertial response. The second one is the MPPT that reduces the power reference as a result of reducing rotational speed of a wind turbine. Hence, it can be assumed that the inertial response provided from the grid-forming wind turbine will be smaller compared to a grid-forming VSC connected to an infinite power source.

To further illustrate that the dynamic interaction between the wind turbine and the grid-forming control results in a reduced inertial response, a comparison of inertial responses from a grid-forming VSC connected to an infinite power source and a grid-forming wind turbine is performed through time-domain simulations. The model of the grid-forming wind turbine considered for the simulation is the one described in Fig. 1.27. The same model is rearranged to acquire the model with a grid-forming VSC connected to an infinite power source. The parameters for the models are presented in Table 1.3 – Table 1.5. The grid disturbance is a frequency variation with  $RoCoF = 1 \text{ Hz/s}$  caused by a connection of a resistive load.

The simulation results are provided in Figure 2.2 – Figure 2.3. Figure 2.2 shows the impact of the power reference on the inertial response. Compared to the wind turbine, the VSC supplies additional active power for a longer period. It is possible to deduce from Figure 2.2, (b), that the reduced period of the inertial response is due to the power reference that depends on the wind

turbine dynamics and changes in time. Based on the results, it is indeed confirmed that the grid-forming wind turbine has a reduced inertial response compared to an infinite power source.

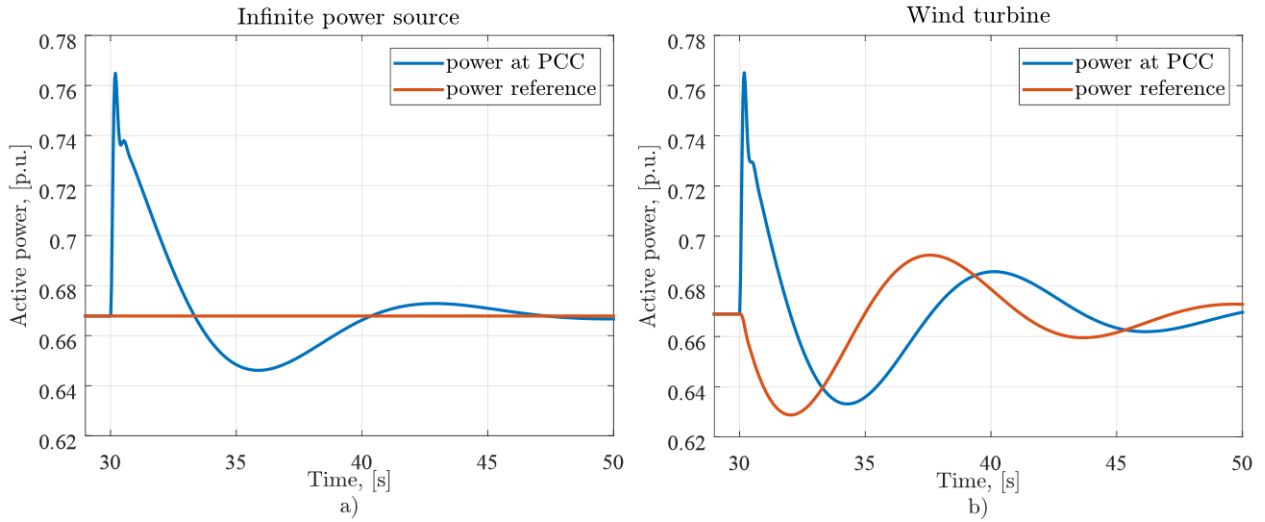


Figure 2.2. Impact of power reference on the inertial response provision, a) grid-forming VSC connected to an infinite power source, b) grid-forming VSC interfacing a wind turbine

In Figure 2.3, a comparison of the impact on the grid frequency from this inertial response is presented. The grid frequency supported by a grid-forming wind turbine has a lower frequency nadir. Also, the coupling between the wind turbine and a grid-forming control results in a more prominent second dip of the grid frequency.

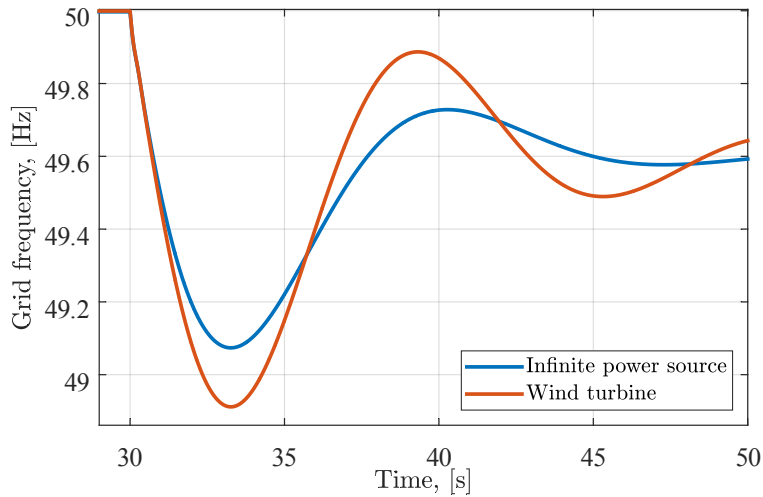


Figure 2.3. Impact of reduced effective inertia on the grid frequency

Moreover, if the inertia constant in a grid-forming control is increased, it can lead to further increase of the second frequency dip as shown in Figure 2.4. Also, the frequency nadir is not improved.

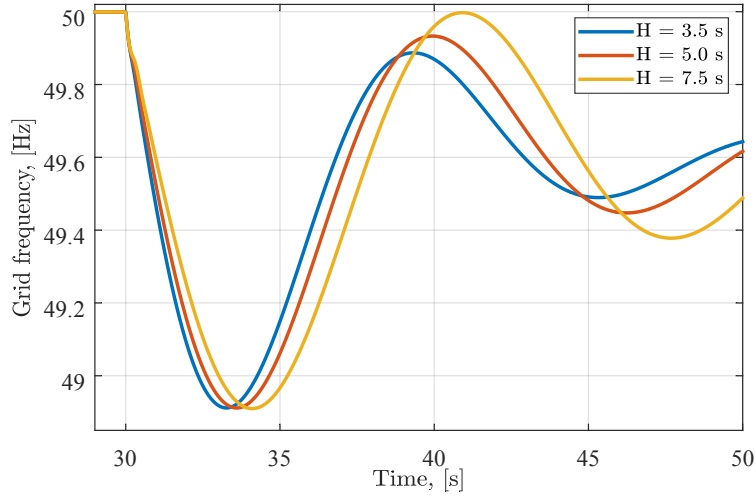


Figure 2.4. Impact of increased inertia constant in a grid-forming control on the grid frequency

Thus, it is clear from the above that if compared with, for instance, a grid-forming BESS unit, the integration of grid-forming wind turbines with a conventional MPPT control and inertial support capability can have a negative effect on the dynamics of the grid frequency.

Depending on a TSO, WPPs connected to the transmission system are required to provide inertial support for several seconds [82]. The inertial support from grid-following wind turbines induces a second frequency dip due to the speed recovery phase in a wind turbine [83]. For certain disturbances, the second dip can be even larger than the first dip. To mitigate the second dip, control strategies extending the recovery phase have been proposed in [84]. Considering that grid-forming wind turbines will replace grid-following ones, they are likely to provide inertia support in order to comply with the grid code requirements. Therefore, to avoid the second dip of the grid frequency and compensate for the coupling between the grid-forming control and the MPPT, the latter has to be optimized or modified. Several solutions have been proposed in literature [85]–[87] by using an adaptive MPPT that extends the speed recovery period. In this thesis, another solution is implemented. As shown in Figure 2.5, it uses a LPF that slows down the power reference from the MPPT. The LPF time constant is 10 s.

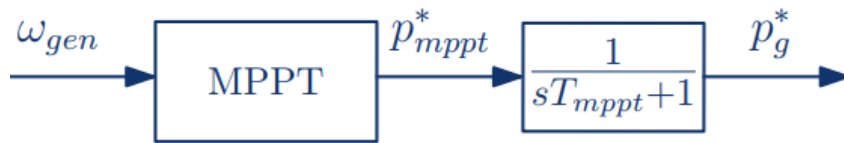


Figure 2.5. Position of the LPF for the MPPT power reference

The effectiveness of this solution is verified for the same case study of a 5-MW wind turbine and for the same grid disturbance of  $\text{RoCoF} = 1 \text{ Hz/s}$ . The inertia constant of the grid-forming control is set to 3.5 s. To compare the behavior of the grid-forming wind turbine without and with the LPF after the MPPT reference calculation, simulation results are presented in Figure 2.6. In Figure 2.6, (d) for the case with a LPF, the rotational speed of the wind turbine' generator experiences a more profound reduction. It is because by slowing down the MPPT power reference during the inertial response, more power is commanded to be supplied to the grid as shown in

Figure 2.6, (b). Then, more kinetic energy is extracted from the wind turbine. Thanks to this increased power supply, the grid frequency nadir is improved. Also, since the recovery period of the wind turbine rotational speed is extended, the secondary frequency dip is mitigated. Throughout the transient period, the DC bus voltage presented in Figure 2.6, (c), remains well controlled.

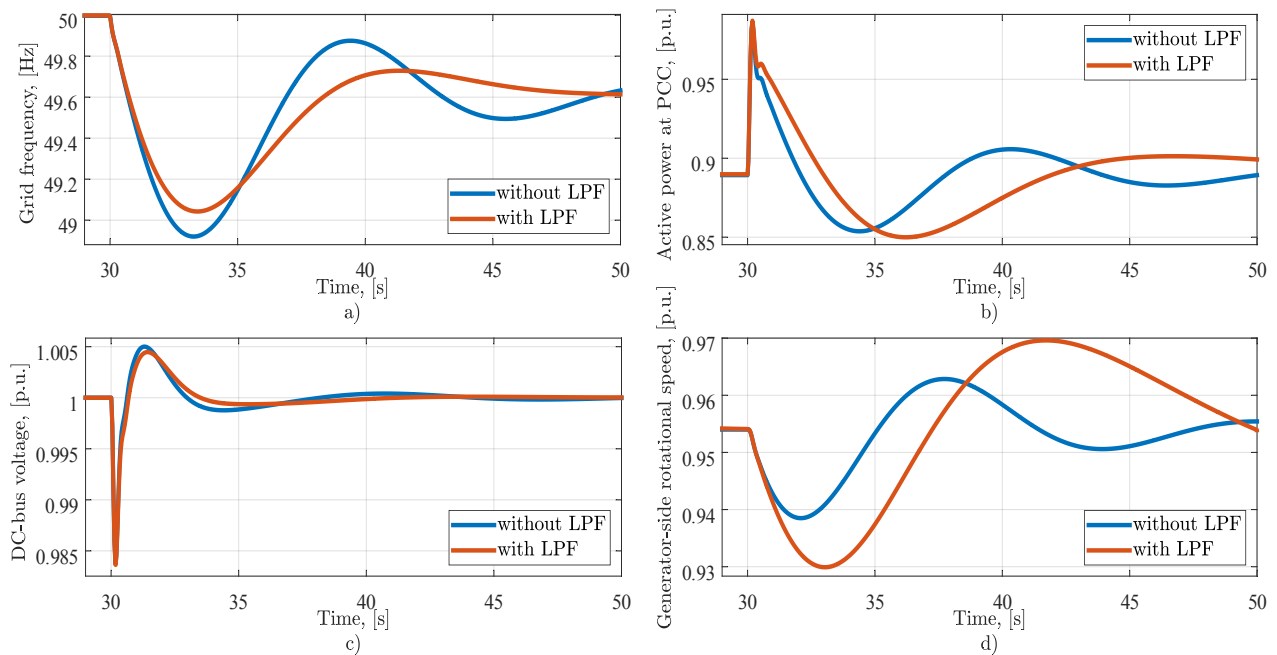


Figure 2.6. Effect of the MPPT' LPF on the wind turbine behaviour: a) grid frequency, b) active power at PCC, c) DC bus voltage, c) generator-side rotational speed

Analogously to the variation of the inertia constant of the grid-forming control in Figure 2.4, the same variation is performed for the case with the added LPF. The results are demonstrated in Figure 2.7.

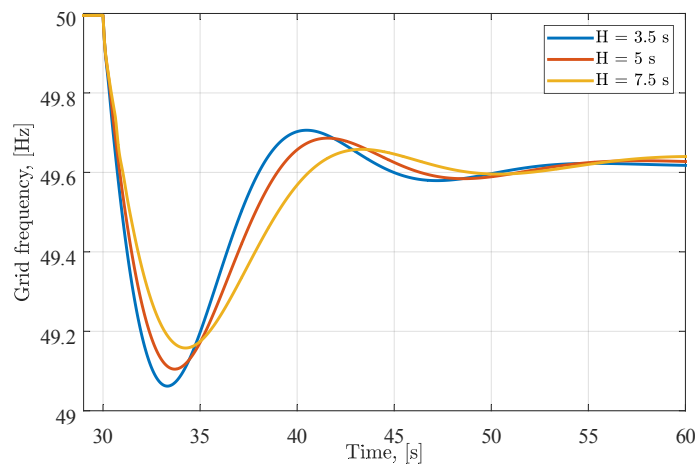


Figure 2.7. Impact of increased inertia constant in a grid-forming control on the grid frequency (the LPF is added to the MPPT reference)

Comparing these results with the ones in Figure 2.4, the effect of the increased inertia constant on the frequency nadir is more substantial while the secondary frequency dip is

sufficiently constrained. Hence, it is clear that by adding the LPF to the MPPT and thereby slowing down its power reference, it is possible to partially or completely decouple the dynamics of the wind turbine and the grid-forming control.

However, this solution with a LPF is only valid for the considered fast grid disturbance. In case of slower events such as wind speed variation and in the presence of a considered LPF, the variations of the rotational speed will be slower and will have a higher amplitude. So it will take more time for a wind turbine to get to a new operating point. The active power supplied to the PCC will have a similar behavior. Due to slowed down active power variations, the moment when the constant value of the available wind power is finally delivered to the grid will come much later. Therefore, to prolong the inertial response and to minimize the decrease of the efficiency in terms of the power supply during changes of the wind speed, a more sophisticated solution is required. One possible solution which is possibly capable of fulfilling both requirements is presented in [87], where the MPPT gains are dynamically adjusted in order to prolong the recovery phase of the wind turbine rotational speed.

## **2.2. Impact of the grid-forming control on mechanical structure of the wind turbine**

As mentioned in the introduction to this section, the grid-forming control has an indirect impact on the wind turbine' generator through the DC bus voltage controller by inducing fast variations of the electromagnetic torque. The consequences of the rapid variations of the electromagnetic torque have been addressed in [81], [88]. The extent of the torque variation depends on several factors. The first factor is the inertia constant of the grid-forming control, that defines the amount of active power to be supplied to the grid. It has a major effect on the DC bus voltage reduction during negative RoCoF events or phase jumps and, consequently, on the increased level of the electromagnetic torque. The second factor is the variation in electromagnetic torque depending on the DC bus voltage controller settings, that is, the settling time and the measurement delay in the feed-forward term of the grid current presented in the previous chapter.

In order to accurately identify the impact on the mechanical structure and demonstrate the effect of both factors, the drivetrain of the case study 5-MW grid-forming wind turbine is now considered as a two-mass mechanical model. Frictional losses in the turbine and the generator have been neglected. The parameters of the wind turbine model, the operating point and the grid disturbance are kept the same as in the previous section.

By analyzing the case study wind turbine's state-space representation, which is omitted in the manuscript, two complex conjugate oscillatory modes originating from the two-mass drivetrain model can be derived:

$$s_{1,2} = -0.88 \pm j15.65 \quad (2.4)$$

It is assumed that these modes represent the main oscillatory mechanical modes of the entire mechanical system of a wind turbine which includes generator, shaft, turbine rotor and turbine blades. These modes give an insight about the frequency at which the wind turbine's mechanical system is likely to oscillate whenever a rapid variation of the torque is applied. The value of the

frequency of oscillation can be found by dividing the imaginary part of the mode, also known as the damped angular frequency,  $\omega_d$ , by  $2\pi$ :

$$f_{osc} = \frac{\omega_d}{2\pi} = 2.5 \text{ Hz} \quad (2.5)$$

From Equation 2.5 it can be deduced that mechanical oscillations can be expected at a relatively low frequency of 2.5 Hz. This mechanical frequency strongly depends on the parameters of the drivetrain such as the shaft stiffness and damping. To confirm by simulations that this frequency indeed corresponds to the frequency of the wind turbine' drivetrain oscillations and to show the impact of the grid-forming control, the wind turbine model is simulated with the following inertia constants of the grid-forming control:  $H = 3.5 \text{ s}$ ,  $H = 5 \text{ s}$ ,  $H = 7.5 \text{ s}$ .

The results are presented in Figure 2.8. In line with the results from the previous section, a higher inertia constant allows delivering more active power during the inertial response as shown in Figure 2.8, (a). It results in a more notable reduction of the DC bus voltage depicted in Figure 2.8, (b). Consequently, as shown in Figure 2.8, (c), the DC bus voltage controller commands the electromagnetic torque to have a higher increase to extract more kinetic energy from the wind turbine and compensate for the power imbalance. In Figure 2.8, (d) – (e), the generator and turbine rotational speeds are shown. With a higher variation of the electromagnetic torque, the reduction of the rotational speed is more profound, as a result of the process of kinetic energy extraction. Most importantly, oscillations are observed in the rotational speed in Figure 2.8, (d) – (e). This means that the mechanical structure including the turbine, the drivetrain and the generator is vibrating. The cause of these torsional vibrations is the fast variation of the electromagnetic torque, resulting in the excitation of the drivetrain's oscillatory modes. With a higher inertia constant, the amplitude of these vibrations is increased. The frequency of these vibrations is around 2.5 Hz, and thus matches with the frequency derived from the state-space system representation. These torsional vibrations not only degrade the lifetime of the turbine' mechanical components. They also affect the dynamics on the DC bus and the AC side, since these vibrations propagate to the DC and AC side as low-frequency oscillations in the DC bus voltage and power, as shown in Figure 2.8, (a) – (b).

It can be concluded that the inertia constant of the grid-forming control indirectly influences the variation of the electromagnetic torque. Although the value of inertia constant does not define whether these torsional vibrations will appear, it has an influence on their amplitude.

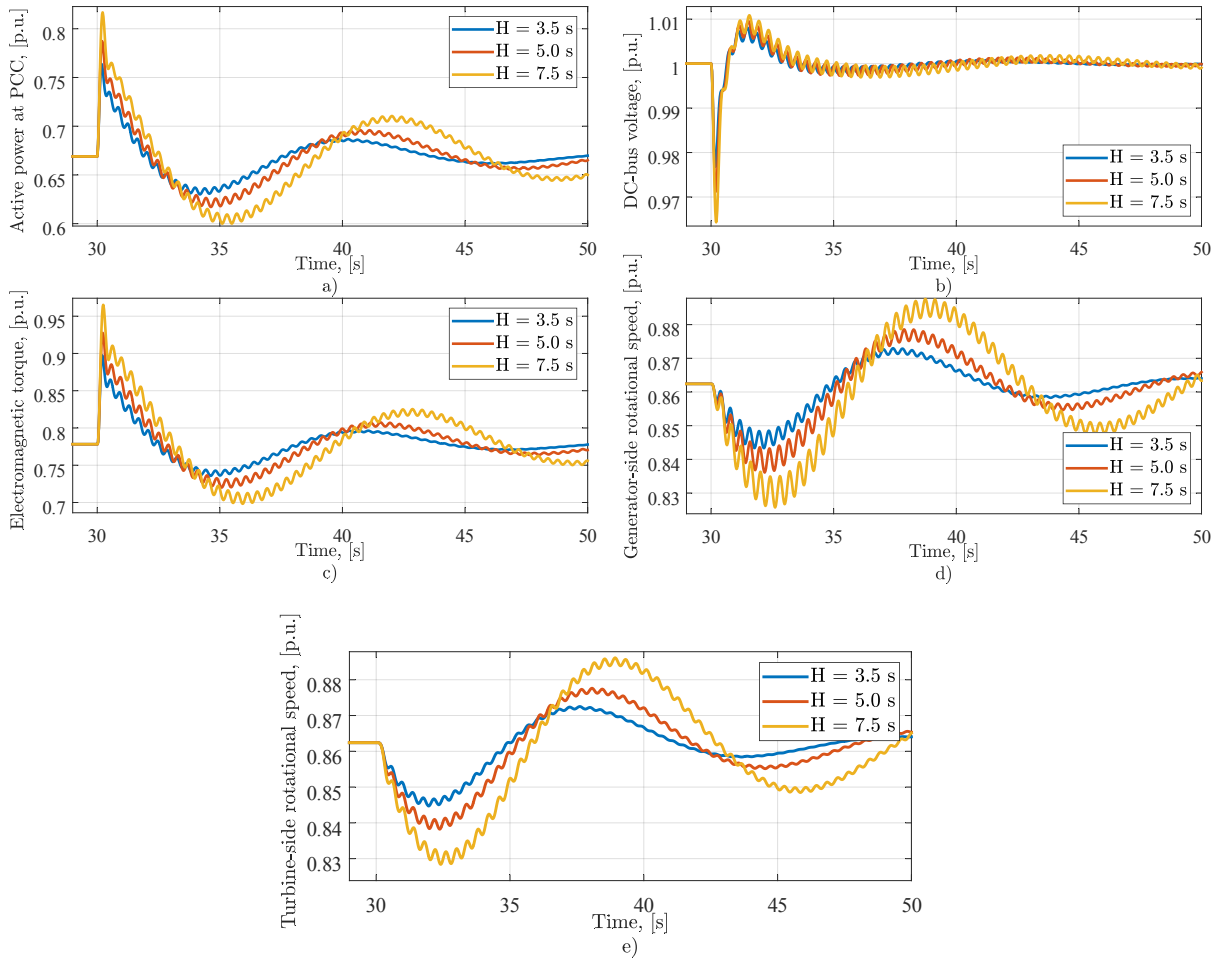


Figure 2.8. Wind turbine dynamics with different values of inertia constants: a) active power at PCC, b) DC bus voltage, c) electromagnetic torque, d) generator-side rotational speed, e) turbine-side rotational speed

Since the DC bus voltage controller plays the role of a coupling mechanism between the wind turbine and a grid-forming control, its dynamics can have a certain effect on the dynamics of the electromagnetic torque. To verify this, the wind turbine operation is analyzed with different settling times of the DC bus voltage controller. Also, the impact of the measurement delay in the feed-forward current compensation term is considered.

In Figure 2.9, the DC bus voltage controller' settling times are: 2 s, 1 s, 0.5 s. A faster DC bus voltage controller results in a faster stabilization of the DC bus voltage as shown in Figure 2.9, (b). Meanwhile, the effect on the electromagnetic torque shown in Figure 2.9, (c) and mechanical oscillations shown in Figure 2.9, (d) is negligible. Hence, it is possible to have a faster DC bus voltage controller without a significant adverse effect on the mechanical oscillations.

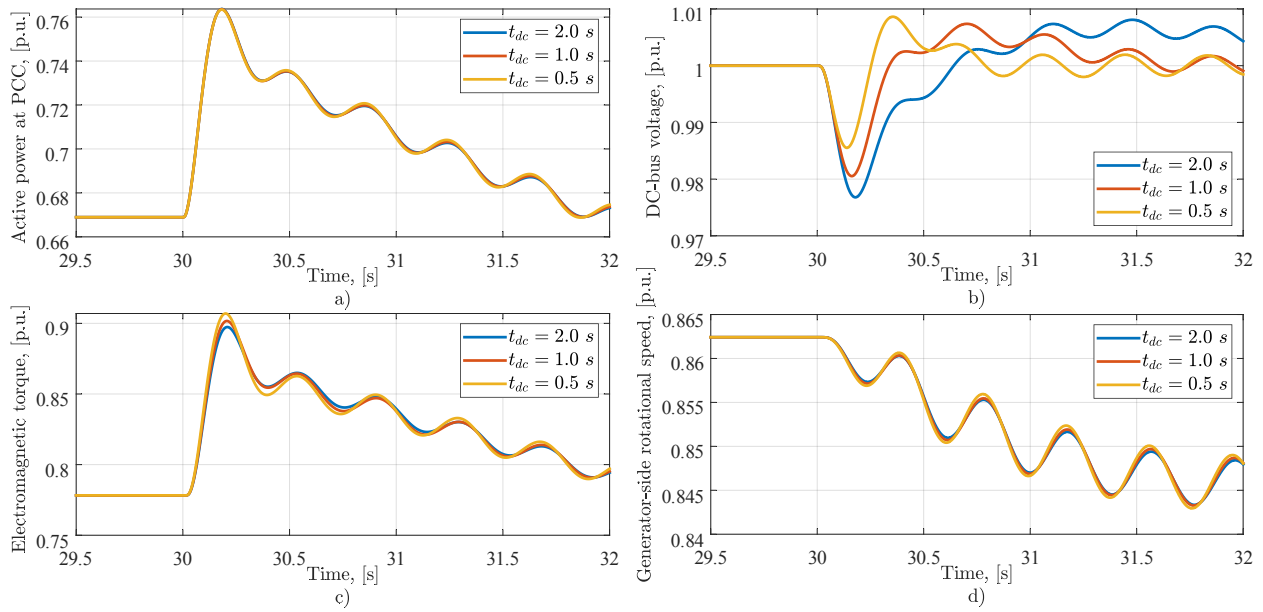


Figure 2.9. Analysis of the DC bus voltage controller's time response variation: a) active power at PCC, b) DC bus voltage, c) electromagnetic torque, d) generator-side rotational speed

In Figure 2.10, the effect of a variation of the measurement delay,  $T_{dc}$ , for the feed-forward current compensation term is presented. The measurement delays are 5, 15 and 25 ms. As can be seen in Figure 2.10, (b), a delay in the measurement can affect the stability of the system. It is clear that a slower feed-forward term can serve as a destabilizing factor since it induces more substantial variations in DC bus voltage. Hence, the electromagnetic torque variations, as well as the oscillations in rotational speed, become more significant, Figure 2.10, (c) – (d). The increased intensity of these vibrations also gives rise to increased oscillations on DC and AC sides in Figure 2.10, (a) – (b).

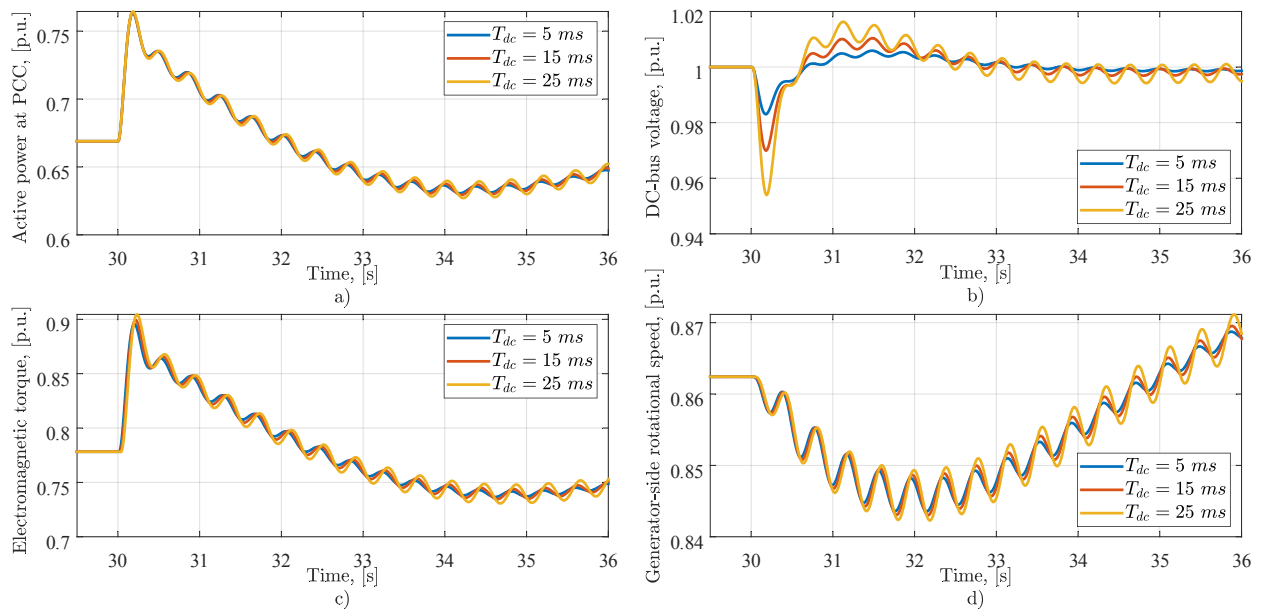


Figure 2.10. Results on variation of the measurement delay: a) active power at PCC, b) DC bus voltage, c) electromagnetic torque, d) generator-side rotational speed

The results in Figure 2.9 – Figure 2.10 can be summarized in the following conclusions:

- The inertia constant of the grid-forming control influences the amplitude of the electromagnetic torque variation and can increase the amplitude of torsional vibrations;
- A faster DC bus voltage controller can improve the DC bus voltage controllability with minor changes in the behavior of the electromagnetic torque and torsional vibrations;
- The current feed-forward term is required to keep DC bus voltage stable. Measurement delays reduce controllability of the DC bus voltage and can give rise to an unstable operation. However, since the B2B converter and the DC bus voltage controller both are located in the nacelle, the measurement delay should remain sufficiently small. So, stable operation can be ensured.

### 2.3. Mitigation of torsional vibrations in a grid-forming wind turbine

Based on the results in the previous section, it was confirmed that fast variations of the electromagnetic torque lead to an excitation of torsional vibrations. To ensure safe, stable and optimal operation of the wind turbine, it is important to attempt suppressing these vibrations. In the past, several damping methods have been proposed for a traditional grid-following wind turbine [89]–[98]. The majority of these methods rely on a modification of the control reference to counteract electromagnetic torque oscillations or to convert torsional vibrations into oscillations of the DC bus voltage. It has been found that analogous damping methods can be applied to a grid-forming wind turbine [99]–[102]. However, since the DC bus voltage is controlled by the MSC, a trade-off exists between the accuracy of the DC bus voltage control and the effectiveness of the vibration damping. In other words, the modification of the control reference component is likely to interfere in the control of the DC bus voltage, and the efficiency of vibrations damping can be reduced. In this section, four different damping methods are presented. The newly proposed damping approach based on the input shaping (IS) method is highlighted and deeply studied.

#### 2.3.1. Methods for vibration damping in a grid-forming wind turbine

- Damping with a high-pass filter [100]

This method is presented in order to demonstrate that it is feasible to suppress the torsional vibrations by damping the electromagnetic torque reference with a filtered component of generator rotational speed. For the filtering, a HPF is used. The block diagram of damping implementation is shown in Figure 2.11.

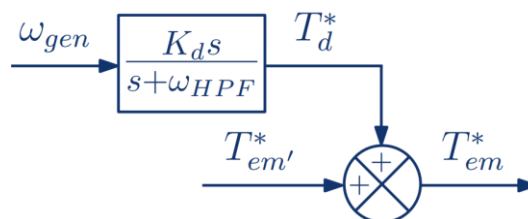


Figure 2.11. Block diagram of the electromagnetic torque reference modification with a damping torque derived with a HPF

where  $K_d$  is a damping gain,  $\omega_{HPF}$  is the high-pass frequency,  $T_d^*$  is the damping torque reference,  $T_{em}^*$  is the electromagnetic torque reference before adding the damping torque.

- Damping with a band-pass filter (BPF) [99]

To study the possibility of vibrations damping in a grid-forming wind turbine, a more detailed investigation has been carried out in [99] where a BPF was applied to the signal of the generator's rotational speed as shown in Figure 2.12 to generate the damping torque reference. The BPF in Laplace domain is expressed as:

$$T_d^* = T_{em}^* K_d \frac{2\xi\omega_n s}{s^2 + 2\xi\omega_n s + \omega_n^2} \quad (2.6)$$

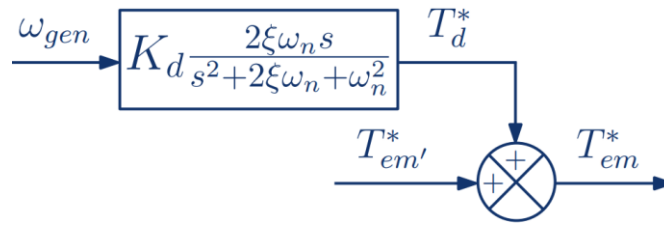


Figure 2.12. Block diagram of the electromagnetic torque reference modification with a damping torque derived with a BPF

The authors in [99] have performed an in-depth frequency-domain and small-signal analysis to comprehensively describe the filter parameters tuning for achieving better damping performance.

- Combined damping method [101]

This method implies the modification of the electromagnetic torque reference by changing the DC bus voltage reference. As shown in Figure 2.13, a scheme reproduced from [24], the reference modification is performed by means of a combination of a BPF and the power output generated from a droop-based frequency regulation component of the VSM,  $\Delta p_f$ . In other words,  $\Delta p_f$  is the power required for the frequency regulation.

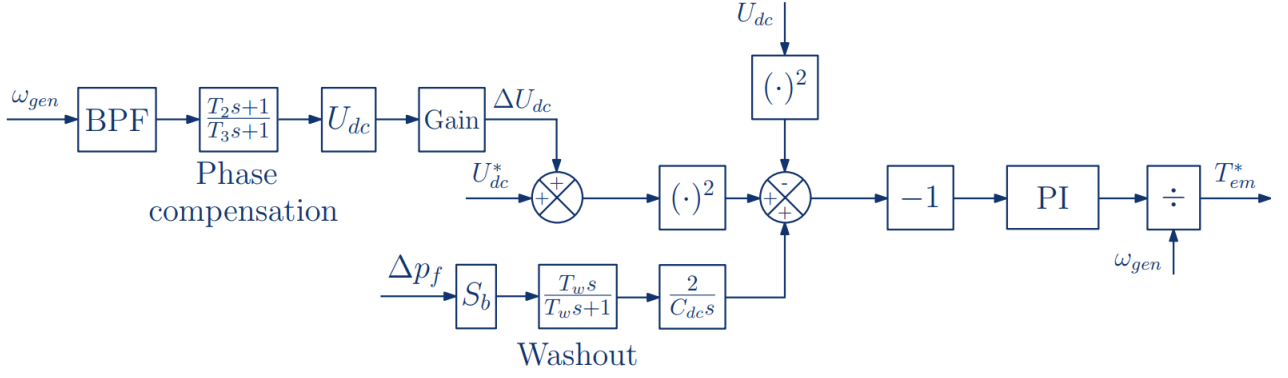


Figure 2.13. Block diagram for a combined damping method

In Figure 2.13, the phase compensation after a BPF is used in order to align the electromagnetic torque in phase with the oscillations of the generator rotational speed. The power  $\Delta p_f$  is filtered. Then, by integrating it, the energy is derived. This energy corresponds to the energy required for frequency regulation and is added in order to keep the power balance in the drivetrain and to mitigate the impact on drivetrain dynamics.

- Damping based on the IS method [102]

The application of this method to a grid-forming wind turbine is the original proposition of this thesis. The principle of the IS method is to modify a controlled reference signal by a convolution with a sequence of impulses to get a system response without oscillations. The IS was initially proposed in the form of Posicast control, mentioned in [103]. Usually, IS is used to damp mechanical vibrations in flexible mechanical systems such as industrial robotic hands or tower cranes. Since a drivetrain of a wind turbine is also a flexible mechanical system, the method can be utilized for the purpose of torsional vibrations damping. The IS can be implemented with a finite pulse response filter. One type of such a filter is known as a zero-vibration (ZV) filter [104]. A 2-pulse ZV filter is expressed by the transfer function:

$$IS(s) = A_1 e^{-t_1(\sigma + j\omega_d)} + A_2 e^{-t_2(\sigma + j\omega_d)} \quad (2.7)$$

where  $A_1, A_2$  are the amplitudes of 1<sup>st</sup> and 2<sup>nd</sup> pulse respectively,  $t_1, t_2$  are the time instants for the corresponding pulses,  $\sigma = \xi\omega_n$  is the real part of a drivetrain oscillatory modes, and  $\xi, \omega_n, \omega_d$  are the damping coefficient, natural frequency and damped natural frequency of the drivetrain oscillatory modes.

The requirements, a ZV filter has to comply with, are the following:

$$0 \leq t_1 < t_2 \quad (2.8)$$

$$A_1 + A_2 = 1 \quad (2.9)$$

### Setting of a ZV filter

To correctly adjust a ZV filter with a good performance, it is necessary to know the information about the drivetrain oscillatory modes. With this information, a ZV filter settings can be calculated by following a step-by-step approach presented in [105]:

1) Define the time for each pulse:

$$t_1 = 0, t_2 = t_1 + T_d \quad (2.10)$$

where

$T_d = \frac{\pi}{\omega_d}$  – damped period of the drivetrain oscillatory mode.

2) Define the pulses amplitude:

$$A_1 = \frac{e^{\frac{\xi\pi}{\sqrt{1-\xi^2}}}}{1 + e^{\frac{\xi\pi}{\sqrt{1-\xi^2}}}}, A_2 = 1 - A_1 \quad (2.11)$$

where the damping ratio can be defined as  $\xi = \left| \frac{\sigma}{\sqrt{\sigma^2 + \omega_d^2}} \right|$ .

A ZV filter can be included to the reference of the electromagnetic torque in the open-loop as shown in Figure 2.14.

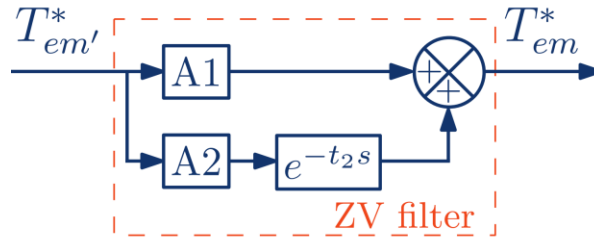


Figure 2.14. 2-pulse ZV filter shaping the reference of the electromagnetic torque

As seen from Figure 2.14, the electromagnetic torque reference signal is separated into two parts. The first part corresponds to  $T_{em}^* A_1$ . The second part is delayed and corresponds to  $T_{em}^* A_2 e^{-t_2 s}$ .

The application of the above listed damping methods allows reducing the amplitude of torsional vibrations to a different extent. In each method the DC bus serves as a buffer for the mechanical oscillations. That is why, there is a negative effect expected in the form of increased oscillations of the DC bus voltage. Depending on the damping method, these oscillations may go beyond the operational limits of the DC bus voltage.

### 2.3.2. Comparison of damping methods efficiency

The objective of this section is to demonstrate the efficiency of vibration damping using the proposed IS method implemented with a ZV filter. The results of application of the ZV filter are compared with the damping method using a HPF. The simulations for comparison are based on the wind turbine model with a two-mass drivetrain presented in Figure 2.15. The position of the damping block is highlighted. The parameters of the model and grid disturbance are the same as in Section 1.3. The parameters of the HPF and a ZV filter are provided in Table 2.1.

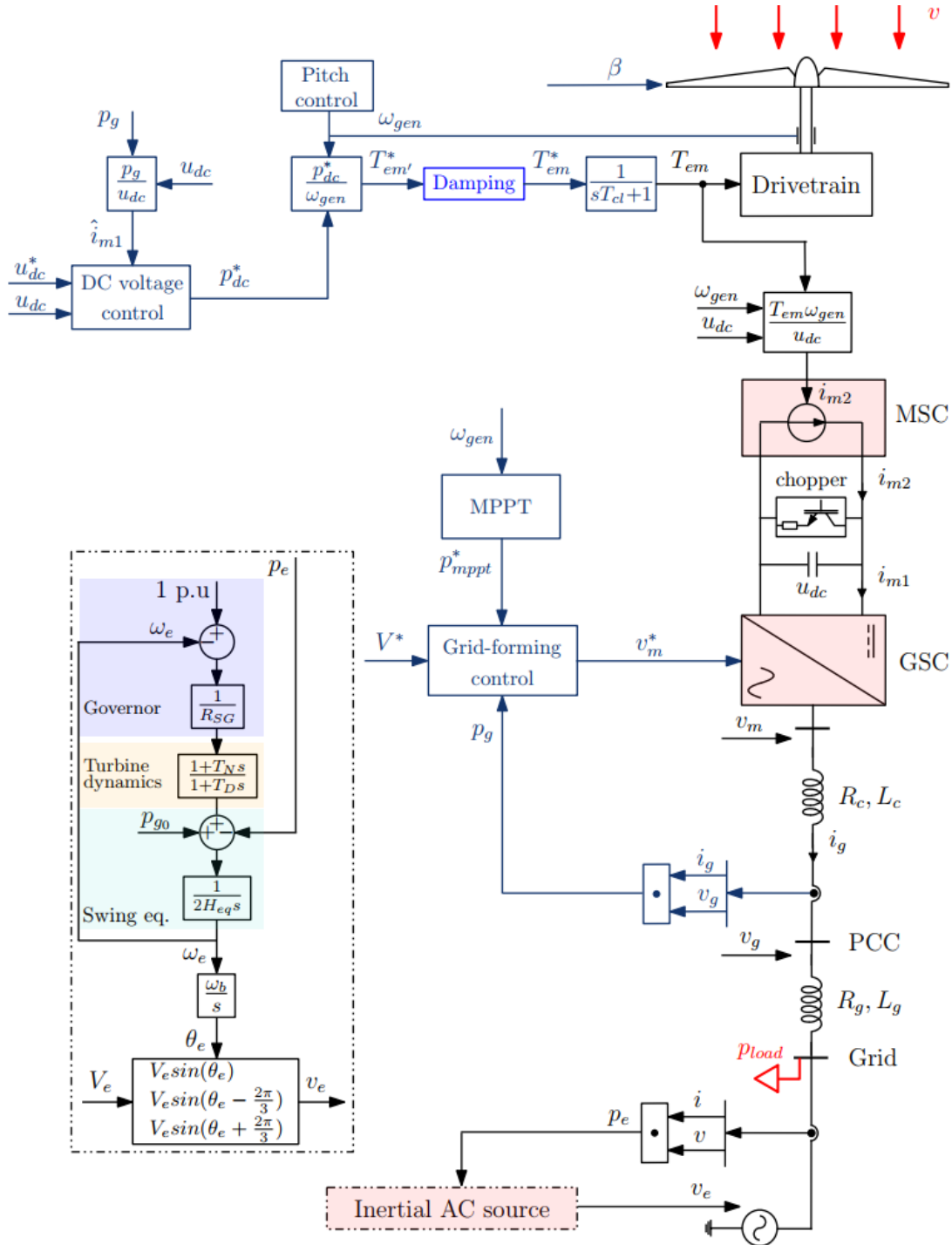


Figure 2.15. Model of a grid-forming wind turbine with the indicated damping block

Table 2.1. Parameters of damping filters

Parameter	Value
<b>HPF:</b>	
Cut-off frequency, $\omega_{HPF}$	1 rad/s
Damping gain, $K_d$	5
<b>ZV filter:</b>	
Impulse amplitude, $A_1, A_2$	0.54, 0.46
Pulse time, $t_1, t_2$	0.0 s, 0.2 s

In Figure 2.16 the comparison of the two damping methods considered is provided. A ZV filter is perfectly tuned for the identified oscillatory modes. As seen from Figure 2.16, (c), the electromagnetic torque can be damped in both cases. In Figure 2.16, (d) – (e), it is shown that the damped torque results in suppressed torsional vibrations on the generator and turbine sides. However, the quality of damping differs. The vibrations at the beginning of the disturbance are better damped with a ZV filter. As depicted in Figure 2.16, (b), the DC bus dynamics are slower with a HPF. The DC bus voltage faster stabilizes with the application of a ZV filter. Considering the active power output at the PCC, if mechanical vibrations are damped, they do not propagate to the AC side as electrical oscillations.

It has been found that with the use of a conventional damping method (HPF in this context) it is possible to damp torsional vibrations. There is no doubt that damping efficiency can be improved with the use of an optimally tuned BPF as it is confirmed in [99], [101]. The damping based on the IS method does not require additional phase compensation units to perform the damping function. From the obtained results it is found that compared to the HPF-based method, the use of the damping based on the IS method provides improved effect in terms of torsional vibrations damping and allows faster stabilization of the DC bus voltage.

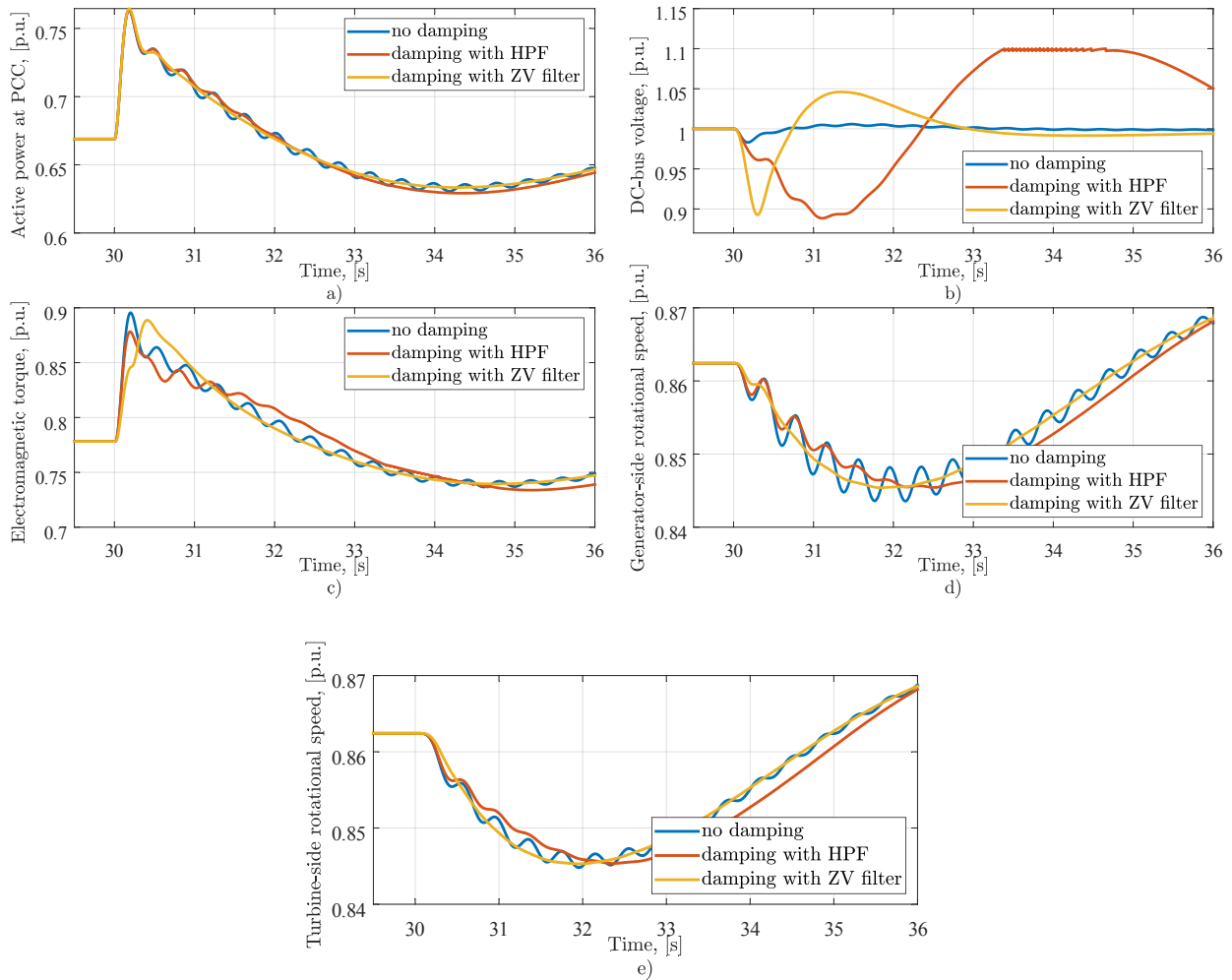


Figure 2.16. Comparison of damping with a HPF and a ZV filter: a) active power at PCC, b) DC bus voltage, c) electromagnetic torque, d) generator-side rotational speed, e) turbine-side rotational speed

## 2.4. Analysis of the damping based on the input shaping method

After having confirmed the positive effect the IS-based damping method has on the reduction of torsional vibrations, the robustness of this method is to be verified. Thus, in this section, the efficiency of the ZV filter is analyzed. Firstly, the impact of the DC bus voltage controller dynamics on the vibration damping is studied. Secondly, since damping is shown to have a negative impact on the DC bus voltage, several solutions are proposed to mitigate this impact. Finally, the robustness of a ZV filter is also tested against parametric variations.

### 2.4.1. Impact of the DC bus voltage controller on damping efficiency

The main function of the MSC is to control the DC bus voltage. Adding a complementary responsibility such as vibration damping can potentially create interactions between the DC bus voltage controller and the ZV filter. This holds especially when the DC bus voltage controller is fast and its settling time is close to the time constant of the ZV filter. To present this issue, the

operation of the DC bus voltage controller is tested with the following settling times,  $t_{dc} = 2$  s,  $t_{dc} = 1$  s and  $t_{dc} = 0.5$  s. The system model presented in Figure 2.15 is simulated for a grid frequency variation with a RoCoF = 2 Hz/s.

The results are provided in Figure 2.17. Accelerated dynamics of the DC bus voltage controller result in faster variations of the electromagnetic torque as shown in Figure 2.17, (c). Fast torque variations do not induce torsional vibrations at 2.5 Hz because the ZV filter performs well its damping function. As was noted, the MSC at the same time is responsible for controlling the DC bus voltage and vibration damping. If the time constants of the DC bus controller and a ZV filter are close to each other, it can become infeasible to perform both functions simultaneously. As exemplified in Figure 2.17, (b) – (c), there are low-frequency variations at around 1.4 Hz for a settling time of 0.5 s. These are the consequence of the interaction between the DC bus voltage controller and a ZV filter. In Figure 2.17, (d) – (e), the drivetrain vibrations at 2.5 Hz are damped. However, the vibrations at 1.4 Hz are not damped and the faster the DC bus voltage controller, the bigger the vibrations' amplitude. Based on the presented results, it is inevitable that the DC bus voltage controller has to be relatively slow to be able to perform both assigned functions. In this case, the feed-forward action in the DC bus voltage controller is compulsory.

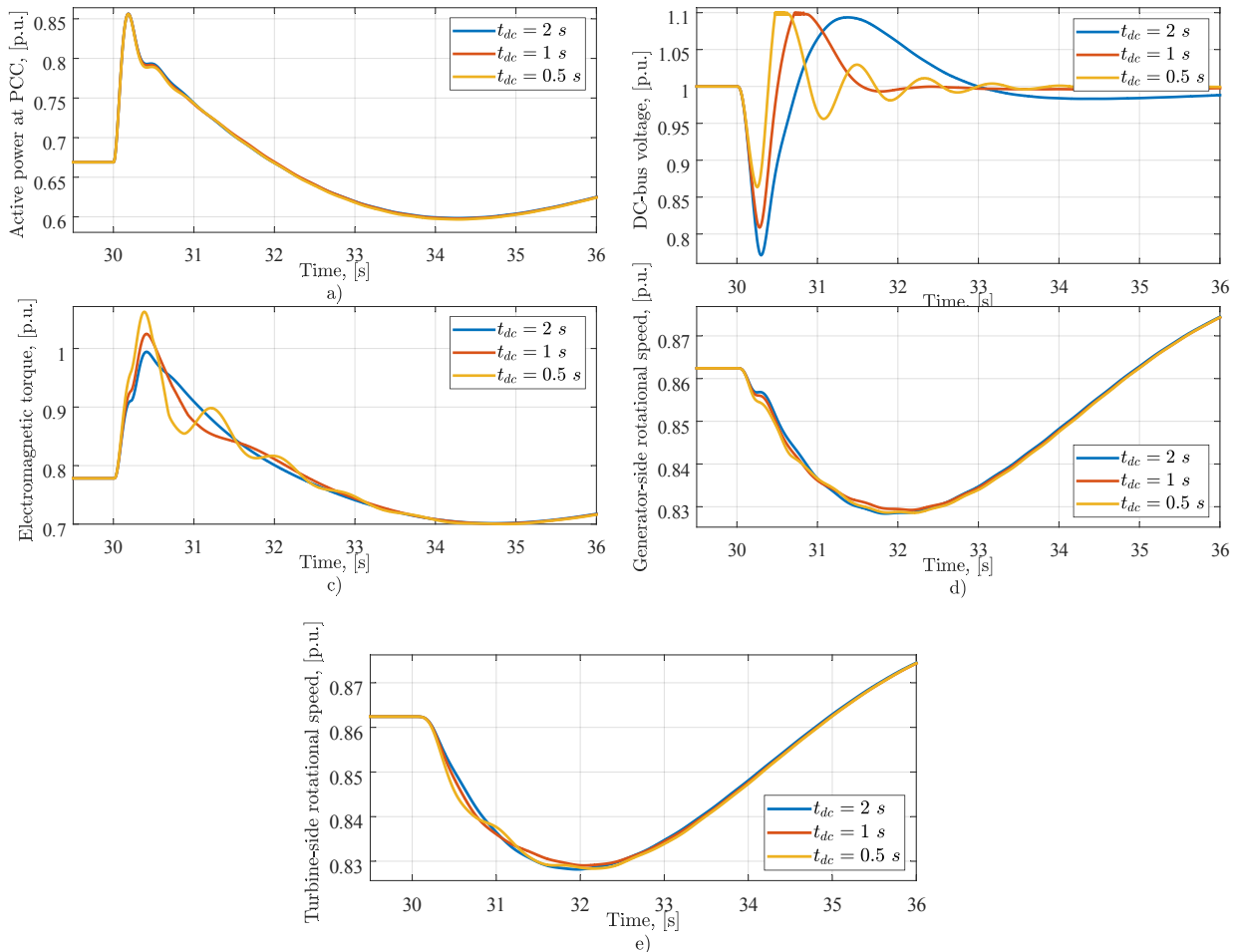


Figure 2.17. Variation of the DC bus voltage controller' settling time: a) active power at PCC, b) DC bus voltage, c) electromagnetic torque, d) generator-side rotational speed, e) turbine-side rotational speed

### 2.4.2. Minimization of the negative effect of the vibration damping

As demonstrated in previous sections, the application of a ZV filter allows suppressing the torsional vibrations on the mechanical side. However, the impact on the DC bus voltage is inevitable because the modifications to the electromagnetic torque directly influence the power balance and, hence, the DC bus voltage. This involves an increased amplitude of DC bus voltage variations, which can be significantly large and, depending on the grid disturbance, can even violate the operational voltage limits, typically in the range of 0.9 - 1.1 pu. To mitigate this effect, two solutions are proposed.

- Sharing of the damping effect between the MSC and the GSC.

This solution implies that the damping effect is shared between both converters. It is implemented by modifying the power reference of the grid-forming control with an incorporation of a term  $\Delta p = k(p_{damp}^* - p_{dc}^*)$  as depicted in Figure 2.18.

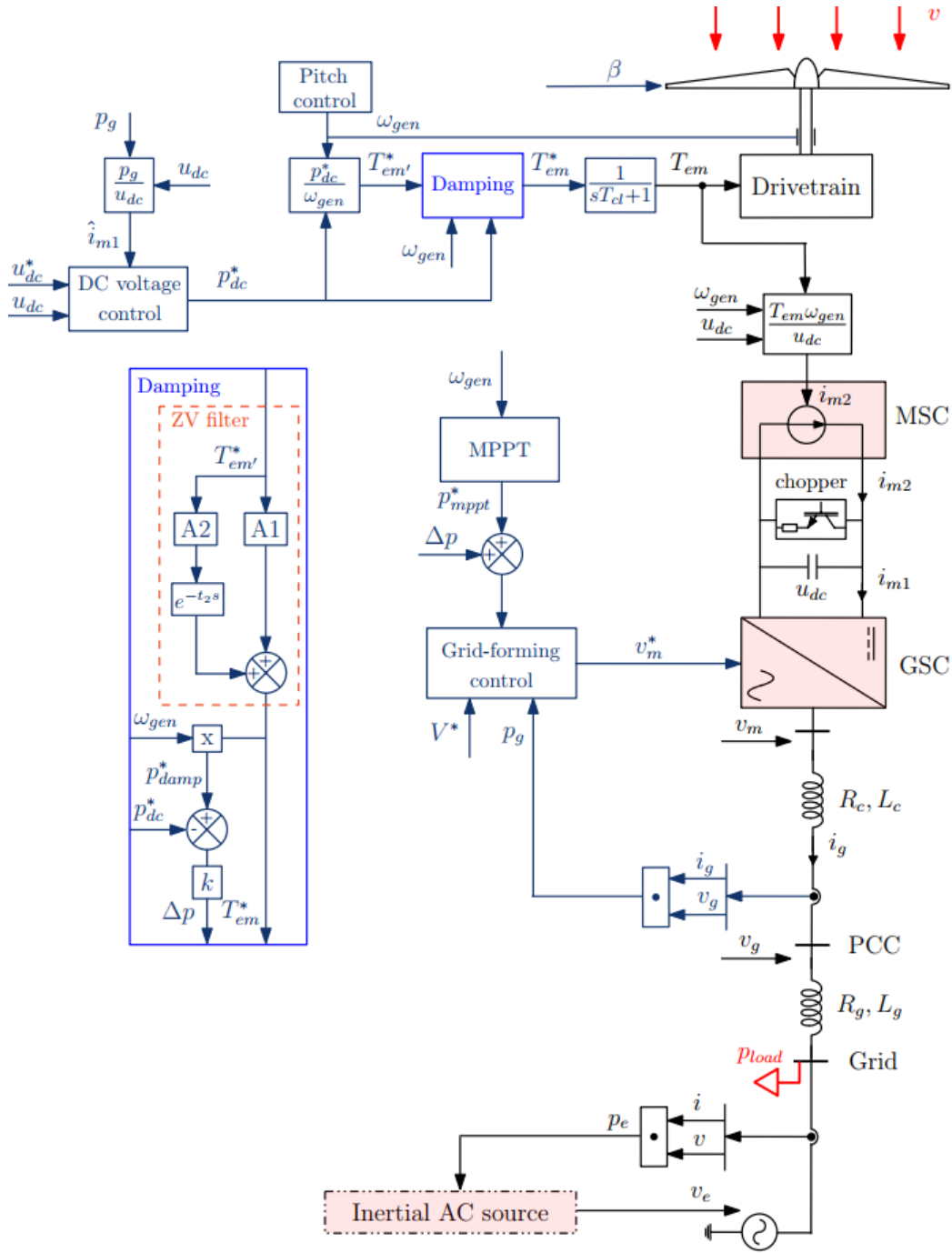


Figure 2.18. System model, damping + sharing of damping effect

The simulation results obtained for the same RoCoF, with the settling time of the DC bus voltage controller set to  $t_{dc} = 1$  s, are showcased in Figure 2.19 where  $k = 1, 2, 3$ . From Figure 2.19, (b) the DC bus voltage management is improved. When increasing the gain  $k$ , the maximum voltage deviation decreases. However, this has an impact on the inertial response of the grid-forming GSC. It alleviates the initial peak of the power injected to the grid as shown in Figure 2.19, (a). As demonstrated in Figure 2.19, (f), this alleviation happens due to the  $\Delta p$  signal that reduces the active power reference of the grid-forming control so that less active power is required to be transmitted to the grid side during a disturbance. As depicted in Figure 2.19, (f), the  $\Delta p$  term also contains oscillations that are re-introduced to the grid side. Then, the DC bus voltage control

modifies  $p_{dc}^*$  to keep the power balance, so that there are also a few low-frequency oscillations re-introduced to the DC bus and to the mechanical side, as shown in Figure 2.19, (b) – (e). Thus, it can be confirmed that the proposed solution can help to mitigate the variations of the DC bus voltage. Nevertheless, this solution has to be limited in order to avoid re-introducing oscillations as much as possible. The value of  $k = 1$  can be selected as a default.

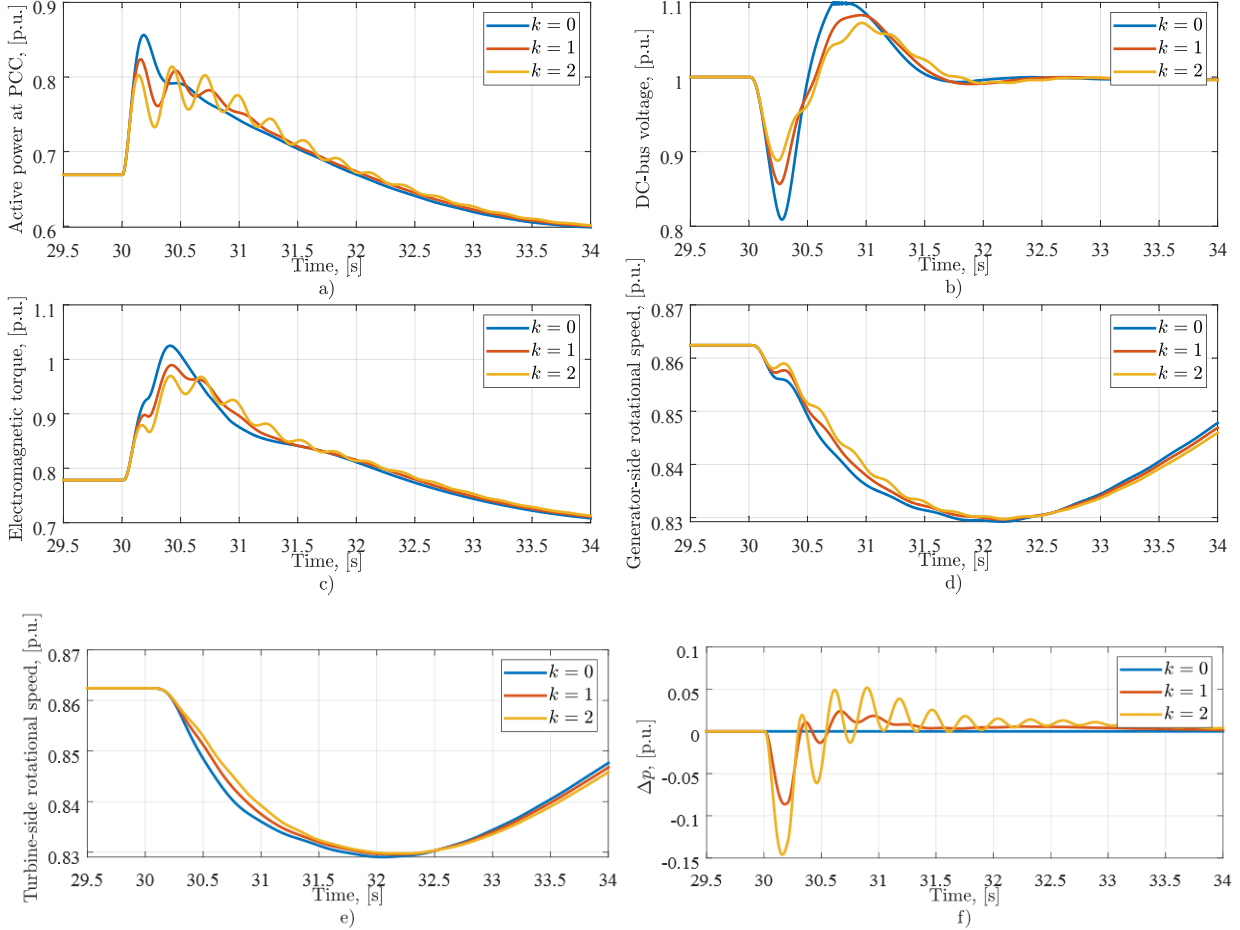


Figure 2.19. Variation of gain  $k$  in the term  $\Delta p$  for sharing the damping effect: a) active power at PCC, b) DC bus voltage, c) electromagnetic torque, d) generator-side rotational speed, e) turbine-side rotational speed, f)  $\Delta p$  power

- De-activation of a ZV filter based on a DC bus voltage criterion

As shown in previous results, the DC bus voltage risks going below the minimum voltage limit of 0.9 pu. In a practical application, the converter would not accept this voltage variation and would probably trip. To avoid this phenomenon, the damping method should preferably be de-activated based on a DC bus voltage criterion.

The system model is the same as in Figure 2.18. The damping block is complemented with additional logic for damping de-activation, as shown in Figure 2.20.

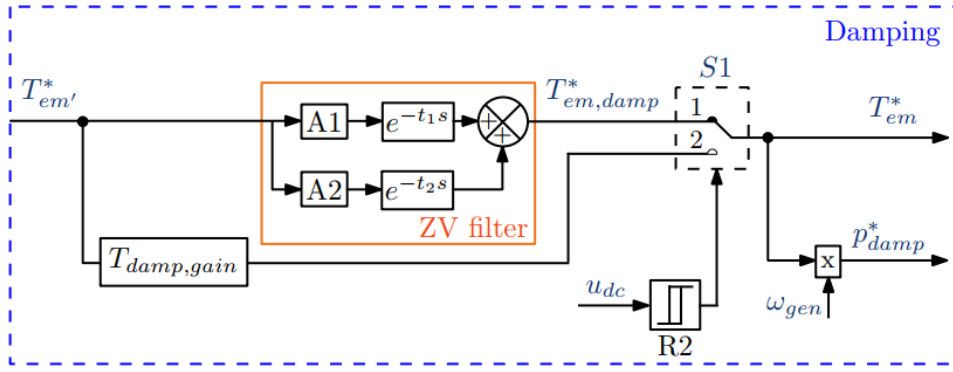


Figure 2.20. Description of the damping block with de-activation based on the DC bus voltage criterion

The de-activation based on the DC bus voltage criterion is implemented with an hysteresis relay block, R2. It switches the electromagnetic torque reference to the one that has not been processed with the ZV filter. Since the ZV filter is in this way de-activated, it is possible to introduce the gain  $T_{damp,gain}$ , which can be set  $\geq 1$  to speed up the restoration of the DC bus voltage. R2 has the following logic:

- If  $u_{dc} < 0.9 \text{ pu} \rightarrow T_{em}^* = T_{em}'^*$
- If  $u_{dc} \geq 0.91 \text{ pu} \rightarrow T_{em}^* = T_{em,damp}^*$

The criterion on the DC bus voltage allows avoiding severe voltage drops at the DC bus [102]. To demonstrate this, the system model shown in Figure 2.18 is simulated with a damping block from Figure 2.20. The  $T_{damp,gain} = 1$ . The grid disturbance is a RoCoF = 2 Hz/s. To see how damping efficiency is influenced with its de-activation, the simulations include three cases:

1. no damping;
2. damping + sharing of damping effect ( $k = 1$ );
3. damping + sharing of damping effect ( $k = 1$ ) + de-activation.

The simulation results are presented in Figure 2.21. Figure 2.21, (b), demonstrates that for the third case the damping de-activation allows keeping the DC bus voltage around the lower limit. In exchange to this improvement, the dynamics of the electromagnetic torque are changed. In Figure 2.21, (c), it can be seen that there is a fast spike 200 ms after the start of a disturbance. This is because when the DC bus voltage moves below its lower limit the first time, the torque reference switches from the reference processed by the ZV filter to the unshaped reference directly obtained from the DC bus voltage controller. Once the DC bus voltage returns above 0.91 pu, the torque reference switches back. This switching results in a reduced efficiency of the intended vibration damping, as presented in Figure 2.21, (d) – (e). However, the amplitude of mechanical vibrations is still significantly smaller compared to the case without damping. The same applies to the drivetrain vibration-induced oscillations of the active power, DC bus voltage and the electromagnetic torque in Figure 2.21, (a) – (c).

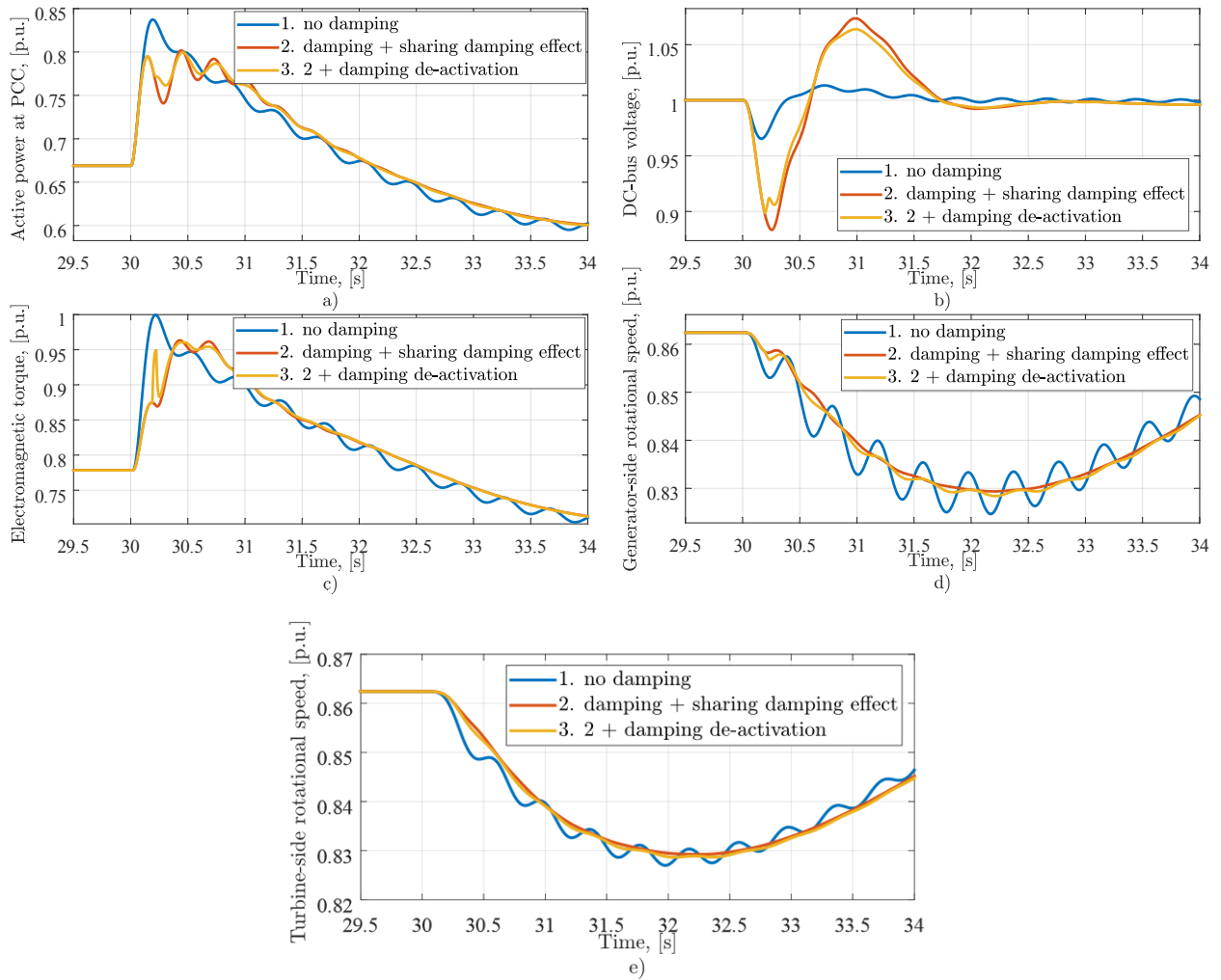


Figure 2.21. Damping de-activation for a RoCoF event: a) active power at PCC, b) DC bus voltage, c) electromagnetic torque, d) generator-side rotational speed, e) turbine-side rotational speed

- De-activation of the ZV filter based on a DC and AC voltage criterion

Since the grid-forming wind turbine is linked to the grid, it can undergo severe stresses during grid faults. These involve significant changes of the electromagnetic torque inducing torsional vibrations. It can result in profound variations of the DC bus voltage during the post-disturbance period. Moreover, if damping is activated throughout the disturbance, the reductions of the DC bus voltage can be more severe. Therefore, to constrain the DC bus voltage from significant reductions and to prevent fast variations of the electromagnetic torque during grid faults, a criterion based on the voltage at the PCC has to be added, as shown in Figure 2.22.

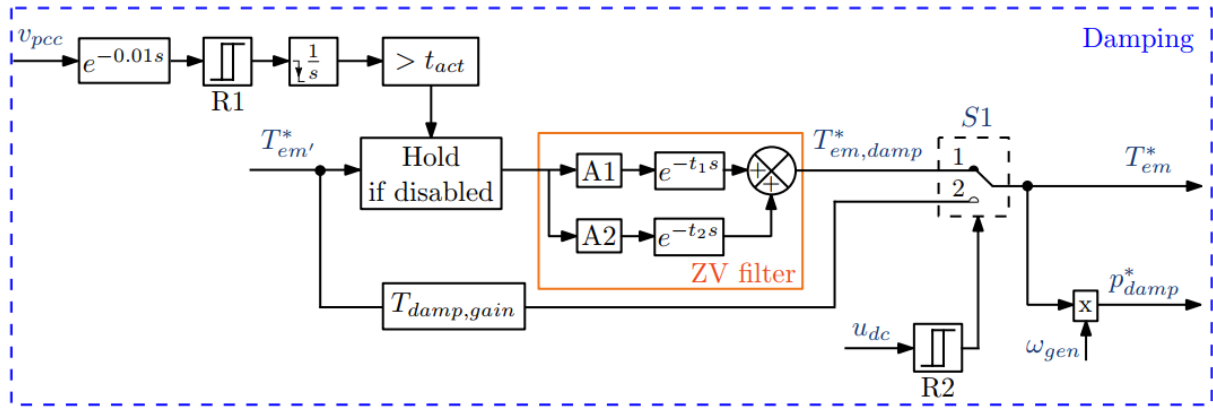


Figure 2.22. Description of the damping block with de-activation based on DC and AC voltage criteria

It is implemented with an hysteresis relay, R1. R1 aims at fixing or slowing down variations of the torque reference if the AC voltage  $v_{pcc} < 0.8 pu$ . Once  $v_{pcc}$  returns above  $0.9 pu$ , the torque reference is fixed for a period of  $t_{act} = 500 ms$  to avoid additional torque variations caused by the ZV filter and to ensure that the damping is not re-activated before stabilizing the PCC voltage. A 10-ms voltage measurement delay is also added.

To demonstrate how damping de-activation can be beneficial during a severe fault, a 100-ms three-phase short circuit is added to the PCC. The grid frequency is constant. The simulation results are presented in Figure 2.23. During the fault, the active power at the PCC in Figure 2.23, (a), almost reduces to 0 pu. The DC bus voltage in Figure 2.23, (b), starts rising and the DC bus voltage controller tries to rapidly reduce the electromagnetic torque as presented in Figure 2.23, (c). Subsequently, with the fast torque reduction, the drivetrain shaft starts vibrating. For the case without damping, these torsional vibrations have an increasing amplitude as shown in Figure 2.23, (d) – (e). So, at the end, the system can become unstable. When the damping is activated, a ZV filter splits the reduction of the torque into two parts. The initial part is now less severe than in the case without damping. However, there is a second reduction happening 0.2 s after a fault. This value corresponds to the time delay of a ZV filter. The second dip leads to a power imbalance resulting in a profound reduction of the DC bus voltage. A very low voltage level can lead to issues such as a saturation of the modulation index, which can affect the output from the GSC.

It is demonstrated in Figure 2.23, (b) – (c) that substantial variations of the torque and the DC bus voltage can be avoided by de-activating damping during and after a short-circuit or during the DC bus voltage reductions below the limit. The DC bus voltage reduction in Figure 2.23, (b) is much more mitigated compared to the case where damping is activated over the entire simulation period. Meanwhile, the overvoltages are well prevented with the DC chopper. As depicted in Figure 2.23, (c), this solution holds the electromagnetic torque nearly constant during the short-circuit and a certain time period,  $t_{act} = 500 ms$ , after it. Thus, adverse excitation of the drivetrain modes is avoided and there are minor mechanical variations on the generator and turbine sides, Figure 2.23, (d) – (e). Hence, for severe events, such as short-circuits, the proposed damping method successfully copes with its main objective. It should also be highlighted that the damping re-activation time after a short-circuit should be higher than the delay imposed by the ZV filter in order to limit the variation in amplitude of the electromagnetic torque induced by the delay of the ZV filter.

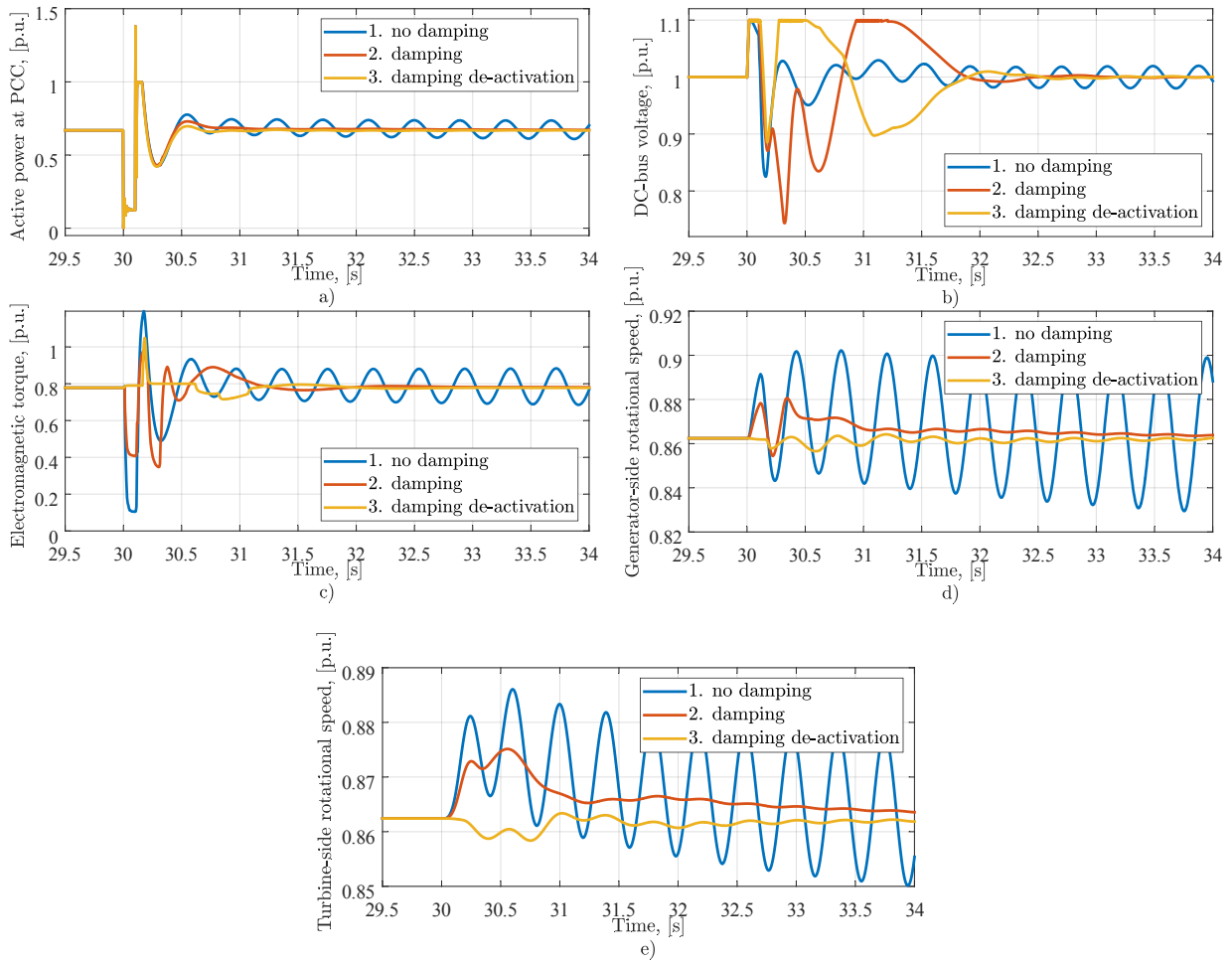


Figure 2.23. Damping de-activation for a 100-ms three-phase fault: a) active power at PCC, b) DC bus voltage, c) electromagnetic torque, d) generator-side rotational speed, e) turbine-side rotational speed

### 2.4.3. Robustness against parametric variations

The parametric variation scenarios considered are:

- Variation of the drivetrain shaft stiffness due to changing surrounding conditions. It implies that the natural frequency of drivetrain oscillatory modes varies within a certain range.
- Inaccurate estimation of the drivetrain oscillatory modes. The information about the oscillatory modes used for the design of a ZV filter can be determined with an error.

Firstly, to demonstrate the resilience of the ZV filter, the shaft stiffness is changed in order to modify the frequency of the drivetrain oscillatory modes by 20%. This value assumes taking into account the maximum possible variation of the shaft stiffness. For the variation of the frequency in the range of  $f_{osc} = [2 \leftarrow 2.5 \rightarrow 3]$  Hz, the shaft stiffness is changed in the range of  $K_s^{pu} = [182 \leftarrow 280 \rightarrow 408]$  pu. Knowing that the ZV filter is designed for the natural frequency of 2.5 Hz and its settings are fixed, the damping efficiency under modified drivetrain parameters are expected to be reduced.

The simulation results presented in Figure 2.24 are for three cases: 1) nominal parameters,  $f_{osc} = 2.5 \text{ Hz}$ , no damping, 2)  $f_{osc} = 2 \text{ Hz}$ , damping, 3)  $f_{osc} = 3 \text{ Hz}$ , damping. The grid disturbance is the RoCoF = 2 Hz/s. The sharing of the damping effect as well as the damping deactivation are not included to focus on the efficiency of the ZV filter. As shown in Figure 2.24, (d) – (e), when the frequency of oscillatory modes changes, the mechanical vibrations are less damped, and, as expected, the damping efficiency is reduced. However, it is important to mention that in comparison with the nominal parameters case, the results with a non-optimally tuned ZV filter still allow mitigating the amplitude of vibrations. So, only mitigated oscillations are present on the AC side as depicted in Figure 2.24, (a). In Figure 2.24, (b) – (c), it is clear that the parametric variation of the shaft stiffness does not strongly impact the behavior of the electromagnetic torque and the DC bus voltage. Hence, it can be deduced that the chosen IS method-based damping is quite efficient even if the frequency of the drivetrain oscillatory modes differs from the one the filter is originally designed for.

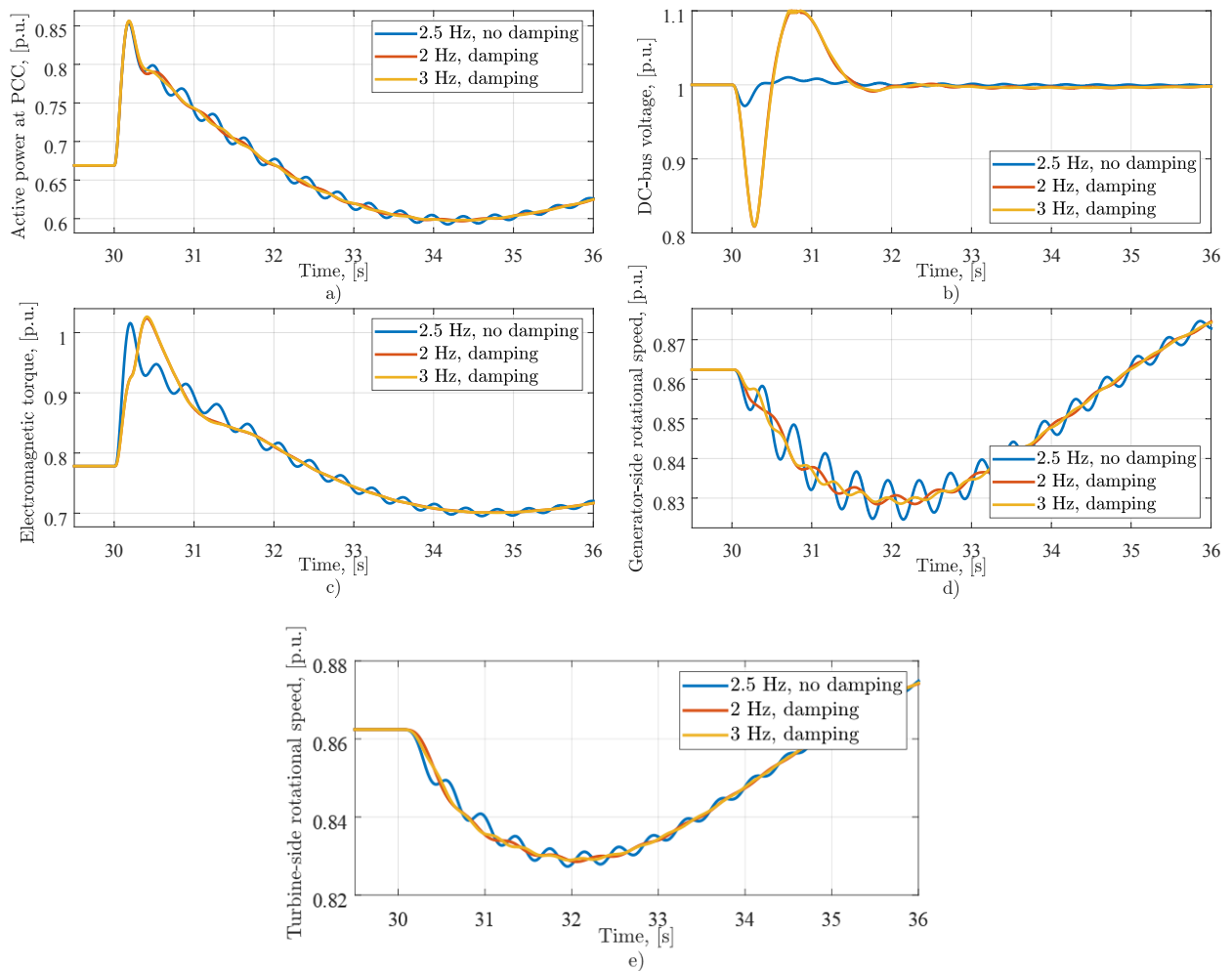


Figure 2.24. Variation of drivetrain shaft stiffness: a) active power at PCC, b) DC bus voltage, c) electromagnetic torque, d) generator-side rotational speed, e) turbine-side rotational speed

Secondly, as explained in Equations 2.10 – 2.11, the efficiency of a ZV filter depends on the estimation of drivetrain oscillatory modes. Therefore, to verify robustness of the ZV filter, it is

assumed that there is an error in the estimation. Several error scenarios are considered in Table 2.2. The maximum error is set to 20%.

Table 2.2. Drivetrain oscillatory modes estimation error scenarios

Scenario	Description
<b>Scenario 1 (S1)</b>	Real part, default, Imaginary part – 20% error $s = -0.88 \pm j12.49$
<b>Scenario 2 (S2)</b>	Real part, default, Imaginary part + 20% error $s = -0.88 \pm j18.74$
<b>Scenario 3 (S3)</b>	Real part – 20% error, Imaginary part – 20% error $s = -0.7 \pm j12.49$
<b>Scenario 4 (S4)</b>	Real part + 20% error, Imaginary part + 20% error $s = -1.05 \pm j18.74$

The scenarios are grouped as following: S1, S2; S3, S4. They are juxtaposed to the default damping case where the ZV filter is adjusted according to accurately estimated drivetrain oscillatory modes. The rest of parameters is the same as in the previous simulation.

In Figure 2.25, the results for scenarios S1, S2 are provided. The error in the imaginary part of drivetrain oscillatory modes has an impact on the damping efficiency as shown in Figure 2.25, (d). Since the vibration damping effect is similar for turbine- and generator-side rotational speed, the results for the turbine-side have been omitted. According to Equation 2.15, the second portion of the electromagnetic torque is more delayed with a smaller frequency of the oscillatory modes (S1). This is confirmed in Figure 2.25, (c). The smaller or bigger delay results in the smaller (S2) or bigger (S1) variation of the DC bus voltage. The oscillations on the AC side also change in Figure 2.25, (a).

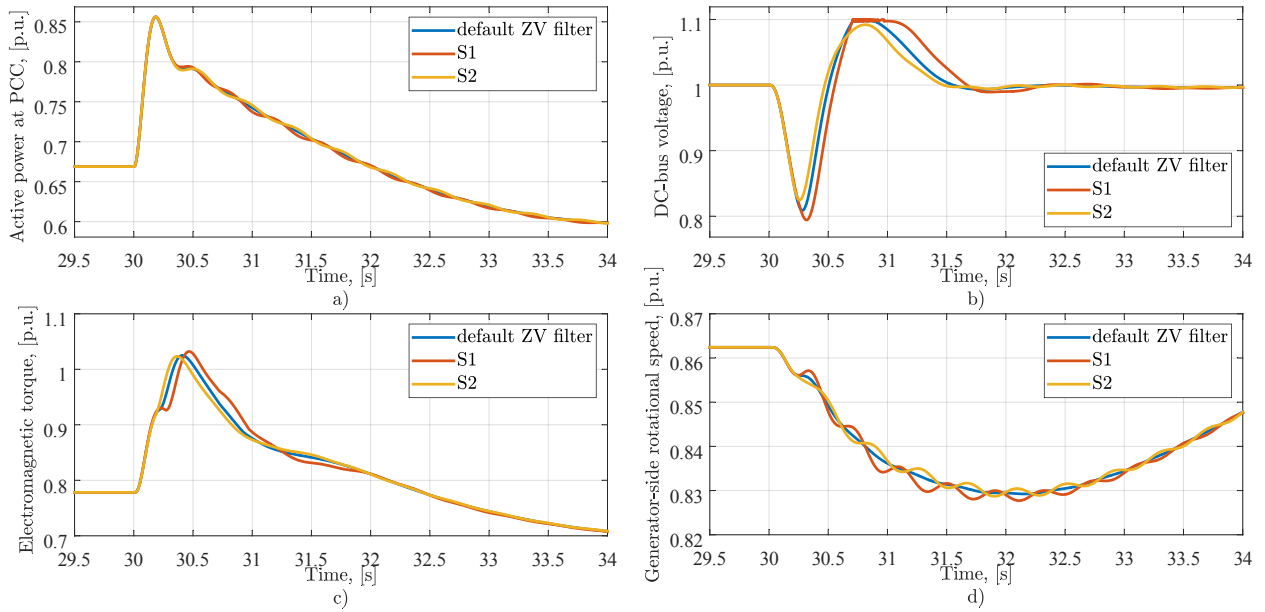


Figure 2.25. Scenarios S1, S2: a) active power at PCC, b) DC bus voltage, c) electromagnetic torque, d) generator-side rotational speed

According to the results in scenarios S1, S2, the error in the imaginary part can have a significant impact on the damping efficiency. In scenarios S3, S4 the error committed in both real and imaginary part. It has been found that the error in the real part of the oscillatory modes has a small impact on the damping efficiency and the results obtained in scenarios S3, S4 also resemble the results in Figure 2.25. That is why they are not shown graphically.

Based on the results from the considered scenarios, it can be concluded that the error in the estimation can reduce damping efficiency. The error in the imaginary part of the oscillatory modes makes a ZV filter less accurate because the imaginary part defines the time delay applied to the electromagnetic torque reference. Inaccurate calculation of this time delay leads to less efficient vibration damping. However, the vibrations are still better damped compared to the case without damping.

## **Conclusions**

In this chapter, it has been identified that there are two electromechanical couplings in a grid-forming wind turbine. While the impact of the MPPT control dynamics on the performance of the grid-forming control can be partially or completely eliminated, the impact of the grid-forming control on the mechanical structure of the wind turbine generator requires more attention. The torsional vibrations, which are a consequence of this coupling, have to be mitigated or suppressed. Among the presented damping solutions, the damping based on the IS method has shown a good performance. The results of the comprehensive analysis of this method have shown that this damping method is very efficient in suppressing torsional vibrations and as well is robust against parametric variations. However, it has been highlighted that there exists a side effect brought with the applied damping, namely increased variations of the DC bus voltage. As discussed in this chapter, this side effect can be mitigated by additional control actions.

### **3. Aggregation of a grid-forming wind power plant**

In the previous chapters the operation of a grid-forming wind turbine has been investigated. A wind turbine constitutes a part of a WPP. Thus, the analysis of a WPP comprised of multiple grid-forming wind turbines, of which the analysis was undertaken in the second chapter, is a logical continuation. The analysis of a detailed WPP model is quite a tedious task that requires much simulation time and computing capacities [106]. Generally, to simplify the analysis, a WPP is aggregated into a dynamic equivalent model (DEM). In this chapter, the aggregation of a WPP into different DEMs such as the Single-Machine equivalent Model (SMM) and the Multi-Machine equivalent Model (MMM) is performed. The aggregation process also takes into account the heterogeneous wind distribution inside a WPP. Under non-uniform wind conditions the calculation of the DEM is more complex. It requires a clustering algorithm to be employed that allows deriving the MMM. In addition, the optimal number of clusters can be found. To generalize the process of selecting the optimal DEM for different wind conditions, the algorithm determining the optimal number of clusters is proposed. This algorithm recommends the optimal DEM to be used depending on the wind conditions. The performance of the algorithm is tested on a case study WPP.

#### **3.1. Types of dynamic equivalent models**

Two main DEMs that can be used to substitute a full WPP model are considered: SMM and MMM. The use of one or another DEM depends on the phenomenon under study. Both DEMs will be presented further with calculation of the equivalent parameters for each type.

##### **3.1.1. Multi-Machine equivalent Model (MMM)**

It has been highlighted in [43] that for power system studies such as rotor angle stability assessments, the aggregation of a WPP into the SMM is not the best solution. Instead, to improve the accuracy of a DEM, a MMM can be utilized [107], [108]. The derivation of the MMM can be based either on the electrical topology of the collector network or on a certain coherency among the wind turbines.

- MMM based on electrical topology

One method presented in literature to obtain a MMM is to consider the electrical topology of a WPP and aggregate each string into the SMM [107]. However, the accuracy of this MMM is often not much better than the accuracy of the SMM [43] because equivalencing wind turbines according to the electrical topology goes against the natural distribution of the wind speed inside a WPP. The generic WPP model and the aggregation into the MMM based on the electrical topology is depicted in Figure 3.1.

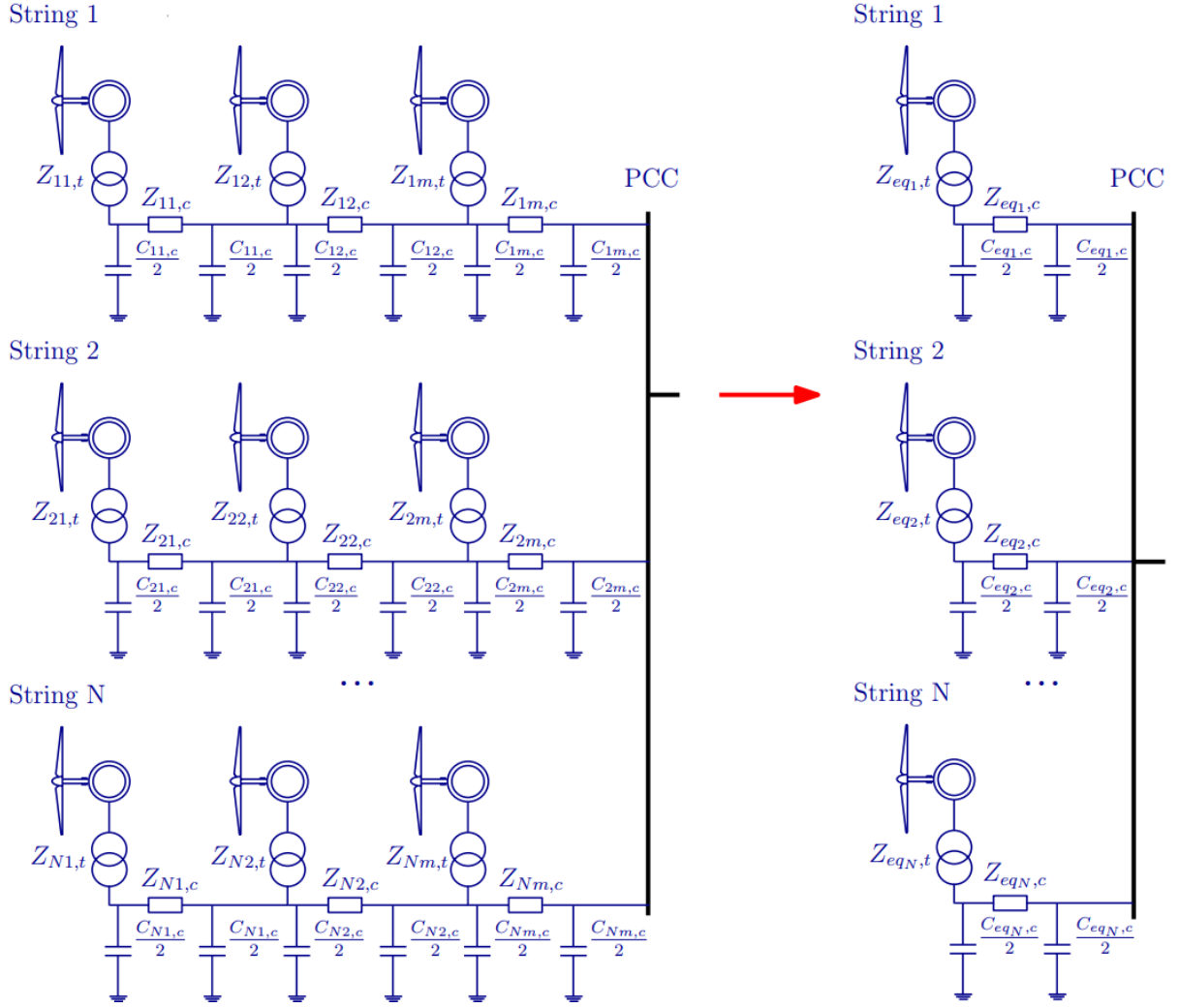


Figure 3.1. Generic WPP aggregation into the MMM based on electrical topology

The denominations of the elements in Figure 3.1 are as following:

- $Z_{ij,t}$  is the impedance of a single transformer;
- $Z_{ij,c}, C_{ij,c}$  is the impedance and capacitance of the cable between two wind turbines;
- $m_i$  is the number of wind turbines in the  $i$ -th string;
- $N$  is the number of strings.

The parameters of the equivalent model are defined accordingly:

- $Z_{eqi,t}$  is the impedance of the equivalent transformer of the  $i$ -th string;
- $Z_{eqi,c}, C_{eqi,c}$  is the equivalent impedance and capacitance of the  $i$ -th string.

The assumption is that all wind turbines inside a WPP receive the same wind speed. The MMM is aggregated into several individual SMMs. The calculation of equivalent parameters of each SMM can be performed differently depending on whether the wind turbines in the WPP are same or not. If the wind turbines connected to a single string are different, the capacity weighted average method is commonly utilized [109], [110]. In this thesis, however, the WPP is assumed to contain only wind turbines of the same type and nominal capacity. Under this assumption, the commonly applied aggregation steps are described below.

a. Equivalent wind turbine capacity of the  $i$ -th string

$$S_{eq_i} = \sum_{j=1}^{m_i} S_{ij} \quad (3.1)$$

where  $S_{ij}$  is the nominal capacity of the  $j$ -th wind turbine,  $m_i$  is the number of wind turbines in the  $i$ -th string.

b. Equivalent impedance of the wind turbine transformer of the  $i$ -th string

The same wind turbine type and capacity imply that the transformers are also the same. Assuming that the wind turbine transformer impedance is given in per-unit, its equivalent impedance for the  $i$ -th string can be computed by substituting the nominal capacity of a wind turbine to the equivalent capacity of the  $i$ -th string, as defined in Equation 3.1:

$$Z_{eq_i,t} = \frac{Z_{im_i,t}}{m_i} \quad (3.2)$$

c. Equivalent impedance of the collector network of the  $i$ -th string

The aggregation of series impedances of the  $i$ -th string is based on the power losses equivalence [111]. Assuming that the current from each wind turbine is the same in magnitude and phase, the current flowing from the wind turbines of  $i$ -th string to the PCC is deduced as:

$$I_{pcc,s_i} = \sum_{j=1}^{m_i} I_{ij} \quad (3.3)$$

where  $I_{ij}$  is the current produced by the  $j$ -th wind turbine,

$R_{eq_i,c}$   $X_{eq_i,c}$  are the equivalent series resistance and reactance of the  $i$ -th string,  $R_{ij,c}$ ,  $X_{ij,c}$  are the series resistance and reactance between the  $j$ -th and the  $j + 1$ -th wind turbine in the  $i$ -th string.  $R_{eq_i,c}$   $X_{eq_i,c}$  are defined such that the equivalent active and reactive power are equal to the sum of the elementary active and reactive power in the series impedance:

$$P_{loss_i} = I_{pcc,s}^2 R_{eq_i,c} = \sum_{j=1}^{m_i} \left( \frac{I_{pcc,s_i j}}{m_i} \right)^2 R_{ij,c} \quad (3.4)$$

$$Q_{loss_i} = I_{pcc,s}^2 X_{eq_i,c} = \sum_{j=1}^{m_i} \left( \frac{I_{pcc,s_i j}}{m_i} \right)^2 X_{ij,c} \quad (3.5)$$

From Equations 3.4 – 3.5 the equivalent series impedance of the  $i$ -th string is expressed as:

$$R_{eq_i,c} = \frac{1}{m_i^2} \sum_{j=1}^{m_i} j^2 R_{ij,c} \quad (3.6)$$

$$X_{eq_i,c} = \frac{1}{m_i^2} \sum_{j=1}^{m_i} j^2 X_{ij,c} \quad (3.7)$$

The capacitance of different cable sections in the  $i$ -th string can be summed under the assumption that the voltage in the whole string is uniform:

$$C_{eq_i} = \sum_{j=1}^{m_i} C_{ij} \quad (3.8)$$

where  $C_{ij}$  is the capacitance of the  $j$ -th cable section in the  $i$ -th string.

- MMM based on a common parameter (cluster-based MMM)

The MMM based on the electrical topology can reflect the dynamic characteristics of a WPP under the simplifying assumption that the wind speed distribution among the wind turbines can be disregarded. When considering a heterogeneous wind speed distribution, on the contrary, another type of the MMM is recommended to be used. In this work this MMM type is named as the cluster-based MMM to distinguish it from the MMM based on electrical topology. For this type of the MMM, a common parameter between the wind turbines is identified, and the wind turbines are grouped into clusters. The cluster-based MMM significantly improves the dynamic characteristic of the equivalent model and converges closely to the dynamics of the detailed WPP.

The criterion for clustering can be based on one or several common parameters such as:

- wind turbine type [112], protection action [113], [114];
- operating point [115]–[117], rotor speed [118]–[120], wind turbine location [121];
- wind speed [108], [122]–[126].

In this thesis, all wind turbines are of the same type and nominal capacity. This implies that also the control parameters of the wind turbines are the same. The wind turbines can thus be clustered based on the criterion of the operating point, rotor speed or wind turbine location. However, relying on these criteria can lead to inaccuracies if the wind turbines operate above the rated wind speed, which can be in the region of 11 – 12 m/s. The criterion based on the wind speed, on the contrary, allows distinguishing wind turbines into clusters even at high wind speeds. The use of this criterion thus has the potential to increase the accuracy of the resulting aggregated model. Therefore, in this thesis, the selected clustering criterion is the one based on the wind speed.

The same generic WPP with 3 clusters highlighted with blue, green and magenta colors is shown in Figure 3.2. The upstream wind is assumed to blow in the south-east direction.

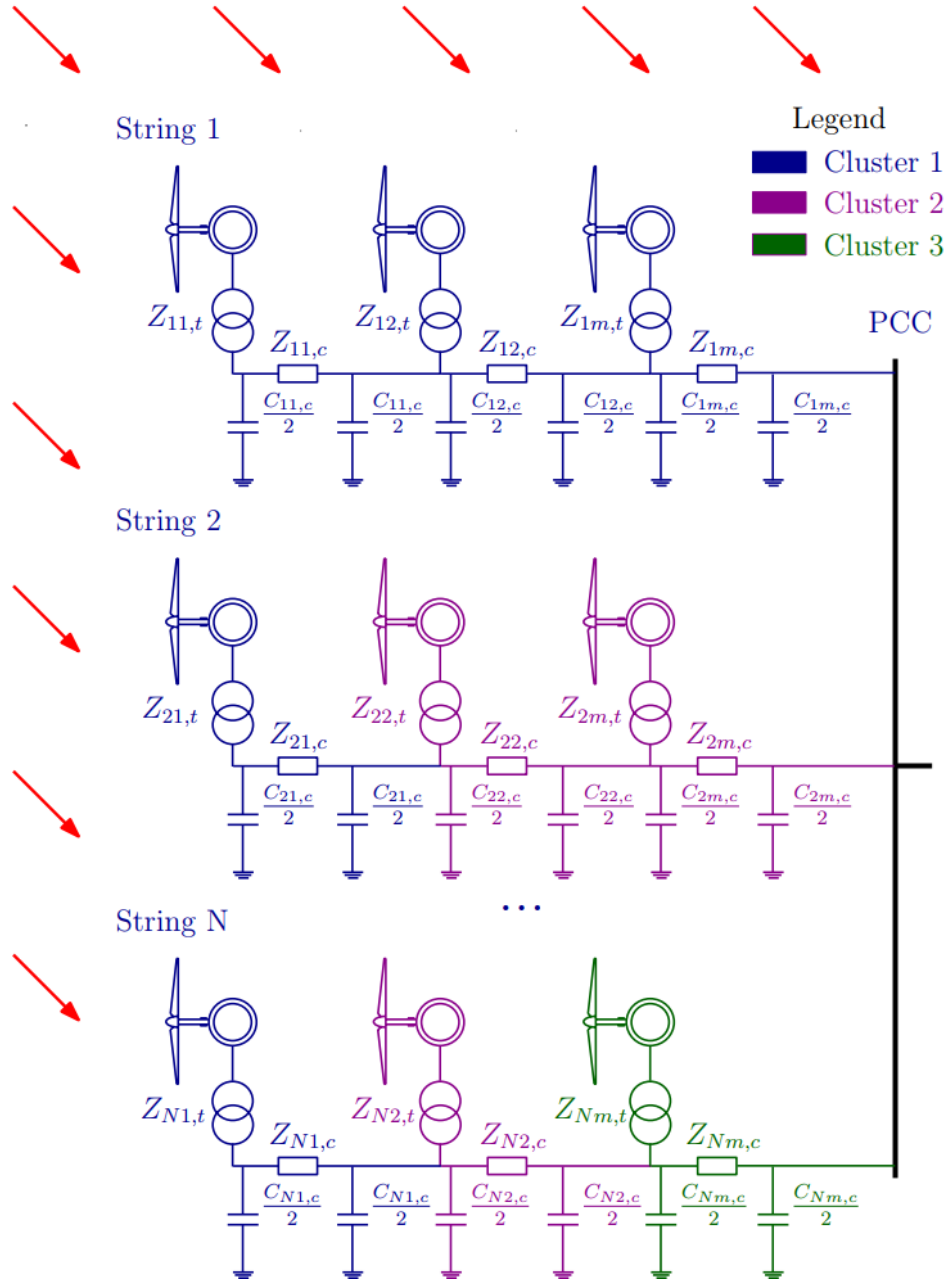


Figure 3.2. Generic WPP with highlighted clusters

As noted, the cluster-based MMM is based on a common parameter. The selected common parameter is the wind speed that is considered different from one wind turbine to another. The cluster-based MMM includes one or several individual SMMs. Each of them represents a single cluster. Since in the cluster-based MMM, the electrical topology is not the clustering criterion, the derivation of these individual equivalent parameters is different from the MMM based on electrical topology.

The equivalent wind speed of the  $g$ -th cluster is expressed as the average wind speed:

$$v_{eq}^{cl} = \frac{1}{m_g^{cl}} \sum_{k=1}^{m_g^{cl}} v_{ik} \quad (3.9)$$

where  $m_g^{cl}$  is the number of wind turbines in the  $g$ -th cluster.

The equivalent nominal capacity and the wind turbine transformer equivalent impedance of the  $g$ -th cluster can be determined similarly to Equations 3.1 – 3.2 when substituting the number of the wind turbines in a string by the number of the wind turbines in a cluster.

The derivation of the equivalent impedance of the collector network of the  $g$ -th cluster is also based on the power losses. These losses have been presented previously in Equations 3.4 – 3.5, but now the methodology has to be adapted. Let us take the example of cluster 2. The wind turbines of this cluster are located in strings 1, 2 and 3 as shown in Figure 3.3. Firstly, the SMM including only wind turbines of cluster 2 has to be developed for each string. Secondly, the SMM of each string has to be aggregated in parallel in order to obtain the final equivalent model of cluster 2.

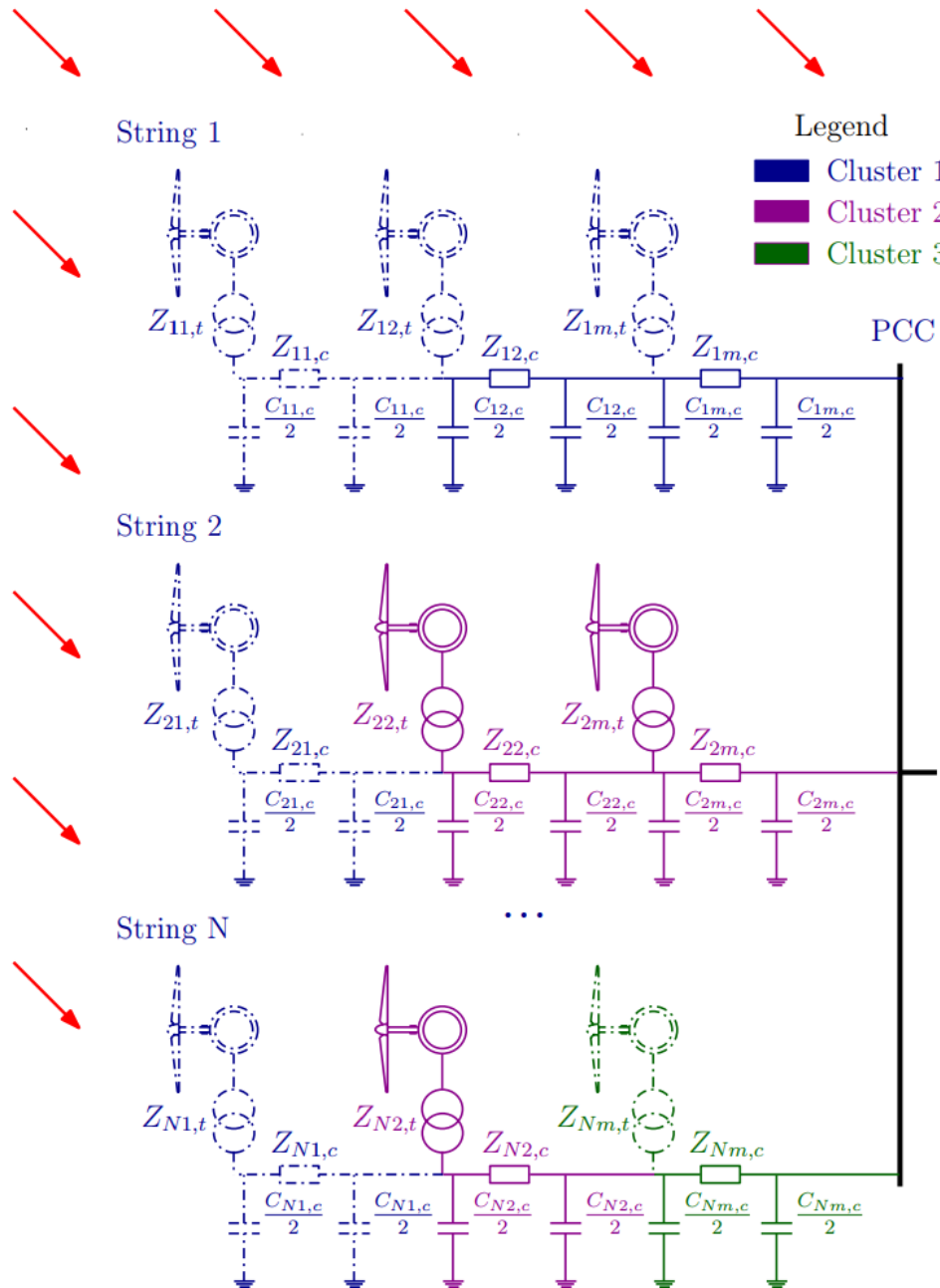


Figure 3.3. Generic WPP for cluster 2

The process of deriving the equivalent impedance of a cluster is as follows:

To calculate equivalent resistance,  $R_{i,c}^g$ , and reactance,  $X_{i,c}^g$  of the  $i$ -th string for the  $g$ -th cluster, only the parameters of the wind turbines belonging to this cluster are taken into consideration. Let us define  $N_{wt,i}^g$  as the number of wind turbines of the  $g$ -th cluster in the  $i$ -th string. With the same approach as in Equations 3.6 – 3.7, the following expression can be written:

$$R_{i,c}^g = \frac{1}{N_{wt,i}^g} \sum_{k=1}^{N_{wt,i}^g} k^2 R_{ik} \quad (3.10)$$

$$X_{i,c}^g = \frac{1}{N_{wt,i}^g} \sum_{k=1}^{N_{wt,i}^g} k^2 X_{ik} \quad (3.11)$$

Then, the additional resistance,  $R_{add,i,c}^g$ , and reactance,  $X_{add,i,c}^g$ , of other cable sections connecting wind turbines of the  $g$ -th cluster in the  $i$ -th string to the PCC are added.

$$R_{eq,i,c}^g = R_{i,c}^g + R_{add,i,c}^g \quad (3.12)$$

$$X_{eq,i,c}^g = X_{i,c}^g + X_{add,i,c}^g \quad (3.13)$$

In the example of cluster 2:

- string 1:  $R_{add1,c}^2 = 0, X_{add1,c}^2 = 0$ ;
- string 2:  $R_{add2,c}^2 = 0, X_{add2,c}^2 = 0$ ;
- string  $N$ :  $R_{addN,c}^2 = R_{Nm}, X_{addN,c}^2 = X_{Nm}$ .

Then, the equivalent impedances of each string are aggregated in parallel into the equivalent cluster resistance,  $R_{eq,i,c}^{cl}$ , and reactance,  $X_{eq,i,c}^{cl}$ .

$$R_{eq,i,c}^{cl} = \frac{1}{\sum_{i=1}^N \frac{1}{R_{eq,i,c}^g}} \quad (3.14)$$

$$X_{eq,i,c}^{cl} = \frac{1}{\sum_{i=1}^N \frac{1}{X_{eq,i,c}^g}} \quad (3.15)$$

For the sake of completeness, it should be noted that the aggregation method still induces an approximation on the active power losses since the currents generated by the wind turbines, not belonging to the cluster, are not taken into account in the equivalent cable loading.

The capacitance of cable sections in the  $i$ -th cluster is also summed under the assumption of a uniform bus voltage.

$$C_{eq_g}^{cl} = \sum_{k=1}^{m_g^{cl}} C_{gk} \quad (3.16)$$

where  $C_{ik}$  is the capacitance of the  $k$ -th cable section in the  $g$ -th cluster.

Once the equivalent parameters for the clusters are determined, the cluster-based MMM is finally obtained. The resulting model is depicted in Figure 3.4 where  $N^{cl}$  is the number of clusters.

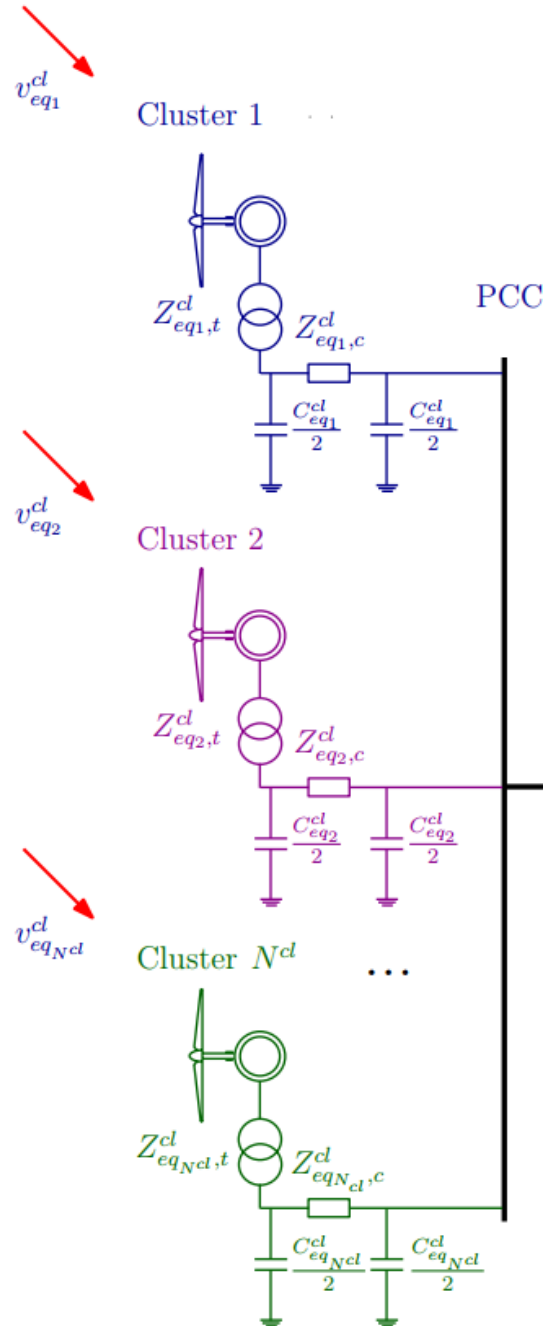


Figure 3.4. Cluster-based MMM

### 3.1.2. Single-machine equivalent model

The SMM is the equivalent model that represents a WPP with a single wind turbine. Often, the fundamental assumption for the SMM is that the wind speed is homogeneously distributed across the entire WPP [107]. The SMM can also be used when the heterogeneous wind distribution is considered. In this case, the SMM is the particular case of the cluster-based MMM with one cluster.

Since, the wind speed is heterogeneously distributed across the WPP, the equivalent wind speed is obtained by finding the average wind speed value as:

$$v_{eq}^{SMM} = \frac{1}{N_{WPP}} \sum_{j=1}^{N_{WPP}} v_{ij} \quad (3.17)$$

where  $N_{WPP}$  is the total number of wind turbines in a WPP.

The equivalent nominal capacity and the wind turbine transformer equivalent impedance of one string can be determined similarly to Equations 3.1 – 3.2. The equivalent series resistance and reactance of one string can be found similarly to Equations 3.6 – 3.7.

Considering several parallel strings to be aggregated, the final equivalent resistance and reactance of the SMM can be found as:

$$R_{eqSMM} = \frac{1}{\sum_{i=1}^N \frac{1}{R_{eqi,c}}} \quad (3.18)$$

$$X_{eqSMM} = \frac{1}{\sum_{i=1}^N \frac{1}{X_{eqi,c}}} \quad (3.19)$$

The equivalent capacitance of the cable can be found analogously to Equation 3.16.

## 3.2. Wind distribution modelling

As discussed, the cluster-based MMM has good prospects to represent a WPP. However, it should be combined with an accurate model of the wind distribution, which should be as close as possible to the real wind distribution across a WPP. Such combination will allow the cluster-based MMM to reflect the dynamics of a detailed WPP model. In this section, the wind distribution modelling used in this thesis is described.

### 3.2.1. General description

After passing a wind turbine the wind speed slows down and becomes more turbulent. This is known as the wake effect. The wake effect has a significant impact on the wind speed distribution in a WPP. Starting at the upstream wind turbine, a wake can propagate for several kilometers [127], [128]. A combination of wakes from multiple wind turbines influences the downstream wind, so

that the wind speed is distributed non-uniformly across a WPP. Thus, it is important to have a relevant wake model and a precise methodology for the wind speed distribution modelling. The proper modelling of the wake effect can help to estimate the power production of a WPP. Also, heterogeneous wind speed distribution can be useful for the analysis of the WPP operation. The wind distribution modelling can be divided in two main steps: wake modelling and wakes merging. The first step is related to the choice of the wake model and its description. The second step deals with multiple wakes from multiple wind turbines by merging these wakes with each other.

- Wake modelling

The classical and the first analytical wake model is the Jensen model. The model is widely utilized [129], [130] and describes the wake effect induced by one wind turbine. The Jensen wake model is expressed as a normalized wind speed deficit in the wake:

$$\frac{\Delta U(\mathbf{x})}{U_b} = \frac{1 - \sqrt{1 - C_T}}{\left(1 + \frac{2\delta(x)}{D}\right)^2} \left(\frac{D}{2} + \delta(x) - r(\mathbf{x})\right) \quad (3.20)$$

where

- $\Delta U(\mathbf{x}) = U_b - U(\mathbf{x})$  is the wind speed deficit in the wake;
- $U_b$  is the background (upstream) wind speed considered to be uniform and unidirectional ( $y$  and  $z$  components are zeros);
- $U(\mathbf{x})$  is the wind speed influenced by the wake effect;
- $\mathbf{x} = (x, y, z)$  is a coordinate vector with horizontal  $x$ , lateral  $y$  and vertical  $z$  directions;
- $r(\mathbf{x}) = (z^2 + y^2)^{1/2}$  is the radial distance from the wake center;
- $C_T$  is the wind turbine thrust coefficient;
- $\delta(x) = xk^*$  is the wake width,  $k^*$  is the wake expansion coefficient that can be set as  $k^* = 0.08$  for upstream wind turbines and  $k^* = 0.04$  – for other wind turbines;
- $D$  is the turbine diameter.

The illustration of the Jensen wake model is shown in Figure 3.5.

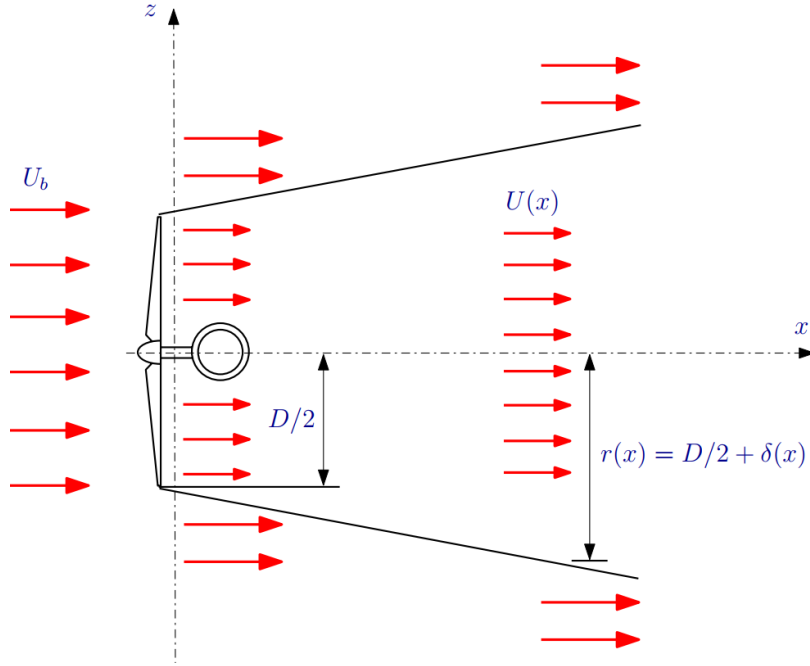


Figure 3.5. Illustration of the wake effect with Jensen model

The Jensen model underestimates the wind speed deficit,  $\Delta U(\mathbf{x})$ , at the wake center and overestimates it at the wake edges [131]. As a result, this model can have significant errors in the prediction of the WPP production [132], [133]. In [133] it is shown that if  $\Delta U(\mathbf{x})$  is plotted against the radial distance from the wake center, it resembles a Gaussian curve and that there is a self-similarity in the turbine wake. Therefore, the Gaussian wake model can be used as an alternative to the Jensen model. The normalized wind speed deficit derived with the Gaussian wake model is presented below:

$$\frac{\Delta U(\mathbf{x})}{U_b} = W(\mathbf{x}) \quad (3.21)$$

where  $W(\mathbf{x}) = C(x)f(r(x), \sigma(x))$ ,  $C(x)$  is the maximum wind speed deficit estimated at a chose location,  $\sigma(x)$  is the standard deviation of the Gaussian function varying downstream,  $f(r(x), \sigma(x))$  is the shape of the wind speed profile.

The maximum wind speed deficit and the shape of the wind profile are derived as following:

$$C(x) = 1 - \sqrt{1 - \frac{c_T}{8(\sigma(x)/D)^2}} \quad (3.22)$$

$$f(r(x), \sigma(x)) = e^{-\frac{r(x)^2}{\sigma(x)^2}} \quad (3.23)$$

This Gaussian model outperforms the Jensen model and is used for the optimization of WPP topologies and for the estimation of wakes in a WPP [134], [135]. Improved wake models have also been proposed in the literature as super-Gaussian [136], [137], double-Gaussian [138], [139] and Ishihara wake models [140].

- Wakes merging

In order to model the wake effects inside a WPP, multiple wake models have to be merged together. These wakes will cross and interact with each other. To take the wake overlapping into account and calculate the merged wake effect at each WPP location, superposition methods are utilized. These methods are based on a summation of the wind speed deficits [132], [141] or on summation of the square of the wind speed deficits [142]. In this thesis, the first method is used. It uses the linear superposition of wind speed deficits and allows getting the wind speed at each coordinate of a WPP using the following equation:

$$U(\mathbf{x}) = U_b - \sum_{k=1}^{N_t} u_k W_k(\mathbf{x}) \quad (3.24)$$

where

- $u_k$  is the average wind speed over the  $k$  – th turbine rotor;
- $u_k W_k(\mathbf{x})$  is the wind speed deficit;
- $N_t$  is the number of wind turbines.

In this thesis, the described wind distribution modeling is performed using the tool designed by L. Lanzilao in [131]. The example of the use of the described wind distribution model is presented for a generic string of six wind turbines in Figure 3.6 with a normalized wind speed. The upstream wind speed is 13.5 m/s. The example shows that the upstream wind turbine influences the wind distribution downstream. It confirms that with a wake effect the wind distribution in one string of a WPP is heterogeneous. Hence, same can be applied to a scale of a WPP.

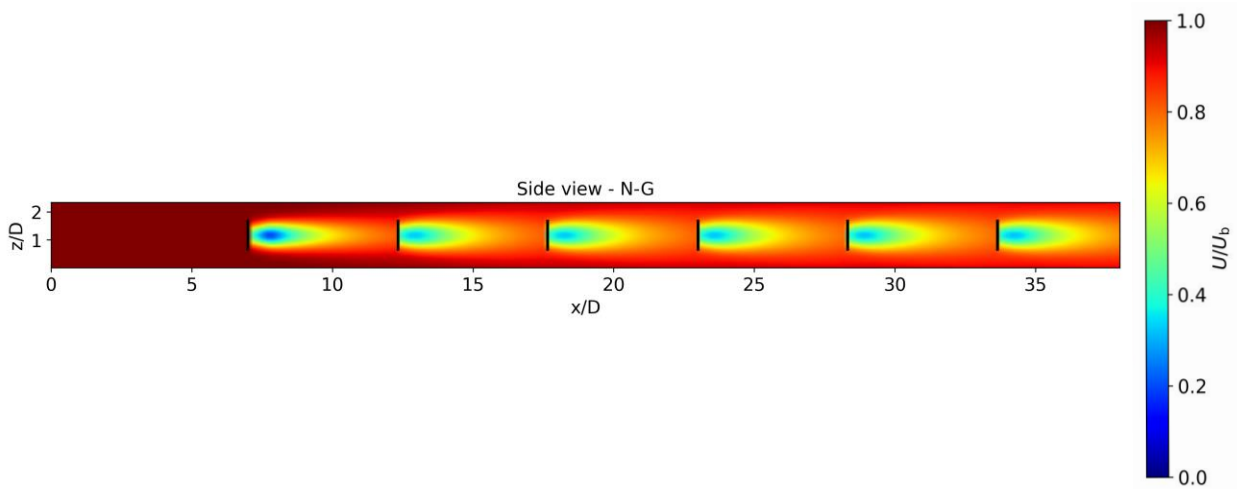


Figure 3.6. Wind speed distribution in a string of wind turbines

### 3.2.2. Application of the wind distribution model to the case study WPP

The wind distribution model is applied to the case study WPP. This WPP is the 300-MW Thanet offshore wind farm located in South England at 11 km from shore, as shown in Figure 3.7.

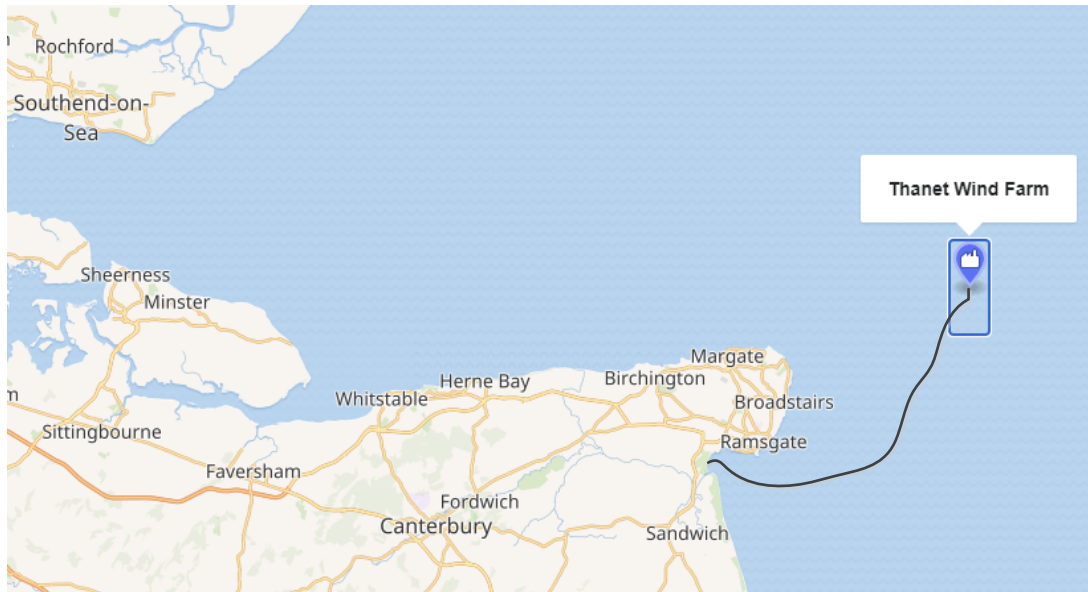


Figure 3.7. Geographical location of Thanet WPP

The electrical topology of the collector network is presented in Figure 3.8. The WPP contains 10 strings, with each string containing 10 wind turbines.

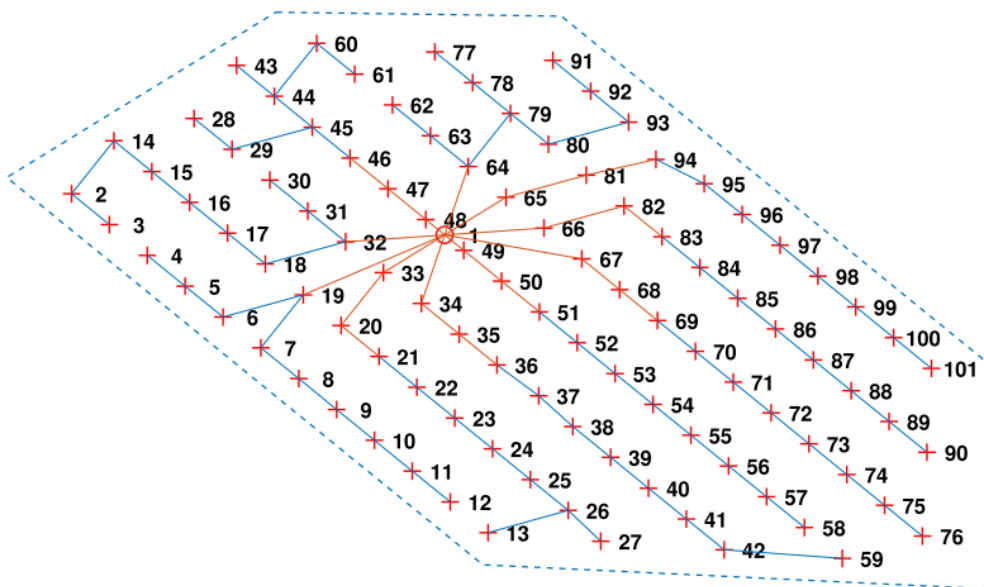


Figure 3.8. Collector network of Thanet WPP [143]

The WPP is connected to the PCC at bus '1' with two 180 MVA transformers in parallel, which step-up the collector network voltage from 33 kV to 132 kV. In Figure 3.63, taken from [143], the high-voltage subsea cable sections are drawn in light-blue and orange colors. The lines in light-blue indicate cables with a cross-section of  $240 \text{ mm}^2$ , the orange ones imply  $300 \text{ mm}^2$ . The average distance between the wind turbines is around  $5D$ . The average distance between strings is around  $7D$ . The cable electrical characteristics of this WPP, provided in [144] are presented in Table 3.1.

Table 3.1. Cable electrical parameters

Parameter	Value	
Cross-section, $mm^2$	240	300
Current carrying capacity, $A$	540	620
DC resistance at 20°C, $\Omega/km$	0.0754	0.0601
Nominal inductance, $mH/km$	0.368	0.357
Nominal capacitance, $\mu F/km$	0.223	0.244

The model of the WPP is presented in Figure 3.9, in which only 3 out of the 10 strings are depicted. With the focus on the aggregation of the WPP, the connection-to-shore cable has been replaced with an equivalent grid impedance under the assumption that the external grid is strong ( $SCR = 20$ ). Each wind turbine is modeled as a grid-forming wind turbine, with the model as discussed in Chapters 1 – 2. However, the voltage reference generation is changed to include the current limitation algorithm described in Appendix A. The rated power of a single wind turbine is changed from 5 MW to 3 MW in order to comply with the WPP total capacity of 300 MW. The parameters of this 3-MW wind turbine as well as other system model parameters are provided in Table 3.2 – Table 3.6. The damping of torsional vibrations with the IS method is turned on as well as the damping de-activation feature. The sharing of the damping effect between the MSC and the GSC is turned off.

Also, a centralized reactive power regulation is added at the PCC. It includes a  $Q(V)$  droop function, PI controller and reference limitation, that is based on the limits acquired from the PQ capability diagram at the WPP bus. The detailed description of this centralized controller is presented in Appendix B.

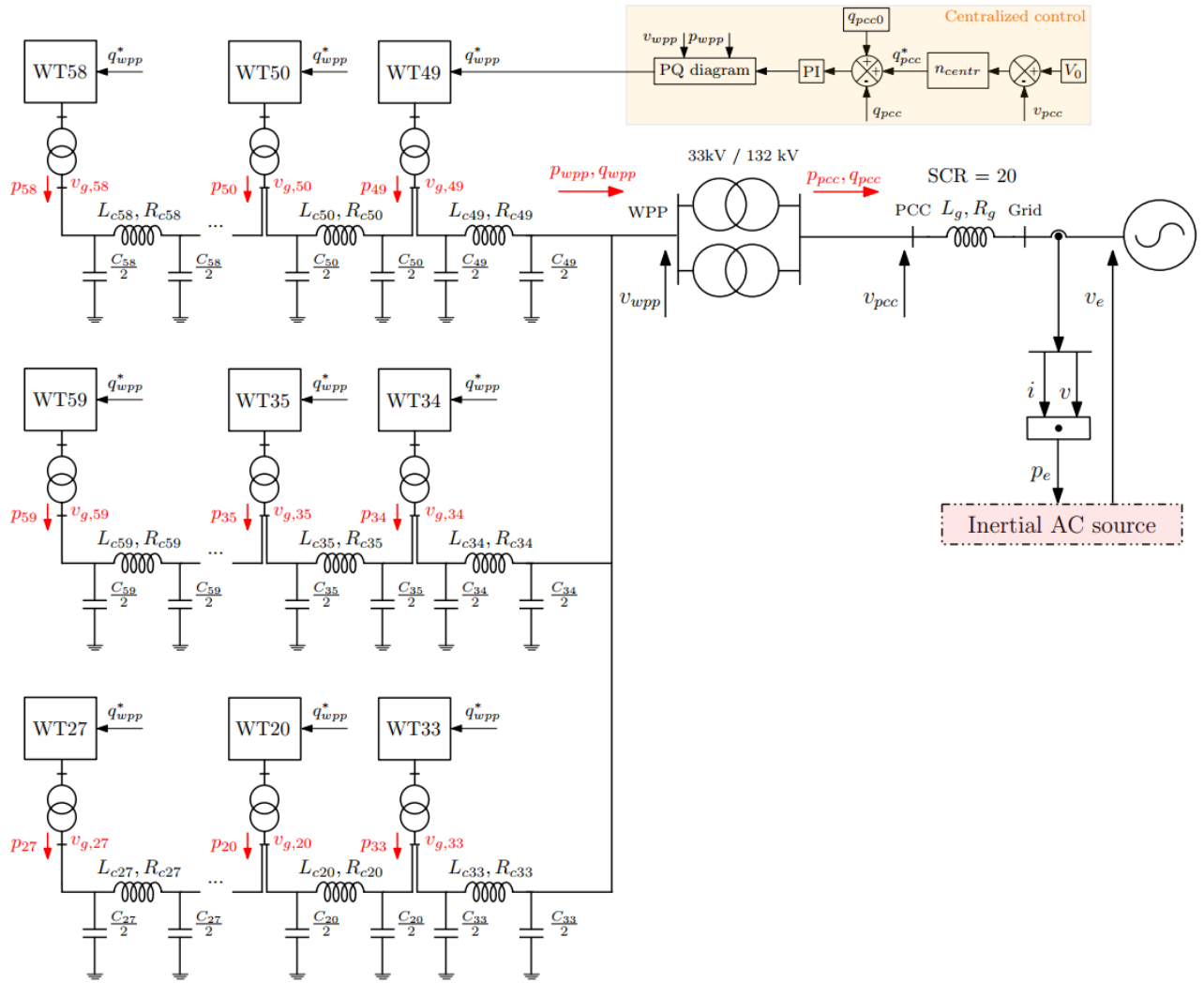


Figure 3.9. WPP model

Table 3.2. Grid parameters

Parameter	Value
Nominal grid power, $S_g$	1 GVA
Nominal grid voltage, $U_{g,MV}, U_{g,HV}$	33 kV, 132 kV
Short-circuit ratio, $SCR$	20
Grid impedance, $r_g, l_g$	0.005 pu, 0.05 pu
<b>Simplified SM parameters:</b>	
Steam turbine constants: $T_N, T_D$	1, 6
Frequency droop, $R_{SG}$	4 %
Equivalent inertia constant, $H_{eq}$	5 s

Table 3.3. PCC transformer parameters

Parameter	Value
Nominal power, $S_t$	180 MVA
Nominal voltage, $U_{MV}, U_{HV}$	33 kV, 132 kV
Impedance, $r_t, l_g$	0 pu, 0.12 pu

Table 3.4. Grid-side converter and transformer parameters

Parameter	Value
Nominal power, $S_c$	3 MVA
Nominal voltage, $U_{m,LV}, U_{m,MV}$	0.69 kV / 33 kV
Connection impedance, $r_c, l_c$	0 pu, 0.15 pu

Table 3.5. Parameters of wind turbine

Parameter	Value
Wind turbine nominal power, $P_{wt}$	3 MW
Rated rotational speed, $\omega_{t,nom}$	1.686 rad/s
Cut-in, Rated, Cut-out wind speed, $v$	3 m/s, 12.05 m/s, 25 m/s
Turbine rotor radius, $R_{wt}$	45 m
Optimal tip-speed ratio, $\lambda_{opt}$	6.29
Optimal power coefficient, $C_{p,opt}$	0.44
Shaft stiffness, $K_s^{pu}$	822 pu
Shaft mutual damping, $D_s^{pu}$	2.94 pu
Turbine inertia constant, $H_t$	3.4 s
Generator inertia constant, $H_g$	1.42 s
Nominal DC bus voltage, $U_{dc}$	1500 V
DC bus capacitance, $C_{dc}$	0.1 F
Minimal and maximal DC bus voltage deviation, $u_{dc,min/max}$	0.9 pu / 1.1 pu

Table 3.6. Controller parameters

Parameter	Value
Grid-forming control inertia constant, $H$	3.5 s
Grid-forming control damping gain, $k_p$	0.0097
Gain, $m_p$	1/50
Reactive droop gain, $n_q$ , cut-off frequency, $\omega_q$	0.375, 10 rad/s
<b>Current limitation:</b>	
$\tau_{cc}, I_{max,sat}$	30 ms, 1.2 pu
<b>PLL control:</b>	
Settling time, $\tau_{pll}$ , damping, $\xi_{pll}$	40 ms, 0.707
<b>DC bus voltage control:</b>	
Settling time, $\tau_{dc}$ , damping, $\xi_{dc}$ , $T_{dc}$	2 s, 0.707, 0.005 s
<b>DC chopper:</b>	
DC resistance, $R_{dc}$ ,	0.45 Ohm
<b>Pitch control:</b>	
Settling time, $\tau_{pitch}$ , damping, $\xi_{pitch}$ , time constant, $T_{pitch}$	4 s, 0.707, 0.1 s
<b>Vibrations Damping (ZV filter):</b>	
Drivetrain oscillatory poles, $s_{12}$	$-0.93 \pm j20.188$
ZV filter gains, $A_1, A_2$	0.53, 0.46
Time delays, $t_1, t_2$	0 s, 0.155 s
<b>Centralized reactive power controller:</b>	
Reactive droop gain, $n_{centr}$ , cut-off frequency, $\omega_{centr}$	0.125,
Voltage limits at PCC, $v_{pcc,min}, v_{pcc,max}$	0.95 pu, 1.05 pu
PI controller settling time, $t_{PI}$ , damping, $\xi_{PI}$	0.05 s, 0.707

The coordinates of the wind turbine locations normalized with a diameter of a wind turbine are depicted in Figure 3.10.

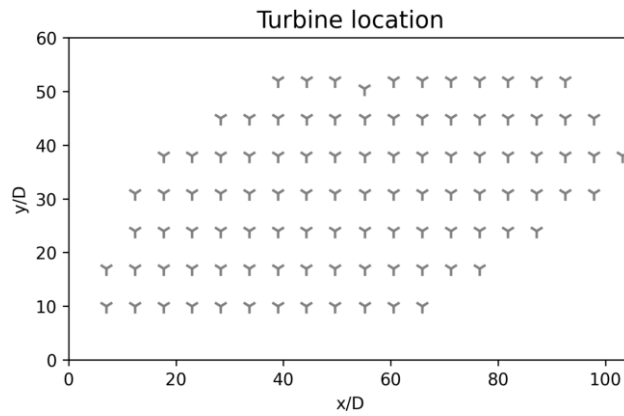


Figure 3.10. Wind turbine locations in Thanet WPP

The wind speed distribution inside the WPP is shown in Figure 3.11 with the coloring based on a normalized wind speed. The upstream wind speed,  $U_b$ , is 13.5 m/s with an eastern direction and is assumed to be uniform. It is clear from the figure that the wind speed in a WPP is heterogeneously distributed and almost each wind turbine is impacted by the wake effect of the upstream wind turbines. The minimum value of the wind speed is 10.5 m/s, corresponding to the wind turbine in the most downstream wind turbine in the bottom row. So, in this model the lowest wind speed is reduced by 22% compared to the upstream wind speed.

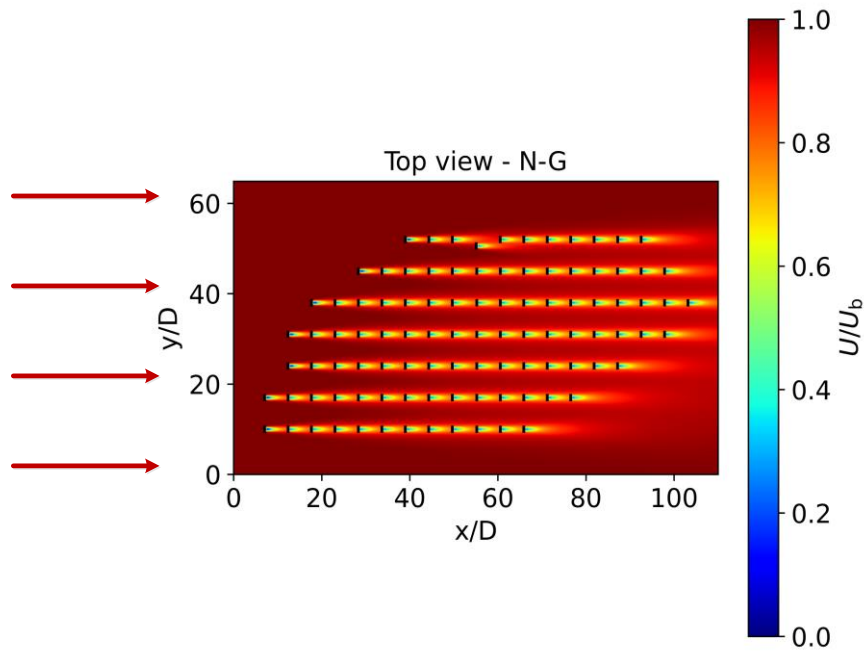
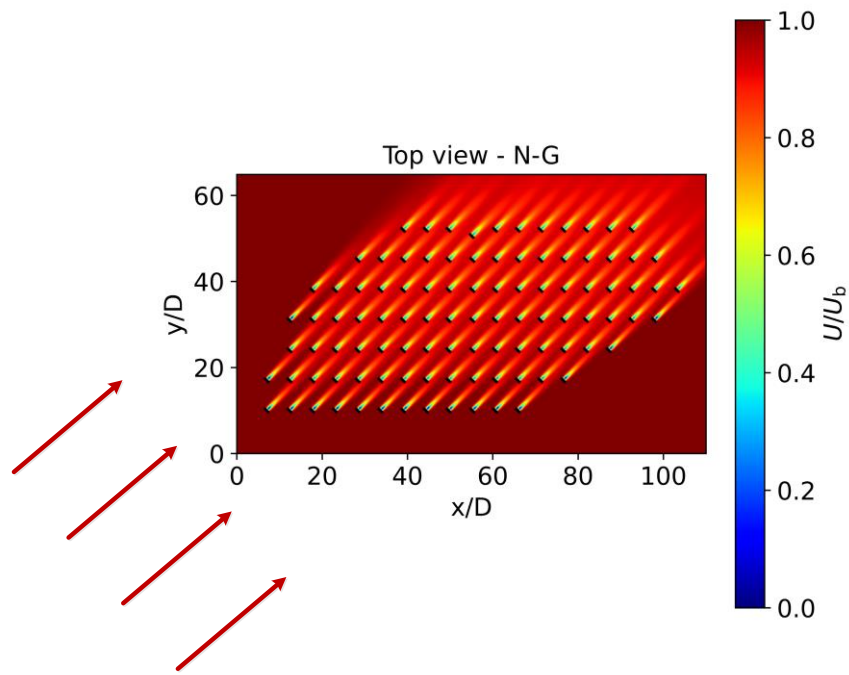


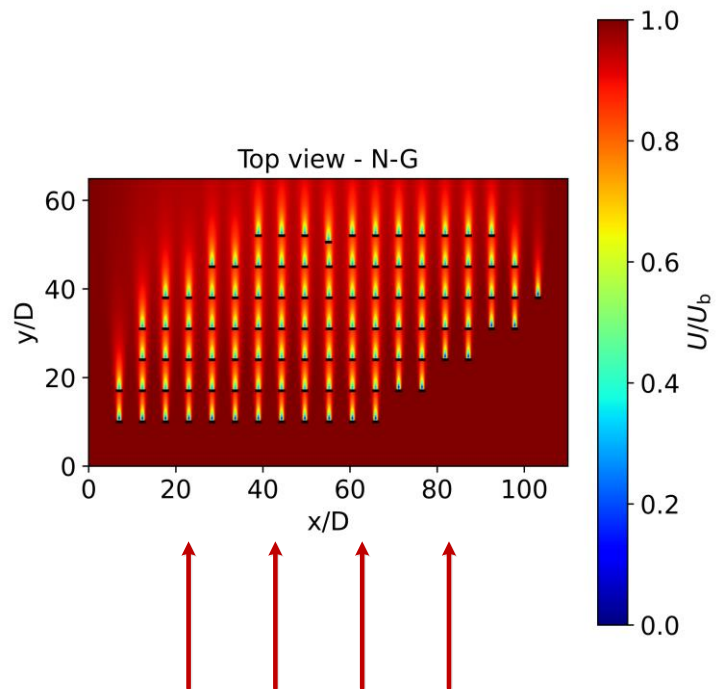
Figure 3.11. Wind speed distribution in a case study WPP, eastern wind direction

Depending on the wind direction, the wind distribution will be different. For example in Figure 3.12 the wind direction is changed to north-eastern and northern, so the wind distribution changes completely. With the variation of the wind direction, the impact of the wake effect on the wind distribution is different. For example, for the north-eastern wind direction in Figure 3.12, (a), the minimum wind speed is 11.7 m/s which is different from the previous case. Similarly for the north wind direction in Figure 3.12, (b), the minimum wind speed is 11.1 m/s. This minimum is

different from previous cases because in this case the wake effect has different impact on the most downstream wind turbines.



a)



b)

Figure 3.12. North-eastern (a) and northern (b) wind direction

### 3.3. Clustering algorithm

In the previous section dedicated to the modelling of the wind distribution, it was demonstrated that the wind turbines at different locations inside a WPP experience different wind speeds. In addition, as presented in Chapter 1, the wind turbine itself is a highly non-linear system, as it can operate in different operating zones.

It is thus, for instance, possible to have some upstream wind turbines which operate in the pitch-regulated (power limitation) zone and some wind turbines downstream – in the power optimization zone. To illustrate the complexity from the point-of-view of the clustering, let us now consider that there is a disturbance on the grid side and that the GSC of the upstream and downstream wind turbines provide an inertial response. In such a case, it is possible that the upstream wind turbines will switch to the current-limited mode, but not the downstream wind turbines. Another possible case is that the downstream wind turbines also saturate but not at the same instant as the upstream wind turbines. Assuming that in this case, the behavior of roughly half of the wind turbines can be approximated by that of the upstream wind turbine, roughly half by the most downstream wind turbine, it is clear that in order to get a high-accuracy cluster-based MMM, the WPP should be aggregated into at least 2 clusters. If the dissimilarity among wind turbines becomes more significant as a result of the complex current-limiting behavior, it is possible that the cluster-based MMM with more clusters becomes more accurate. Therefore, an optimal clustering is crucial for obtaining a sufficiently accurate DEM.

In this section the  $k$  – means clustering algorithm used in this thesis is described and the results of clustering of the case study WPP are provided.

#### 3.3.1. Description of the clustering algorithm

Different clustering algorithms have been presented in literature [145]–[149]. These include the k-means [145], support-vector [146], singular value decomposition [147], self-organizing map [148], and spectral clustering algorithm [149]. Each clustering algorithm has its peculiarities. The k-means clustering is one of the simplest yet powerful algorithms that can be employed for clustering purposes.

The  $k$  – means clustering algorithm applies an unsupervised machine learning and splits a dataset of  $X = \{x_1, x_2, \dots, x_n\}$  into  $N^{cl}$  clusters  $C_i$  where  $i = 1, \dots, N^{cl}$  [150], [151]. The number of clusters,  $N^{cl}$ , is selected in the arbitrary manner. The clusters have to satisfy the criterions:

- The elements of one cluster cannot be the elements of another cluster:  $C_i \cap C_j = \emptyset$  for  $i \neq j$ ;
- The entire data of  $X$  has to be distributed among clusters:  $C_1 \cup C_2 \cup \dots \cup C_{N^{cl}} = X$ ;

Each cluster is characterized with a centroid  $\mu_i$  that represents the center of a cluster. To assign the element of a dataset to a cluster, the Euclidean distance between each element and each of  $N^{cl}$  centroids is measured. The element  $x_i$  is assigned to the cluster  $C_i$  if the Euclidean distance between  $x_i$  and  $\mu_i$  is smaller than the distance to other centroids. Graphically, the principle of clusters formation is shown in Figure 3.13.

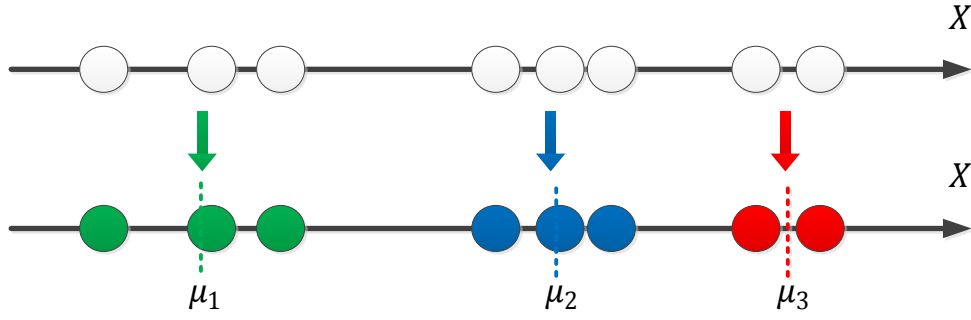


Figure 3.13. Clusters formation with indicated centroids

Thus, the problem of finding the right set of clusters can be formulated as the objective of finding the right centroids. This task can be achieved by minimizing the objective function:

$$E(N^{cl}) = \sum_{i=1}^{N^{cl}} \sum_{x_j \in C_i}^{m_i^{cl}} \|x_j - \mu_i\|^2 \quad (3.25)$$

where  $m_i^{cl} = |C_i|$  is the number of elements in a cluster  $C_i$ .

The calculation of  $E(N^{cl})$  includes inner and outer sum operations. The inner sum calculates the total Euclidean distance for each element in the cluster  $C_i$ , the outer sum adds the inner sum of each cluster together. The minimized  $E(N^{cl})$  is obtained when the sum of distances between cluster elements and cluster centroid is minimal.

The classical  $k$  – means clustering algorithm is performed in iterations. At the first iteration,  $t = 0$ , the initial set of centroids  $\mu_1^{(t)}, \mu_2^{(t)}, \dots, \mu_k^{(t)}$  is randomly generated. Then, the clusters are found where:

$$C_i^{(t)} = \{x_j \in X, \|x_j - \mu_i\|^2 \leq \|x_j - \mu_l\|^2 \forall l \neq i\} \quad (3.26)$$

After clusters are found, the algorithm re-computes the estimation of cluster centroids:

$$\mu_i^{(t+1)} = \frac{1}{m_i} \sum_{x_j \in C_i^t} x_j \quad (3.27)$$

Then, the iteration number increases,  $t = t + 1$ , and operations in Equations 3.26 – 3.27 are repeated. The iteration process terminates once the clusters stop changing or the iteration maximum,  $t_{max}$ , is reached.

The  $k$  – means clustering algorithm rapidly converges to a solution. However, it can converge to a local minimum. That is why the algorithm is run multiple times (for example 1000 times). Then, among the 1000 solutions, the solution with the smallest  $E(N^{cl})$  is selected.

The main code elements for the  $k$  – means clustering algorithm are presented in Figure 3.14.

---

```

t ← 0
done ← False
randomly initialize  $\mu_1^t, \mu_2^t, \dots, \mu_k^t$ 
while not done do
  // for each mean, update its cluster
  for i = 1 to k do
     $C_i^t = \{x \in X \mid \|x - \mu_i^t\| \leq \|x - \mu_j^t\|\}$ 

    if  $C_i^t \cap C_i^{t-1} = C_i^t \forall i$  then
      done ← True

  // for each cluster, update its mean
  for i = 1 to k do
     $n_i = |C_i^t|$ 
     $\mu_i^{t+1} = \frac{1}{n_i} \sum_{x \in C_i^t} x$ 

    if  $\|\mu_i^{t+1} - \mu_i^t\| \leq \epsilon \forall i$  then
      done ← True

  t ← t + 1
  if t > tmax then
    done ← True

end while

```

---

Figure 3.14. Main code elements for the  $k$  – means clustering algorithm [152]

### 3.3.2. Selection of the optimal number of clusters

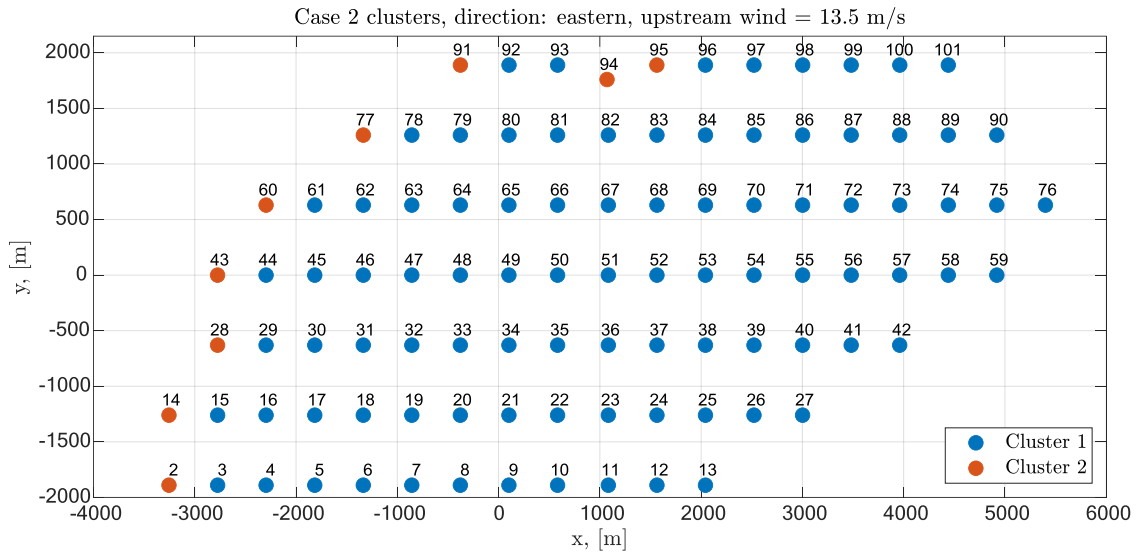
With the clustering algorithm described, the question is how to select the optimal number of clusters. In order to answer this question, the  $k$  – means clustering is applied to the case study WPP and an analysis based on the time-domain simulations is conducted. The  $k$  – means clustering is performed for 2, 3 and 4 clusters. The maximum number of clusters is chosen to be  $N_{max}^{cl} = 4$  clusters. Though more clusters can be considered, it will be shown further in this thesis that the selected maximum number of clusters is sufficient for the conducted studies. Three cases of the upstream wind speed are chosen:

- 1) medium-wind speed,  $v = 13.5$  m/s,
- 2) low-wind speed,  $v = 8$  m/s,
- 3) high-wind speed,  $v = 18$  m/s.

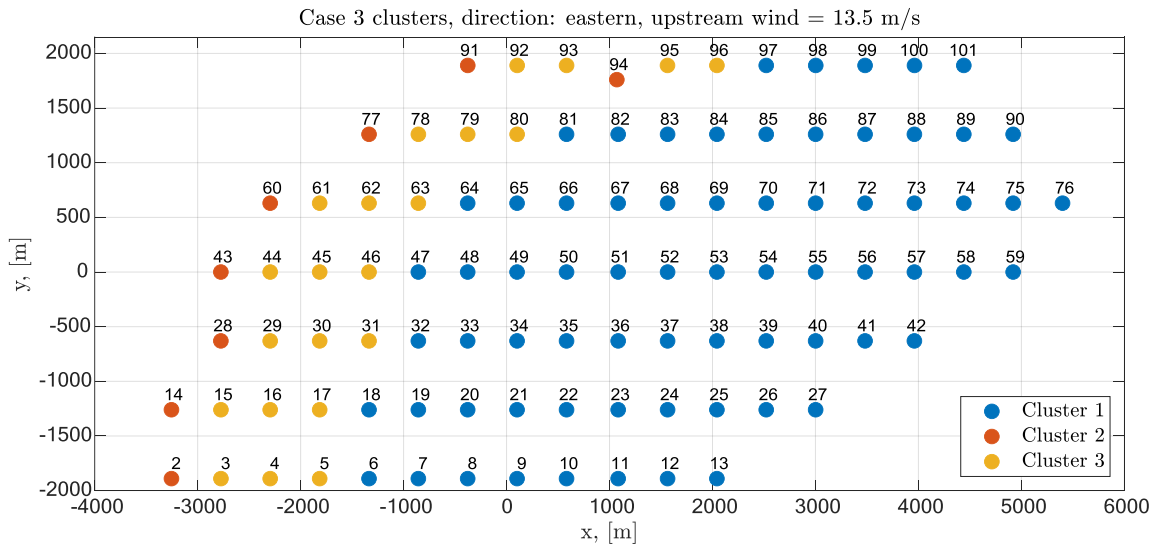
The wind has an east direction as shown in Figure 3.11. Based on insights into the working principles of the wind turbines at different wind speeds, there is an expected high likelihood that at both low- and high-wind speeds the wind turbines will operate similarly. In this case, the SMM is likely sufficient to represent the dynamics of the WPP model. However, at medium-wind speeds, it is certain that the wind turbines can operate differently. It is thus especially in these regions that the cluster-based MMM will be needed.

- Medium-wind speed,  $v = 13.5$  m/s

For the medium-wind speed, the average wind speed across a WPP is 11.1 m/s. To recall, the wind turbine rated wind speed is 12.05 m/s. The results of the  $k$  – means clustering are presented with the cluster distribution map in Figure 3.15.



a)



b)

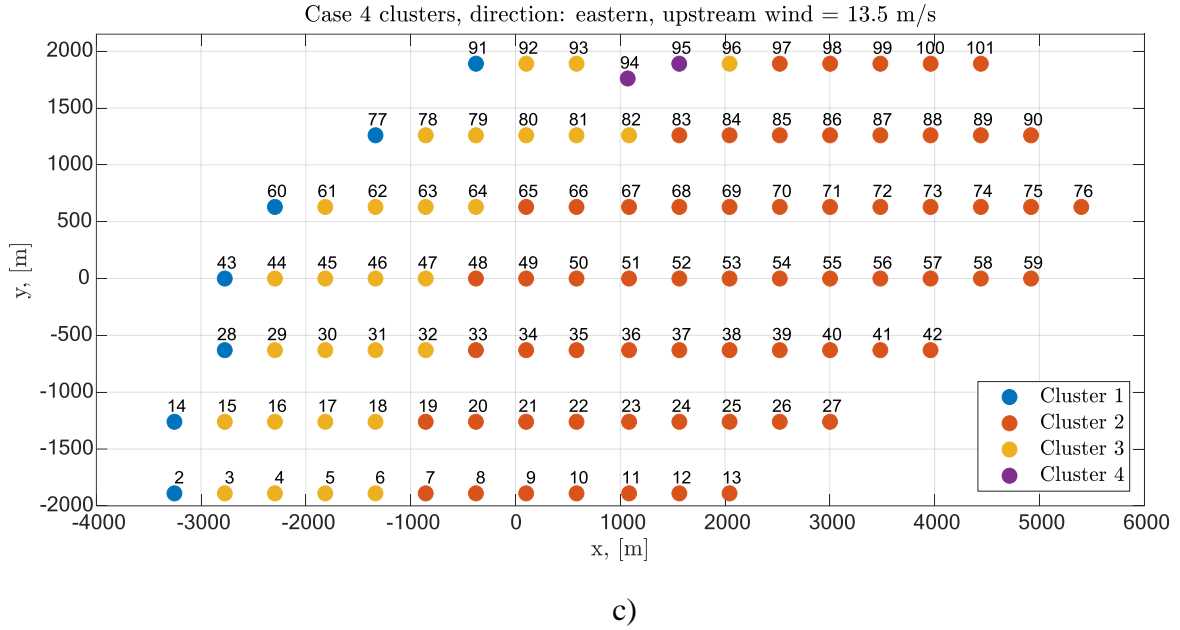


Figure 3.15. WPP map with highlighted clustering for a) 2 clusters, b) 3 clusters, c) 4 clusters

To demonstrate the dynamic response of the cluster-based MMM with different number of clusters as well as of the SMM and the detailed model, time-domain simulations are conducted. As the focus in this work is on the frequency contribution provided by grid-forming converters, the simulated disturbance is a grid frequency variation with a RoCoF = 2 Hz/s.

The performance of the DEMs is verified by comparing their responses to the response of the detailed WPP model. The index numerically characterizing the performance is the root-mean square percentage error (RMSPE) expressed as:

$$RMSPE = 100\% \sqrt{\frac{\sum_{i=1}^t (p_d(i) - p_{DEM}(i))^2}{t}} \quad (3.28)$$

where  $p_d$  is the timeseries data for the active power measured at the PCC from a detailed WPP model,  $p_{DEM}$  is the timeseries data for the active power measured at the PCC from a DEM,  $t$  is the number of datapoints in a dataset.

Under the selected wind speed, 48% of wind turbines switch to their current-limiting control mode during a disturbance. However, the current saturation happens at different time instants because each wind turbine has a different initial operating point and can also operate in different operating zones (power optimization, power limitation). For example, one wind turbine enters the current-limiting mode 100 ms after a grid disturbance, another only at 500 ms. Therefore, it is a non-trivial task for a DEM to combine the dynamic responses of the wind turbines operating in the normal mode and in the current-limited mode. Ideally, the wind turbines with similar wind speeds are thus to be assigned to the same cluster. As shown in Figure 3.16, the 3- and 4-cluster MMMs approximate the detailed model best.

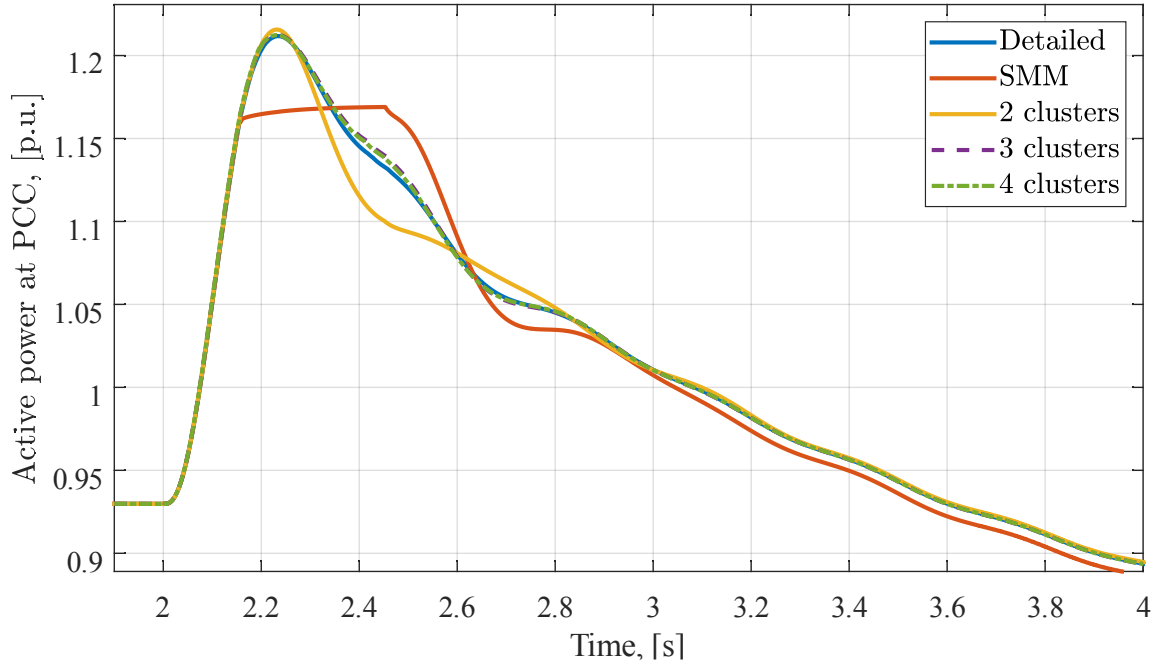


Figure 3.16. Eastern wind direction, upstream wind speed 13.5 m/s

The RMSPE for these simulation results is given in Table 3.7.

Table 3.7. RMSPE, direction: east, upstream wind speed: 13.5 m/s

DEM	RMSPE, %
SMM	1.98
MMM (2 CLST)	0.51
MMM (3 CLST)	0.11
<b>MMM (4 CLST)</b>	<b>0.09</b>

The results in Table 3.7 show notable accuracy improvement between the SMM and the 2-, 3-cluster MMM, while the improvement between 3- and 4-cluster MMM is smaller. Thus, for certain cases of medium wind speeds, the MMM with more clusters is more accurate. However, the further increase of the clusters number will have a smaller effect, according to this metric.

Hence, there should be a criterion to choose the DEM with the optimal number of clusters that would be sufficient for accurate following of the dynamic response of the detailed model. The criterion of selecting the optimal number of clusters is based on the RMSPE difference between the DEMs. The logic of selecting the optimal number can be written as follows:

$$\begin{aligned}
 & \text{for } k = 1: N^{cl} - 1 \\
 & \quad \Delta RMSPE = |RMSPE(k) - RMSPE(k + 1)| \\
 & \quad \text{if } \Delta RMSPE < \varepsilon: \text{optimal model} = k; \text{break}; \text{end} \\
 & \quad \text{if } k = N^{cl} - 1: \text{optimal model} = k + 1; \text{end} \\
 & \text{end}
 \end{aligned} \tag{3.29}$$

where initial  $k = 1$  corresponds to the SMM,  $k + 1 = 2$  – to the 2-cluster MMM, etc,  $\varepsilon$  is the minimal allowed error below which the DEM can be selected as optimal.

The value of  $\varepsilon$  can be arbitrarily selected. In this thesis it is chosen as  $\varepsilon = 0.02\%$ .

By applying this criterion to the results in Table 3.7, it can be deduced that the cluster-based MMM with 4 clusters is the most optimal among others.

- Low- and high-wind speed: 9 m/s, 18 m/s

As mentioned, the low- and high-wind speeds are considered because there is a high probability that the wind turbines under these wind conditions will operate similarly. Similar operation of each wind turbine in a WPP can have impact on the results of the DEMs.

The graphical demonstration of the cluster groups has been omitted for these cases. In Figure 3.17 the resulting dynamic responses of the detailed model and DEMs to the same grid disturbance are presented. The responses of all DEMs show a close resemblance to the detailed model. In Figure 3.17, (a), all wind turbines operate in the power optimization mode and the average wind speed is 8.1 m/s. In Figure 3.17, (b), all wind turbines produce rated power and switch to the current-limited mode more or less at the same time during the grid disturbance.

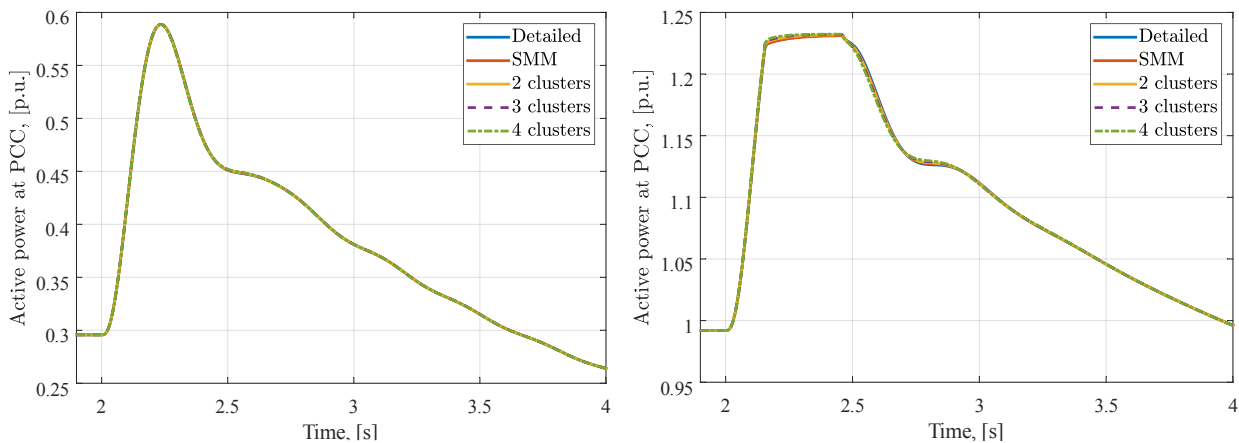


Figure 3.17. The active power response from detailed model and DEMs in the low- and high-wind speed regions, a) 9 m/s, b) 18 m/s

In Table 3.8 – Table 3.9 the RMSPEs for the discussed simulation results are provided.

Table 3.8. RMSPE, direction: east, upstream wind speed: 9 m/s

DEM	RMSPE, %
SMM	0.034
MMM (2 CLST)	0.014
MMM (3 CLST)	0.019
MMM (4 CLST)	0.025

Table 3.9. RMSPE, direction: east, upstream wind speed: 18 m/s

DEM	RMSPE, %
SMM	0.023
MMM (2 CLST)	0.016
MMM (3 CLST)	0.024
MMM (4 CLST)	0.027

Compared to the RMSPE in Table 3.7, the RMSPEs are several times smaller and the differences between the RMSPEs are very small. If a criterion for the optimal number of clusters is applied, then the number corresponding to the SMM will be selected as the optimal. Thus, the RMSPE results along with the time-domain results confirm the expected behavior outlined in the beginning of this section about the similarity of the dynamic characteristics of the DEMs in low- and high-wind speed regions.

### **3.4. Algorithm for determining the optimal number of clusters as a function of wind conditions**

In the previous section, it was demonstrated that the  $k$  – means clustering algorithm can help to significantly improve the accuracy of the DEM, especially in the cases when wind turbines behave differently. In addition, the selection of the optimal number of clusters was explained. In this section, the generalized algorithm which determines the optimal number of clusters as a function of wind conditions is proposed. In order to describe the principles behind the algorithm, we conduct a sweep for one wind direction and several wind speeds and determine the optimal number of clusters for each case.

### 3.4.1. Selection of the optimal number of clusters for one wind direction

The wind speed sweep is performed in the range of 8 – 20 m/s for the east wind direction. The time-domain simulations of the detailed model and DEMs are conducted for the same grid disturbance.

The upstream winds are:

8.0, 9.0, 10.0, 11.0, 11.5, 12, 12.5, 13.0, 13.5, 14, 14.5, 15, 15.5, 16, 18, 20 m/s.

The RMSPE evolution based on the time-domain simulation results is presented in Figure 3.18. In the region with medium wind speeds (12 – 14 m/s), the cluster-based MMM clearly outperforms the SMM. Especially, the 4-cluster MMM results in a notable accuracy increase, in particular in this wind speed region. In the region of low- (8 – 11.5 m/s) and high-wind speeds (14.5 – 20 m/s) the RMSPEs of all DEMs are very small and their differences are negligible.

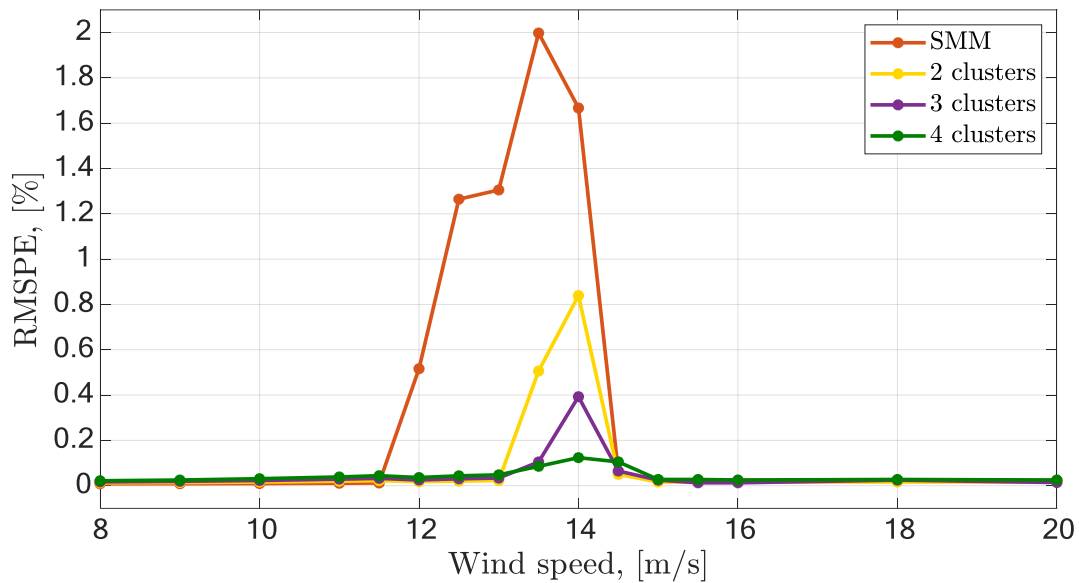


Figure 3.18. RMSPE for eastern wind direction

The selection of the optimal number of clusters is performed according to Equation 3.30 with  $\varepsilon = 0.02\%$ . The results of selection are provided in Figure 3.19. According to these results, in the medium-wind speed region the cluster-based MMM with 4 clusters is selected as optimal as it has the best accuracy among the DEMs. The number of clusters can be also further increased. However, as confirmed by simulation results in Figure 3.16, the 4-cluster MMM provides very good accuracy in the medium wind speed region and the increase of clusters number will only bring a marginal improvement. It is also logical that it will increase the computation time. On the contrary, in the low- and high-wind speed regions the SMM that is the 1-cluster MMM is selected because the  $\Delta RMSPE$  between the DEMs is very small.

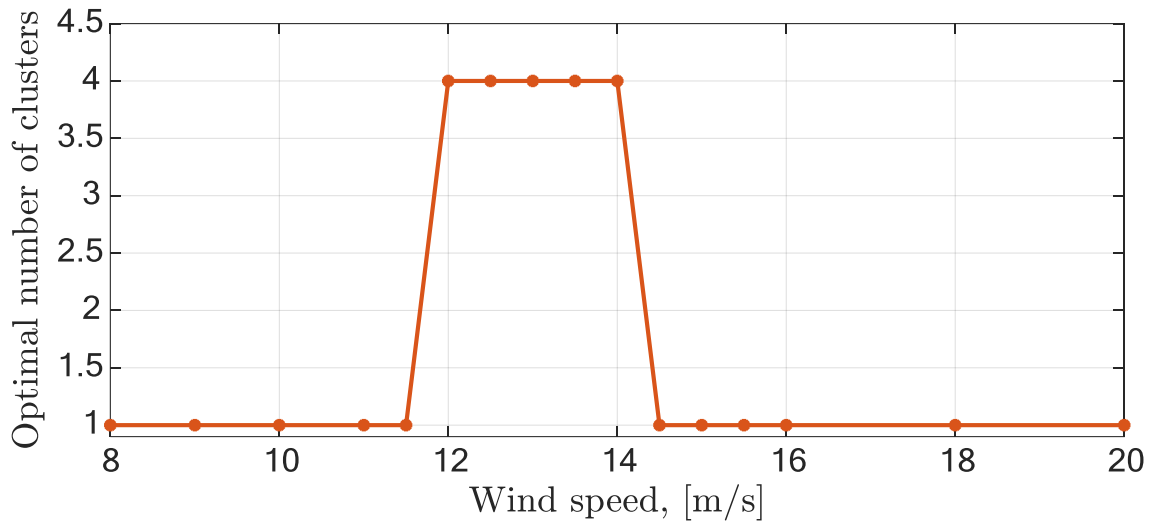


Figure 3.19. Optimal number of clusters for one wind direction

### 3.4.2. Generalization of the algorithm

The algorithm determining the optimal number of clusters can be generalized in the following steps:

- Step 1. The topology of the collector network, the maximal number of clusters,  $N_{max}^{cl}$ , the number of wind directions,  $\mathbf{m}$ , and the number of wind speeds,  $\mathbf{n}$ , in each wind direction, are chosen.
- Step 2. For each  $\mathbf{n}$  and  $\mathbf{m}$ , the wind turbines are grouped in clusters and the equivalent impedances of cluster-based MMMs as well as of the SMM are calculated.
- Step 3. The WPP detailed and DEMs are initialized according to the wind speeds. and simulated. The measurements for the active power at the PCC are saved.
- Step 4. After a simulation, the optimal number of clusters for a specific wind condition is determined.
- Step 5. Once  $\mathbf{m} = \mathbf{m}_{max}$ , the results of the optimal number of clusters are graphically presented with a multi-segment round plot.

The steps of this generalized algorithm are depicted in Figure 3.20.

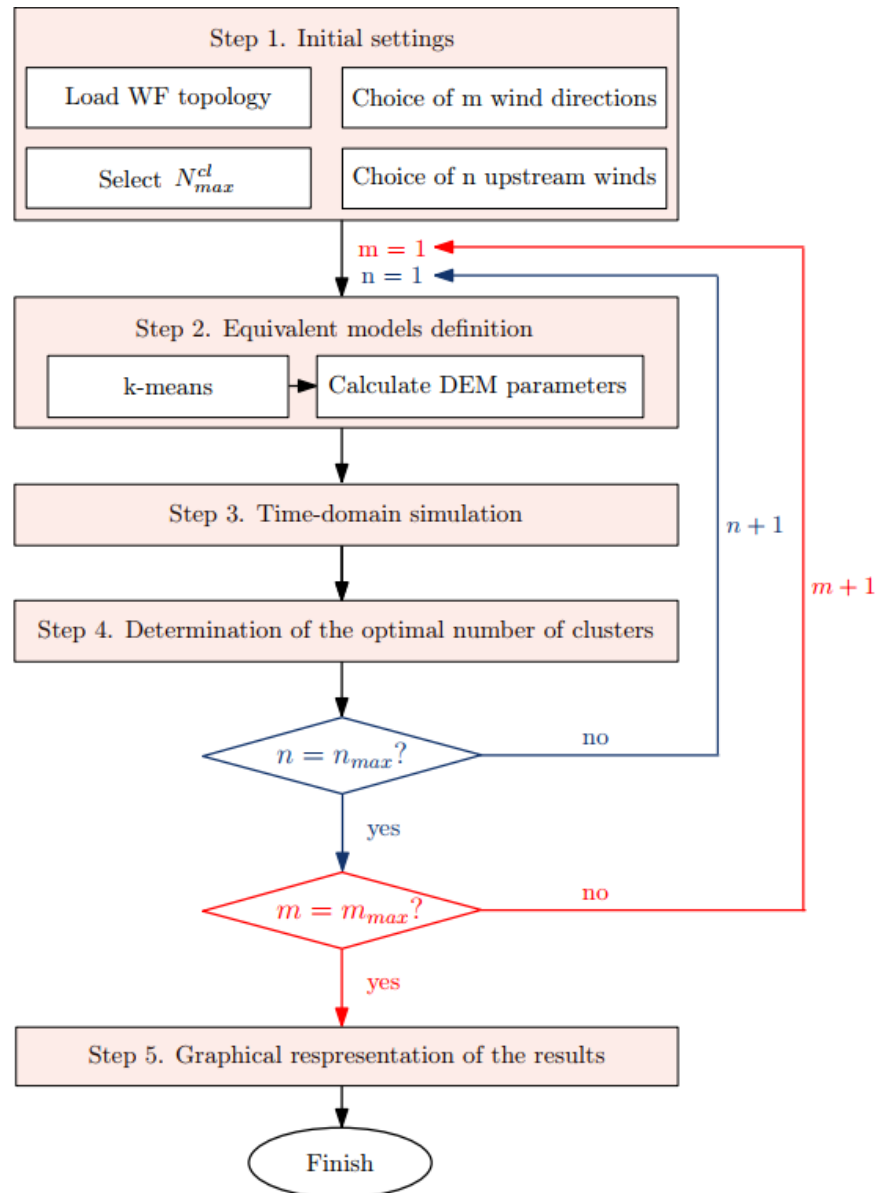


Figure 3.20. Generalized algorithm for determination of the optimal number of clusters

### 3.4.3. Algorithm verification for all wind directions and wind speeds

To verify the proposed algorithm, a complete sweep of wind directions and upstream wind speeds for the case study WPP is carried out.

The wind directions are swept from  $0^\circ$  to  $345^\circ$  with a step of  $15^\circ$  ( $m_{max} = 24$ ).

Upstream winds: 8.0, 9.0, 10.0, 11.0, 11.5, 12, 12.5, 13.0, 13.5, 14, 14.5, 15, 15.5, 16, 18, 20 m/s ( $n_{max} = 16$ ).

The algorithm is launched for several grid disturbances: RoCoF = 2 Hz/s, 2.5 Hz/s and 3 Hz/s. The RoCoF = 3 Hz/s is assumed to be the maximum value that can be expected to happen in the power system [153].

For each case, the performance of the SMM and cluster-based MMM with 2, 3, 4 clusters is compared.

- $\text{RoCoF} = 2 \text{ Hz/s}$

The results are presented in the form of a multi-segment round plot in Figure 3.21. This round depicts the optimal number of clusters to be used in a considered wind condition (cell). There are two colors on the plot: white and green. White is for the SMM and green corresponds to the MMM with 4 clusters. The optimal number of clusters resulted to be always equal to four because this DEM gives the smallest RMSPE and satisfies the error criterion set for the choice of the optimal number of clusters. According to the obtained results, the SMM is recommended to use in the low- and high-wind speed regions. The use of the cluster-based MMM is preferred in the medium-wind speed region.

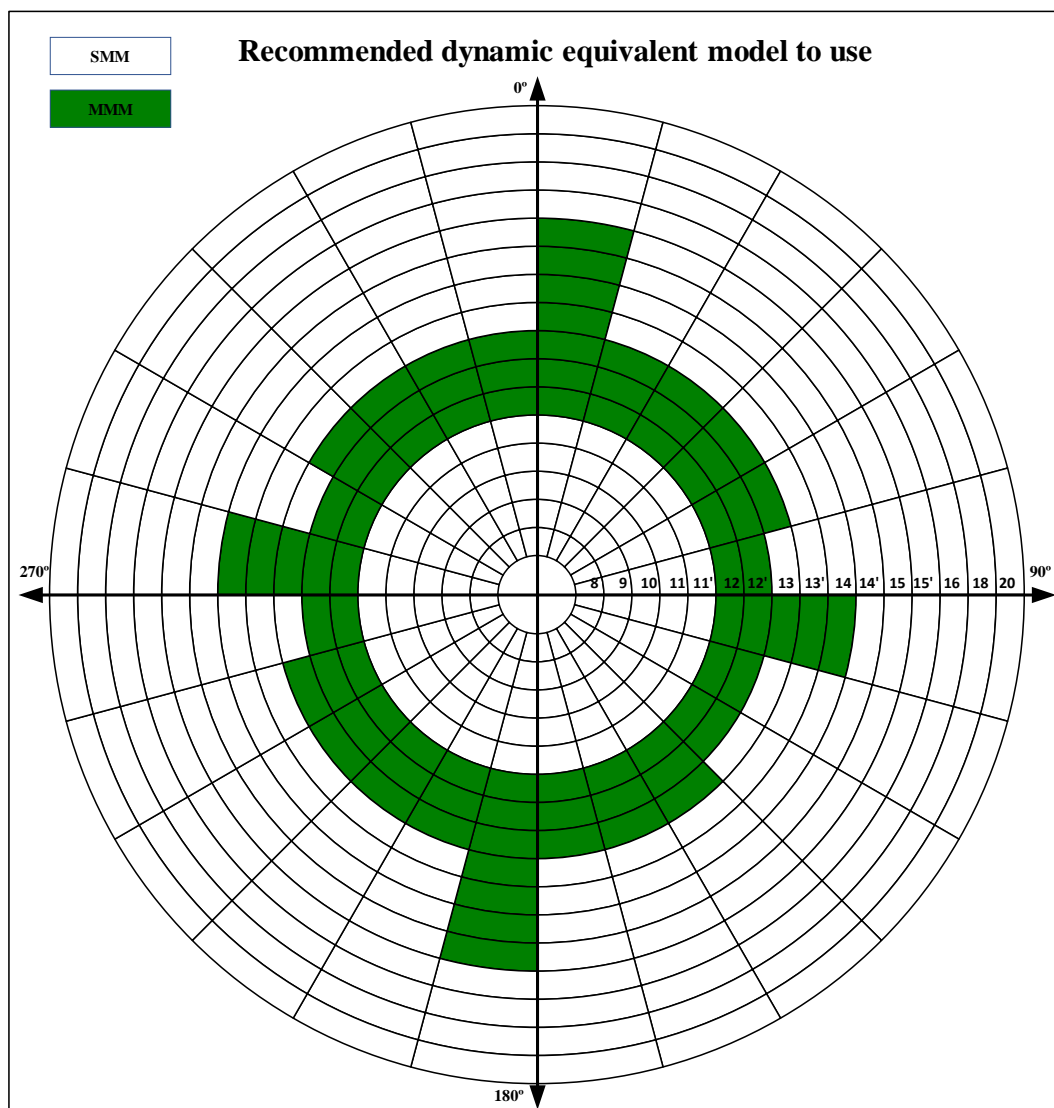


Figure 3.21. Multi-segment round plot for  $\text{RoCoF} = 2 \text{ Hz/s}$

The size of the zone where the use of the cluster-based MMM is recommended also depends on the severity of a disturbance in the grid.

- 2.5 Hz/s, 3 Hz/s

The results are presented in Figure 3.22 and Figure 3.23, respectively. Similarly to  $\text{RoCoF} = 2 \text{ Hz/s}$ , in the medium-wind speed region, the cluster-based MMM with 4 clusters is recommended. With the increased size of the grid disturbance, there are more wind turbines switching to the current-limited mode. Thus, the extent of dissimilarity between the wind turbines increases, especially for the case of  $3 \text{ Hz/s}$ , Figure 3.23. Thus it becomes the preferred option to represent a WPP with the cluster-based MMM in a wider range of wind conditions. For instance, green zone for the case of  $\text{RoCoF} = 2 \text{ Hz/s}$  and  $2.5 \text{ Hz/s}$  starts at  $12 \text{ m/s}$ , while for the case of  $\text{RoCoF} = 3 \text{ Hz/s}$  it starts at  $11.5 \text{ m/s}$ .

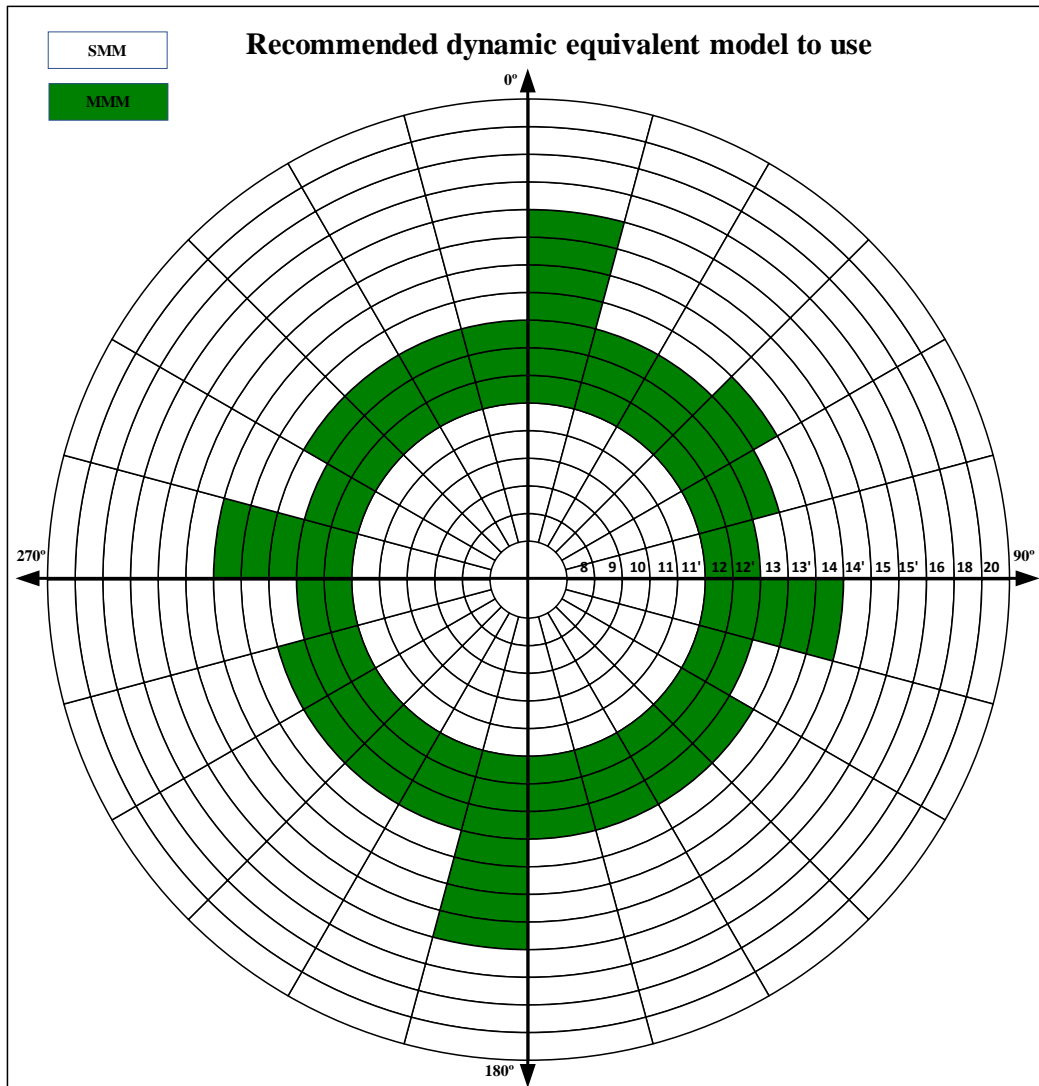


Figure 3.22. Multi-segment round plot for  $\text{RoCoF} = 2.5 \text{ Hz/s}$

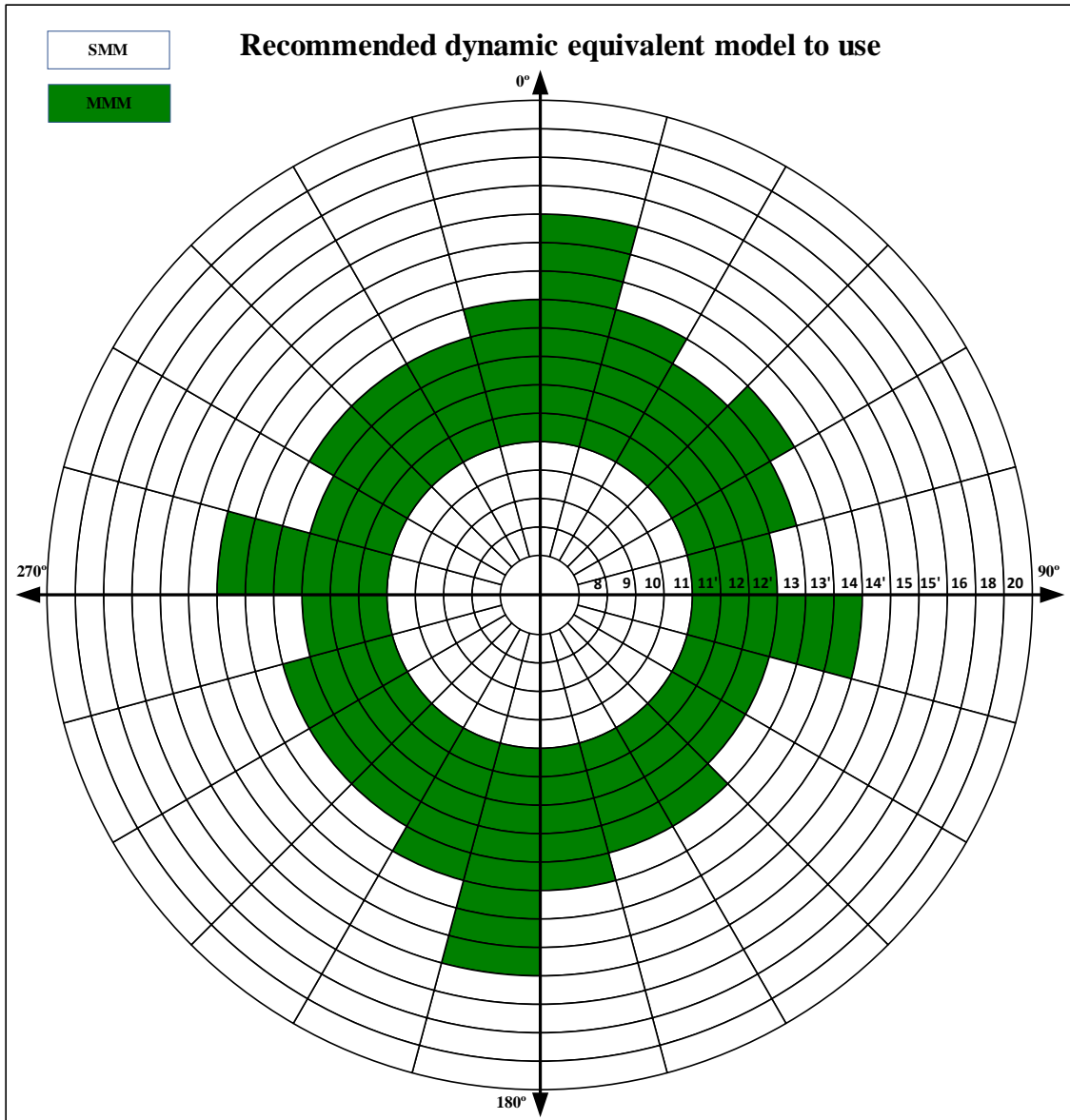


Figure 3.23 . Multi-segment round plot for RoCoF = 3 Hz/s

Considering the multi-segment round plots, it is clear that the recommendations given based on the RoCoF = 2 Hz/s remain relevant for RoCoF = 2.5 Hz/s and RoCoF = 3 Hz/s. Therefore, the multi-segment round plot of RoCoF = 3 Hz/s is also valid for RoCoF = 2 Hz/s. Hence, the algorithm recommendations can be merged into one universal multi-segment round plot shown in Figure 3.24 where green, purple and orange colors correspond to the recommendations added from results for RoCoFs = 2, 2.5 and 3 Hz/s, respectively.

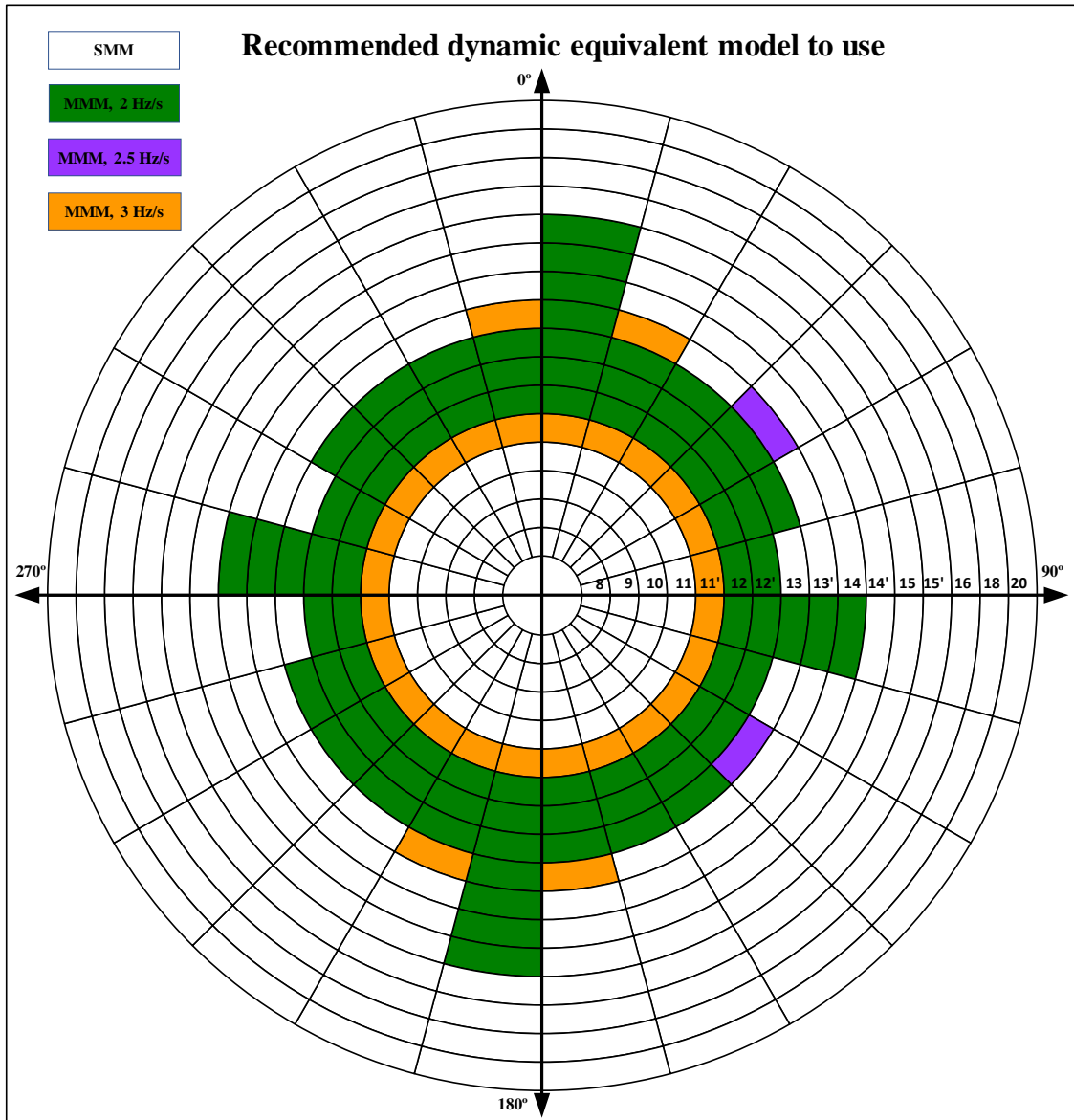


Figure 3.24. Universal multi-segment round plot

By recalling the criterion used for the selection of the optimal number of clusters, it is true that in the case when the SMM is recommended, the cluster-based MMM does not perform worse. Therefore, the recommendations in the universal multi-segment round plot can be simplified by extending the cluster-based MMM zone until the maximum upstream wind speed where the cluster-based MMM is recommended.

The results of zone extension are provided in Figure 3.25 where the maximum upstream wind speed for the cluster-based MMM is 15 m/s.

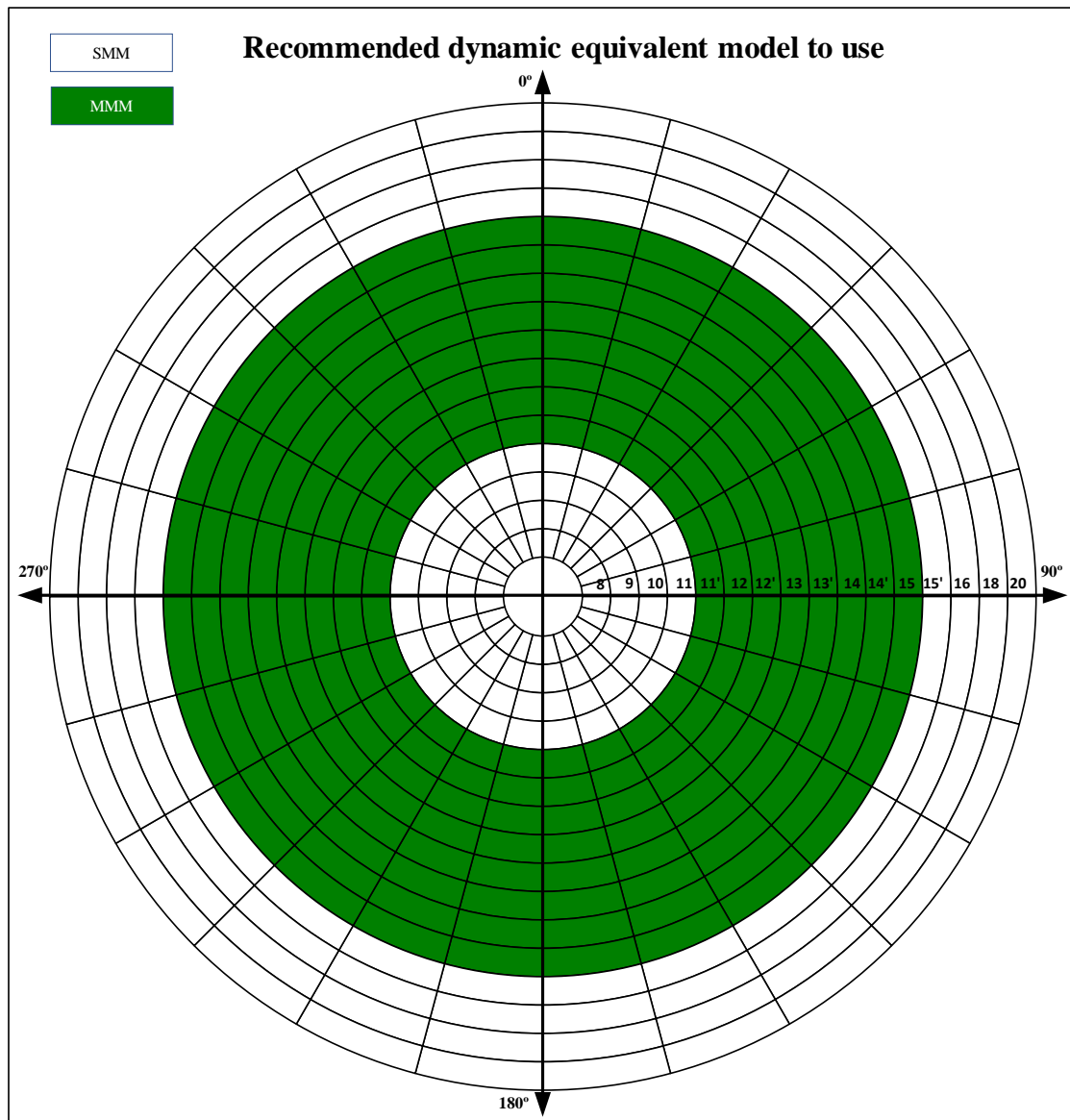


Figure 3.25 . Universal multi-segment round plot with extended zone for the cluster-based MMM

## Conclusions

In this chapter the aggregation of a grid-forming WPP has been investigated. Several types of DEMs and their derivation were presented. In order to include realistic wind conditions across a WPP, a state-of-the-art wind model taking the heterogeneous wind distribution into account has been implemented. The wind distribution model along with the  $k$  – means clustering allowed obtaining cluster-based MMMs capable of accurately reflecting the dynamic characteristics of the detailed WPP model. The criterion for the selection of the optimal number of clusters in the cluster-based MMM was explained. It was demonstrated that for specific wind conditions, especially for low- and high-wind speeds, the classical SMM is typically sufficient for representing the dynamics of the detailed WPP model, while for the medium-wind speeds, the cluster-based MMM becomes indispensable. Furthermore, in order to provide information about the DEM that is optimal to use in one or another wind condition, a generalized algorithm for determining the optimal number of clusters as a function of wind conditions was proposed. The performance of the proposed algorithm was demonstrated by applying it to a case study WPP. The outcomes of applying the algorithm are summarized by means of universal multi-segment round plots, which graphically present the recommendations of the most suitable DEM for different wind speed conditions.

## General conclusion

Wind turbines make a significant contribution towards the energy transition. The control of these wind turbines in the power system, which undergoes substantial transformation as a result of the energy transition, requires special attention. In particular, how to switch from grid-following to grid-forming operation mode, as well as how to accurately represent the grid-forming WPP connected to a transmission system with a dynamic equivalent model are important scientific questions to be investigated. The main focus of this thesis has been on the grid-forming control applied to a Type-IV wind turbine. The objectives were to study how the grid-forming control can be integrated into the control configuration of the B2B converter and what the issues are that can arise due to this integration. These issues were identified and solutions to mitigate the problems were proposed. Also, another objective was to study the possibility of aggregating a WPP that includes numerous grid-forming wind turbines so that it becomes possible to conduct a dynamic analysis of the transmission system with integrated grid-forming WPPs. The main conclusions are summarized in the remainder of this chapter.

In the first chapter, the modelling fundamentals for the power electronic converter control as well as the main wind turbine components have been presented. Moreover, the chapter was concentrated on the integration of the grid-forming control in the control configuration of the B2B converter of a Type-IV wind turbine. For this reason, the classical grid-following control configuration for a wind turbine was recalled. It has been found that the combination of the classical control of the B2B converter with a grid-forming control is not feasible since this control configuration is prone to instabilities due to poor regulation of the DC bus voltage. It is because the GSC has to simultaneously perform two control actions such as the regulation of the power transfer and the control of the DC bus voltage. The latter has to be relatively slow to avoid interference with the grid-forming controller. It was explained that, in order to improve the DC bus voltage regulation, the controls of the MSC and the GSC have to be switched. So, a modified control strategy, called as *p – control strategy*, stipulates that the MSC is responsible for the DC bus voltage control and the GSC is responsible for the power transfer to the PCC. It was identified that apart from the visible benefits of the *p – control strategy*, it creates electromechanical couplings between the dynamics of the wind turbine and the dynamics of the grid-forming control. These couplings can negatively impact the performance of a grid-forming wind turbine and, thus, are thoroughly investigated in the second chapter.

In the second chapter the electromechanical couplings between the wind turbine dynamics and the dynamics of the grid-forming control have been studied closely and possible solutions for their mitigation have been discussed and proposed. The main reason of the existence of these couplings in a grid-forming wind turbine is the modified control configuration of the B2B converter. The main focus was on the coupling created by the DC bus voltage controller located at the MSC. Since the grid-forming control with inherent inertia capability reacts instantaneously to grid disturbances, the DC bus voltage controller also has a rapid reaction with the aim to restore the power balance at the DC side. This rapid reaction leads to the fast variation of the wind turbine generator' electromagnetic torque. Hence, the grid-forming control has an indirect impact on the wind turbine generator and on the mechanical structure of a wind turbine. Thus, a grid-forming wind turbine is linked to the grid and all grid disturbances are translated to the mechanical structure of a wind turbine. The fast variation of the electromagnetic torque induces drivetrain torsional

vibrations which propagate to the DC and AC side. These vibrations increase stresses on the mechanical structure and lead to fatigue and lifetime reduction of the wind turbine components. The damping of torsional vibrations has been performed with the input shaping method implemented with a ZV filter. The proposed damping has shown positive improvement in terms of mitigation of torsional vibrations. It was found that the considered damping solution, however, can have a negative effect on the DC bus voltage dynamics. Therefore, solutions to minimize this effect were proposed. It has been justified that these solutions can help to mitigate and limit the DC bus voltage variations while ensuring sufficient efficiency of vibration damping. Furthermore, the robustness of the ZV filter has been tested by applying the variation of the drivetrain parameters and considering the possibility that the drivetrain oscillatory modes are estimated with an error. It has been confirmed that the applied damping is efficient against torsional vibrations even if there are some parametric uncertainties.

Furthermore, the effectiveness of the proposed damping method will not be deteriorated by variation in grid inertia, grid strength and wind speed. Indeed, such variations do not change the characteristics of the drivetrain oscillatory modes and thus, the efficiency of the damping based on the IS method will not be affected. In addition, a high level of detail for the grid model is not critical for the robustness tests of the proposed damping.

Moreover, with the additional improvements listed in the future perspectives, the proposed damping method has the potential to be used in industry when applied to existing wind turbines and the ones in design stage.

In the third chapter the possibility to aggregate a grid-forming WPP into a DEM has been studied. Assuming that the wind is heterogeneously distributed across a WPP, the aggregation process aimed to derive the most accurate DEM requires multiple steps to be done. These include:

- modelling of the wind distribution;
- grouping of the wind turbines into clusters with the  $k$  – means clustering algorithm;
- derivation of the DEMs including the cluster-based MMMs with different number of clusters;
- selection of the optimal number of clusters that satisfy the criterion of the model accuracy.

The results of aggregation have shown that the use of the cluster-based MMM with the multiple number of clusters is the optimal option for the medium winds speeds. It is because under such wind conditions, the wind turbines in a WPP are more likely to differently react to grid disturbances. Meanwhile, for the low and high wind speeds, the SMM already renders sufficient accuracy, and the use of a sophisticated cluster-based MMM is redundant. To know what the optimal DEM is to be used in certain wind conditions, the steps required for the aggregation process are generalized in the algorithm that determines the optimal number of clusters as a function of wind conditions. The algorithm scans all wind directions and upstream wind speeds in each direction and, as the outcome, provides the recommendations of the optimal DEM for each wind condition. The recommendations of an optimal DEM as well as its equivalent parameters for each wind condition should be transmitted to the TSO by a WPP operator. Knowing the upstream wind speed and wind direction, the TSO can use a corresponding optimal DEM. These optimal DEMs can be useful for a TSO in the analysis of the interconnection feasibility of a grid-forming WPP to the transmission system and in the system-wide dynamic studies.

## Future perspectives

The future works provisioned from the outcomes of this thesis can be arranged in two groups corresponding to Chapter 2 and Chapter 3.

Based on the results in Chapter 2, the following work pathways can be underlaid:

- The proposed vibrations damping with the input shaping method can be improved in terms of the control by using a more adaptive algorithm that dynamically re-tunes the ZV filter according to the changing dynamic characteristics of the wind turbine' drivetrain. For example, this can be achieved with a model predictive controller integrated into the damping control, so that the variation of the drivetrain oscillatory modes can be anticipated and the ZV filter parameters can be re-calculated dynamically. Moreover, it has been demonstrated that the implementation of the vibration damping can be constrained due to significant variations of the DC bus voltage. Therefore, it is worth paying attention to define how the impact of these constraints on the damping efficiency can be alleviated and optimized by advanced control actions.
- Moreover, in this thesis, the wind turbine model is a simplified model and does not take into account the dynamics of other mechanical components of the wind turbine such as the nacelle and the yaw regulation system. Therefore, the proposed damping solution has to be verified for a more sophisticated model of a wind turbine;
- It is also possible to shift the DC bus voltage regulation from the MSC to an added storage device at the DC link, which is a solution that is currently being pursued by wind turbine manufacturers. A storage device allows avoiding the interference with the damping controller. Hence, the DC bus voltage dynamics can be improved. Since the storage device brings additional costs compared to the developed control solution, the two solutions should be analyzed in detail. From this analysis, the optimal dimensions for the storage can be derived, possibly combining the storage solution with the proposed control.

Based on the results in Chapter 3, the following works are proposed:

- The developed algorithm determining the optimal dynamic equivalent model of a WPP under different wind conditions was subjected to the grid disturbances such as the grid frequency variations with different RoCoF values. So, the recommendations of the optimal dynamic equivalent models are based on this grid disturbance. A WPP can also be subjected to other grid disturbances such as phase shifts or voltage sags. Hence, it is important to try to upgrade the proposed recommendation algorithm so that the universal multi-segment round plot is valid for different types of grid disturbances being assessed;
- A stopping criterion of the proposed algorithm can be improved by using other metrics in order to correctly decide whether the accuracy of a selected DEM is sufficient for the dynamic studies under consideration;
- Another clustering method could be used with the proposed aggregation methodology and the results can be compared with the k – means clustering in terms of DEM accuracy;
- Moreover, the mix of the grid-following and the grid-forming wind turbines is a very interesting subject. Assuming that this topic will continue gaining relevance over the next

years, the aggregation of a WPP containing both the grid-following and the grid-forming wind turbines, or even different types of a grid-forming control, and the use of the proposed recommendation algorithm for the mixed WPPs can be further investigated in detail.

## References

- [1] International Energy Agency, “Global Energy Review: CO<sub>2</sub> Emissions in 2021 Global emissions rebound sharply to highest ever level,” 2021. Accessed: Sep. 03, 2022. [Online]. Available: [www.iea.org/t&c/](http://www.iea.org/t&c/).
- [2] “United Nations Climate Change, Adoption of the Paris agreement,” 2016. .
- [3] “European Commission, A European Green Deal.” [https://ec.europa.eu/info/strategy/priorities-2019-2024/european-green-deal\\_en](https://ec.europa.eu/info/strategy/priorities-2019-2024/european-green-deal_en) (accessed Sep. 17, 2022).
- [4] “EU Emissions Trading System (EU ETS).” [https://ec.europa.eu/clima/eu-action/eu-emissions-trading-system-eu-ets\\_en](https://ec.europa.eu/clima/eu-action/eu-emissions-trading-system-eu-ets_en) (accessed Sep. 17, 2022).
- [5] J. Rocabert, A. Luna, F. Blaabjerg, and P. Rodríguez, “Control of power converters in AC microgrids,” *IEEE Transactions on Power Electronics*, vol. 27, no. 11, pp. 4734–4749, 2012.
- [6] J. M. Guerrero, M. Chandorkar, T. L. Lee, and P. C. Loh, “Advanced control architectures for intelligent microgrids part i: Decentralized and hierarchical control,” *IEEE Transactions on Industrial Electronics*, vol. 60, no. 4, pp. 1254–1262, 2013.
- [7] D. E. Olivares, A. Mehrizi-Sani, A. H. Etemadi, C. A. Cañizares, R. Iravani, M. Kazerani, A. H. Hajimiragha, O. Gomis-Bellmunt, M. Saeedifard, R. Palma-Behnke, G. A. Jiménez-Estévez, and N. D. Hatziargyriou, “Trends in microgrid control,” *IEEE Transactions on Smart Grid*, vol. 5, no. 4, pp. 1905–1919, 2014.
- [8] F. Milano, F. Dorfler, G. Hug, D. J. Hill, and G. Verbič, “Foundations and challenges of low-inertia systems (Invited Paper),” *20th Power Systems Computation Conference, PSCC 2018*, Aug. 2018.
- [9] M. Paolone, T. Gaunt, X. Guillaud, M. Liserre, S. Meliopoulos, A. Monti, T. Van Cutsem, V. Vittal, and C. Vournas, “Fundamentals of power systems modelling in the presence of converter-interfaced generation,” *Electric Power Systems Research*, vol. 189, p. 106811, Dec. 2020.
- [10] T. Qoria, F. Gruson, F. Colas, X. Guillaud, M. S. Debry, and T. Prevoist, “Tuning of cascaded controllers for robust grid-forming voltage source converter,” *20th Power Systems Computation Conference, PSCC 2018*, Aug. 2018.
- [11] M. C. Chandorkar, D. M. Divan, and R. Adapa, “Control of parallel connected inverters in standalone ac supply systems,” *IEEE Transactions on Industry Applications*, vol. 29, no. 1, pp. 136–143, 1993.
- [12] J. W. Simpson-Porco, F. Dörfler, and F. Bullo, “Synchronization and power sharing for droop-controlled inverters in islanded microgrids,” *Automatica*, vol. 49, no. 9, pp. 2603–2611, Sep. 2013.
- [13] B. Johnson, M. Rodriguez, M. Sinha, and S. Dhople, “Comparison of virtual oscillator and droop control,” *2017 IEEE 18th Workshop on Control and Modeling for Power Electronics, COMPEL 2017*, Aug. 2017.
- [14] S. D’Arco, J. A. Suul, and O. B. Fosso, “A Virtual Synchronous Machine implementation for distributed control of power converters in SmartGrids,” *Electric Power Systems Research*, vol. 122, pp. 180–197, May 2015.
- [15] J. Roldan-Perez, A. Rodriguez-Cabero, and M. Prodanovic, “Design and Analysis of Virtual

- Synchronous Machines in Inductive and Resistive Weak Grids,” *IEEE Transactions on Energy Conversion*, vol. 34, no. 4, pp. 1818–1828, Dec. 2019.
- [16] H. Bevrani, T. Ise, and Y. Miura, “Virtual synchronous generators: A survey and new perspectives,” *International Journal of Electrical Power & Energy Systems*, vol. 54, pp. 244–254, Jan. 2014.
- [17] Q. C. Zhong and G. Weiss, “Synchronverters: Inverters that mimic synchronous generators,” *IEEE Transactions on Industrial Electronics*, vol. 58, no. 4, pp. 1259–1267, Apr. 2011.
- [18] L. Zhang, L. Harnefors, and H. P. Nee, “Power-synchronization control of grid-connected voltage-source converters,” *IEEE Transactions on Power Systems*, vol. 25, no. 2, pp. 809–820, May 2010.
- [19] I. Cvetkovic, D. Boroyevich, R. Burgos, C. Li, and P. Mattavelli, “Modeling and control of grid-connected voltage-source converters emulating isotropic and anisotropic synchronous machines,” *2015 IEEE 16th Workshop on Control and Modeling for Power Electronics, COMPEL 2015*, Sep. 2015.
- [20] C. Arghir, T. Jouini, and F. Dörfler, “Grid-forming control for power converters based on matching of synchronous machines,” *Automatica*, vol. 95, pp. 273–282, Sep. 2018.
- [21] S. Curi, D. Gros, and F. Dorfler, “Control of low-inertia power grids: A model reduction approach,” *2017 IEEE 56th Annual Conference on Decision and Control, CDC 2017*, vol. 2018-Janua, pp. 5708–5713, Jan. 2018.
- [22] C. Arghir and F. Dörfler, “The Electronic Realization of Synchronous Machines: Model Matching, Angle Tracking, and Energy Shaping Techniques,” *IEEE Transactions on Power Electronics*, vol. 35, no. 4, pp. 4398–4410, Apr. 2020.
- [23] “Migrate project.” <https://www.h2020-migrate.eu/> (accessed Sep. 03, 2022).
- [24] “PROMOTioN project.” <https://www.promotion-offshore.net/> (accessed Sep. 03, 2022).
- [25] “OSMOSE project.” <https://www.osmose-h2020.eu/> (accessed Sep. 03, 2022).
- [26] “TotalControl project.” <https://www.totalcontrolproject.eu/dissemination-activities/public-deliverables> (accessed Sep. 03, 2022).
- [27] R. Musca, A. Vasile, and G. Zizzo, “Grid-forming converters. A critical review of pilot projects and demonstrators,” *Renewable and Sustainable Energy Reviews*, vol. 165, p. 112551, Sep. 2022.
- [28] WindEnergy, “Wind energy in Europe: Scenarios for 2030,” 2017.
- [29] C. Guidorzi, S. Dichiara, F. Frontera, al -, Y. Shen, Z. Song, A. Kusiak -, Y. Zhou, A. Chechkin, I. M. Sokolov, L. Lu, and N. A. Cutululis, “Virtual synchronous machine control for wind turbines: a review,” *Journal of Physics: Conference Series*, vol. 1356, no. 1, p. 012028, Oct. 2019.
- [30] L. Shang, J. Hu, X. Yuan, and Y. Chi, “Understanding Inertial Response of Variable-Speed Wind Turbines by Defined Internal Potential Vector,” *Energies 2017, Vol. 10, Page 22*, vol. 10, no. 1, p. 22, Dec. 2016.
- [31] Y. Zhao, J. Chai, and X. Sun, “Virtual synchronous control of grid-connected DFIG-based wind turbines,” *Conference Proceedings - IEEE Applied Power Electronics Conference and Exposition - APEC*, vol. 2015-May, no. May, pp. 2980–2983, May 2015.
- [32] S. Wang, J. Hu, and X. Yuan, “Virtual Synchronous Control for Grid-Connected DFIG-Based Wind Turbines,” *IEEE Journal of Emerging and Selected Topics in Power*

*Electronics*, vol. 3, no. 4, pp. 932–944, Dec. 2015.

- [33] K. Gunther and C. Sourkounis, “Investigation of Virtual Synchronous Machine Control for the Grid-Side Converter of Wind Turbines with Permanently Excited Synchronous Generator,” *IECON Proceedings (Industrial Electronics Conference)*, vol. 2019-October, pp. 2395–2401, Oct. 2019.
- [34] D. Duckwitz, “Power System Inertia. Derivation of Requirements and Comparison of Inertia Emulation Methods for Converter-based Power Plants,” Fraunhofer Institute for Energy Economics and Energy System Technology, 2019.
- [35] L. Huang, H. Xin, Z. Wang, K. Wu, H. Wang, J. Hu, and C. Lu, “A Virtual Synchronous Control for Voltage-Source Converters Utilizing Dynamics of DC-Link Capacitor to Realize Self-Synchronization,” *IEEE Journal of Emerging and Selected Topics in Power Electronics*, vol. 5, no. 4, pp. 1565–1577, Dec. 2017.
- [36] S. Sang, C. Zhang, X. Cai, M. Molinas, J. Zhang, and F. Rao, “Control of a Type-IV Wind Turbine with the Capability of Robust Grid-Synchronization and Inertial Response for Weak Grid Stable Operation,” *IEEE Access*, vol. 7, pp. 58553–58569, 2019.
- [37] A. Jain, J. N. Sakamuri, and N. A. Cutululis, “Grid-forming control strategies for black start by offshore wind power plants,” *Wind Energy Science*, vol. 5, no. 4, pp. 1297–1313, Oct. 2020.
- [38] J. N. Sakamuri, Ö. Göksu, A. Bidadfar, O. Saborío-Romano, A. Jain, and N. A. Cutululis, “Black Start by HVdc-connected Offshore Wind Power Plants,” *IECON Proceedings (Industrial Electronics Conference)*, vol. 2019-October, pp. 7045–7050, Oct. 2019.
- [39] A. Jain, O. Saborío-Romano, J. N. Sakamuri, and N. A. Cutululis, “Virtual Resistance Control for Sequential Green-start of Offshore Wind Power Plants,” *IEEE Transactions on Sustainable Energy*, Jul. 2022.
- [40] A. Jain, O. Saborío-Romano, J. N. Sakamuri, and N. A. Cutululis, “Blackstart from HVDC-connected offshore wind: Hard versus soft energization,” *IET Renewable Power Generation*, vol. 15, no. 1, pp. 127–138, Jan. 2021.
- [41] A. Arasteh, L. Zeni, and N. A. Cutululis, “Fault ride through capability of grid forming wind turbines: A comparison of three control schemes,” *IET Renewable Power Generation*, vol. 16, no. 9, pp. 1866–1881, Jul. 2022.
- [42] R. Ragavendran, “Control and power management of an offshore wind power plant with a diode rectifier based HVDC transmission,” Centrale Lille, 2019.
- [43] K. V. Kkuni, G. Yang, and T. Knueppel, “Analysis of the Implication of Current Limits in Grid Forming Wind Farm,” *arxiv.org*, Oct. 2021.
- [44] S. Wang, J. Hu, X. Yuan, and L. Sun, “On Inertial Dynamics of Virtual-Synchronous-Controlled DFIG-Based Wind Turbines,” *IEEE Transactions on Energy Conversion*, vol. 30, no. 4, pp. 1691–1702, Dec. 2015.
- [45] J. Hu, S. Wang, W. Tang, and X. Xiong, “Full-capacity wind turbine with inertial support by adjusting phase-locked loop response,” *IET Renewable Power Generation*, vol. 11, no. 1, pp. 44–53, 2017.
- [46] Ö. Göksu, R. Teodorescu, C. L. Bak, F. Iov, and P. C. Kjær, “Instability of wind turbine converters during current injection to low voltage grid faults and PLL frequency based stability solution,” *IEEE Transactions on Power Systems*, vol. 29, no. 4, pp. 1683–1691, 2014.

- [47] F. Bizzarri, A. Brambilla, and F. Milano, “Analytic and numerical study of TCSC devices: Unveiling the crucial role of phase-locked loops,” *IEEE Transactions on Circuits and Systems I: Regular Papers*, vol. 65, no. 6, pp. 1840–1849, Jun. 2018.
- [48] B. Wen, D. Boroyevich, R. Burgos, P. Mattavelli, and Z. Shen, “Analysis of D-Q Small-Signal Impedance of Grid-Tied Inverters,” *IEEE Transactions on Power Electronics*, vol. 31, no. 1, pp. 675–687, Jan. 2016.
- [49] D. Dong, B. Wen, D. Boroyevich, P. Mattavelli, and Y. Xue, “Analysis of phase-locked loop low-frequency stability in three-phase grid-connected power converters considering impedance interactions,” *IEEE Transactions on Industrial Electronics*, vol. 62, no. 1, pp. 310–321, Jan. 2015.
- [50] M. Ashabani, F. D. Freijedo, S. Golestan, and J. M. Guerrero, “Inducverters: PLL-Less Converters With Auto-Synchronization and Emulated Inertia Capability,” *IEEE Transactions on Smart Grid*, vol. 7, no. 3, pp. 1660–1674, May 2016.
- [51] R. Hose, A. Kuri, G. Mehlmann, R. Zurowski, D. Audring, and M. Luther, “Performance of synchronizing units under reduced system strength,” *Proceedings of 2021 IEEE PES Innovative Smart Grid Technologies Europe: Smart Grids: Toward a Carbon-Free Future, ISGT Europe 2021*, 2021.
- [52] L. Papangelis, M. S. Debry, T. Prevost, P. Panciatici, and T. Van Cutsem, “Stability of a voltage source converter subject to decrease of short-circuit capacity: A case study,” *20th Power Systems Computation Conference, PSCC 2018*, Aug. 2018.
- [53] “High Penetration of Power Electronic Interfaced Power Sources and the Potential Contribution of Grid forming Converters.” ENTSO-E Technical Group on High Penetration of Power Electronic Interfaced Power Sources, 2018, Accessed: Jun. 29, 2022. [Online]. Available: [www.entsoe.eu](http://www.entsoe.eu).
- [54] A. Engler, O. Haas, B. Kansteiner, F. Raptis, J. Sachau, and P. Zacharias, “Control of parallel working power units in expandable grids,” in *Proceedings of the 14th European Photovoltaic Solar Energy Conference*, 1994.
- [55] M. Colombino, D. Groß, J. S. Brouillon, and F. Dörfler, “Global Phase and Magnitude Synchronization of Coupled Oscillators with Application to the Control of Grid-Forming Power Inverters,” *IEEE Transactions on Automatic Control*, vol. 64, no. 11, pp. 4496–4511, Nov. 2019.
- [56] D. Groß, M. Colombino, J. S. Brouillon, and F. Dorfler, “The effect of transmission-line dynamics on grid-forming dispatchable virtual oscillator control,” *IEEE Transactions on Control of Network Systems*, vol. 6, no. 3, pp. 1148–1160, Sep. 2019.
- [57] G.-S. Seo, M. Colombino, I. Subotic, B. Johnson, D. Gross, and F. Dorfler, “Dispatchable Virtual Oscillator Control for Decentralized Inverter-Dominated Power Systems: Analysis and Experiments: Preprint; Dispatchable Virtual Oscillator Control for Decentralized Inverter-Dominated Power Systems: Analysis and Experiments: Preprint,” *2019 IEEE Applied Power Electronics Conference and Exposition (APEC)*, 2019, Accessed: Jul. 01, 2022. [Online]. Available: [www.nrel.gov/publications](http://www.nrel.gov/publications).
- [58] E. Rokrok, T. Qoria, A. Bruyere, B. Francois, and X. Guillaud, “Classification and dynamic assessment of droop-based grid-forming control schemes: Application in HVDC systems,” *Electric Power Systems Research*, vol. 189, p. 106765, Dec. 2020.
- [59] “COMMISSION REGULATION (EU) 2016/ 631, Requirements for grid connection of generators,” *Off. J. Eur. Union*. p. 68, 2016.

- [60] T. Qoria, Q. Cossart, C. Li, and X. Guillaud, "MIGRATE Project, WP3 - Control and Operation of a Grid with 100 % Converter-Based Devices, Deliverable 3.2 : Local control and simulation tools for large transmission systems," 2019, 2019. Accessed: Jul. 01, 2022. [Online]. Available: <https://www.semanticscholar.org/paper/WP-3-Control-and-Operation-of-a-Grid-with-100-3--2-Qoria-Cossart/5c5beff0d5bef78799253aae9b19f50a9cb6eb9f>.
- [61] N. Pogaku, M. Prodanović, and T. C. Green, "Modeling, analysis and testing of autonomous operation of an inverter-based microgrid," *IEEE Transactions on Power Electronics*, vol. 22, no. 2, pp. 613–625, Mar. 2007.
- [62] E. A. A. Coelho, P. C. Cortizo, and P. F. D. Garcia, "Small-signal stability for parallel-connected inverters in stand-alone ac supply systems," *IEEE Transactions on Industry Applications*, vol. 38, no. 2, pp. 533–542, Mar. 2002.
- [63] Y. A. R. I. Mohamed and E. F. El-Saadany, "Adaptive decentralized droop controller to preserve power sharing stability of paralleled inverters in distributed generation microgrids," *IEEE Transactions on Power Electronics*, vol. 23, no. 6, pp. 2806–2816, 2008.
- [64] S. V. Iyer, M. N. Belur, and M. C. Chandorkar, "A generalized computational method to determine stability of a multi-inverter microgrid," *IEEE Transactions on Power Electronics*, vol. 25, no. 9, pp. 2420–2432, 2010.
- [65] T. Qoria, E. Rokrok, A. Bruyere, B. François, and X. Guillaud, "A PLL-Free grid-forming control with decoupled functionalities for high-power transmission system applications," *IEEE Access*, vol. 8, pp. 197363–197378, 2020.
- [66] E. Rokrok, "Application of grid-forming control to HVDC interconnections," Centrale Lille, 2022.
- [67] X. Wang, M. G. Taul, H. Wu, Y. Liao, F. Blaabjerg, and L. Harnefors, "Grid-Synchronization Stability of Converter-Based Resources—An Overview," *IEEE Open Journal of Industry Applications*, vol. 1, pp. 115–134, Aug. 2020.
- [68] A. D. Paquette and D. M. Divan, "Virtual Impedance Current Limiting for Inverters in Microgrids With Synchronous Generators," *IEEE Transactions on Industry Applications*, vol. 51, no. 2, pp. 1630–1638, Mar. 2015.
- [69] T. Qoria, F. Gruson, F. Colas, G. Denis, T. Prevost, and X. Guillaud, "Critical Clearing Time Determination and Enhancement of Grid-Forming Converters Embedding Virtual Impedance as Current Limitation Algorithm," *IEEE Journal of Emerging and Selected Topics in Power Electronics*, vol. 8, no. 2, pp. 1050–1061, Jun. 2020.
- [70] T. Burton, N. Jenkins, D. Sharpe, and E. Bossanyi, "Wind Energy Handbook, Second Edition," *Wind Energy Handbook, Second Edition*, May 2011.
- [71] S. Heier, *Grid Integration of Wind Energy: Onshore and Offshore Conversion Systems*. John Wiley & Sons, Ltd, 2014.
- [72] J. K. Pedersen, K. O. Helgelsen-Pedersen, N. K. Poulsen, V. Akhmatov, and A. H. Nielsen, "Contribution to a dynamic wind turbine model validation from a wind farm islanding experiment," *Electric Power Systems Research*, vol. 64, no. 1, pp. 41–51, Jan. 2003.
- [73] J. Licari, J. Ekanayake, and I. Moore, "Inertia response from full-power converter-based permanent magnet wind generators," *Journal of Modern Power Systems and Clean Energy*, vol. 1, no. 1, pp. 26–33, Jan. 2013.
- [74] L. Sun, C. Gong, and F. Han, "Design and optimization of control parameters based on direct-drive permanent magnet synchronous generator for wind power system," *Proceedings*

- of the 2013 IEEE 8th Conference on Industrial Electronics and Applications, ICIEA 2013, pp. 1238–1243, 2013.
- [75] H. Zhang, “Analysis and performance enhancement of a series parallel offshore wind farm topology integrated into a HVDC grid,” HEI, 2017.
- [76] A. D. Hansen and I. Margaritis, “Type IV Wind Turbine Model,” Copenhagen, 2014. Accessed: Jul. 01, 2022. [Online]. Available: <https://www.semanticscholar.org/paper/Type-IV-Wind-Turbine-Model-Hansen-Margaritis/a66e3fe27bf0bcb3d997fe9324169f6dbb079bc3>.
- [77] F. Iov and F. Blaabjerg, “Power Electronics Control of Wind Energy in Distributed Power Systems,” *Renewable Energy*, Dec. 2009.
- [78] F. Blaabjerg, *Control of power electronic converters and systems*. Academic Press, 2018.
- [79] P. Tielens and D. Van Hertem, “The relevance of inertia in power systems,” *Renewable and Sustainable Energy Reviews*, vol. 55, pp. 999–1009, Mar. 2016.
- [80] Z. Wu, W. Gao, T. Gao, W. Yan, H. Zhang, S. Yan, and X. Wang, “State-of-the-art review on frequency response of wind power plants in power systems,” *Journal of Modern Power Systems and Clean Energy*, vol. 6, no. 1, pp. 1–16, Jan. 2018.
- [81] A. Avazov, “Influence of the frequency support provided by a grid-forming control-based wind turbine on the loading of its mechanical system,” 2020, Accessed: Jun. 10, 2022. [Online]. Available: [https://www.researchgate.net/publication/346625153\\_Influence\\_of\\_the\\_frequency\\_support\\_provided\\_by\\_a\\_grid-forming\\_control-based\\_wind\\_turbine\\_on\\_the\\_loading\\_of\\_its\\_mechanical\\_system](https://www.researchgate.net/publication/346625153_Influence_of_the_frequency_support_provided_by_a_grid-forming_control-based_wind_turbine_on_the_loading_of_its_mechanical_system).
- [82] HydroQuebec, “Connecting to Hydro-Québec’s system. Technical requirements, standards and codes. Connection to the system at 44 kV or more (transmission system).” <https://www.hydroquebec.com/transenergie/en/connecting-to-hydroquebec-system.html> (accessed Nov. 02, 2022).
- [83] M. Kang, J. Lee, and Y. C. Kang, “Modified stepwise inertial control using the mechanical input and electrical output curves of a doubly fed induction generator,” *9th International Conference on Power Electronics - ECCE Asia: “Green World with Power Electronics”*, ICPE 2015-ECCE Asia, pp. 357–361, Jul. 2015.
- [84] K. Liu, Y. Qu, H. M. Kim, and H. Song, “Avoiding Frequency Second Dip in Power Unreserved Control during Wind Power Rotational Speed Recovery,” *IEEE Transactions on Power Systems*, vol. 33, no. 3, pp. 3097–3106, May 2018.
- [85] J. Xi, H. Geng, and X. Zou, “Decoupling Scheme for Virtual Synchronous Generator Controlled Wind Farms Participating in Inertial Response,” *Journal of Modern Power Systems and Clean Energy*, vol. 9, no. 2, pp. 347–355, Mar. 2021.
- [86] J. Xi, H. Geng, S. Ma, Y. Chi, and G. Yang, “Inertial response characteristics analysis and optimisation of PMSG-based VSG-controlled WECS,” *IET Renewable Power Generation*, vol. 12, no. 15, pp. 1741–1747, Nov. 2018.
- [87] B. A. Bastiani and R. V. de Oliveira, “Adaptive MPPT control applied to virtual synchronous generator to extend the inertial response of type-4 wind turbine generators,” *Sustainable Energy, Grids and Networks*, vol. 27, p. 100504, Sep. 2021.
- [88] K. Gunther, B. Spichartz, and C. Sourkounis, “Influences of Virtual Inertia Control on the Mechanical Drive Train of Wind Turbines,” *2020 15th International Conference on*

- [89] A. D. Hansen and G. Michalke, "Multi-pole permanent magnet synchronous generator wind turbines' grid support capability in uninterrupted operation during grid faults," *IET Renewable Power Generation*, vol. 3, no. 3, pp. 333–348, 2009.
- [90] J. Licari, C. E. Ugalde-Loo, J. Liang, J. Ekanayake, and N. Jenkins, "Torsional damping considering both shaft and blade flexibilities," *Wind Engineering*, vol. 36, no. 2, pp. 181–195, Apr. 2012.
- [91] X. Li, H. Leng, K. Tian, X. T. Nguyen, V. H. Hoang, Y. Jiang, S. Liu, D. Zhao, and J. Cai, "A novel method of drive train damping for large wind turbines," *Journal of Physics: Conference Series*, vol. 1037, no. 3, p. 032033, Jun. 2018.
- [92] K. Szabat and T. Orłowska-Kowalska, "Vibration suppression in a two-mass drive system using PI speed controller and additional feedbacks - Comparative study," *IEEE Transactions on Industrial Electronics*, vol. 54, no. 2, pp. 1193–1206, Apr. 2007.
- [93] J. Licari, C. E. Ugalde-Loo, J. B. Ekanayake, and N. Jenkins, "Damping of torsional vibrations in a variable-speed wind turbine," *IEEE Transactions on Energy Conversion*, vol. 28, no. 1, pp. 172–180, 2013.
- [94] A. Dixit and S. Suryanarayanan, "Towards pitch-scheduled drive train damping in variable-speed, horizontal-axis large wind turbines," *Proceedings of the 44th IEEE Conference on Decision and Control, and the European Control Conference, CDC-ECC '05*, vol. 2005, pp. 1295–1300, 2005.
- [95] H. Geng, D. Xu, B. Wu, and G. Yang, "Active damping for torsional vibrations in PMSG based WECS," *Conference Proceedings - IEEE Applied Power Electronics Conference and Exposition - APEC*, pp. 2126–2131, 2010.
- [96] J. Liu, F. Zhou, C. Zhao, and Z. Wang, "Mechanism analysis and suppression strategy research on permanent magnet synchronous generator wind turbine torsional vibration," *ISA transactions*, vol. 92, pp. 118–133, Sep. 2019.
- [97] Z. Li, S. Tian, Y. Zhang, H. Li, and M. Lu, "Active Control of Drive Chain Torsional Vibration for DFIG-Based Wind Turbine," *Energies 2019, Vol. 12, Page 1744*, vol. 12, no. 9, p. 1744, May 2019.
- [98] P. Tourou, A. Broy, and C. Sourkounis, "Modelling and torque control for active minimization of drivetrain oscillations in high power wind turbines," *Proceedings of the 18th Mediterranean Electrotechnical Conference: Intelligent and Efficient Technologies and Services for the Citizen, MELECON 2016*, Jun. 2016.
- [99] L. Chen, X. Du, B. Hu, and F. Blaabjerg, "Drivetrain oscillation analysis of grid forming type-IV wind turbine," *IEEE Transactions on Energy Conversion*, pp. 1–1, 2022.
- [100] A. Avazov, F. Colas, J. Beerten, and X. Guillaud, "Damping of Torsional Vibrations in a Type-IV Wind Turbine Interfaced to a Grid-Forming Converter," *2021 IEEE Madrid PowerTech, PowerTech 2021 - Conference Proceedings*, Jun. 2021.
- [101] L. Lu, O. Saborío-Romano, and N. A. Cutululis, "Torsional oscillation damping in wind turbines with virtual synchronous machine-based frequency response," *Wind Energy*, 2022.
- [102] A. Avazov, F. Colas, J. Beerten, and X. Guillaud, "Application of input shaping method to vibrations damping in a Type-IV wind turbine interfaced with a grid-forming converter," *Electric Power Systems Research*, vol. 210, p. 108083, Sep. 2022.
- [103] A. Kamel, F. Lange, and G. Hirzinger, "New aspects of input shaping control to damp

- oscillations of a compliant force sensor,” *Proceedings - IEEE International Conference on Robotics and Automation*, pp. 2629–2635, 2008.
- [104] J. R. Huey, K. L. Sorensen, and W. E. Singhose, “Useful applications of closed-loop signal shaping controllers,” *Control Engineering Practice*, vol. 16, no. 7, pp. 836–846, Jul. 2008.
- [105] M. Schlegel and M. Goubej, “Feature-based Parametrization of Input Shaping Filters with Time Delays,” *IFAC Proceedings Volumes*, vol. 43, no. 2, pp. 247–252, Jan. 2010.
- [106] L. Li, Y. Teng, and X. Wang, “Dynamic equivalent modeling of wind farm considering the uncertainty of wind power prediction and a case study,” *Journal of Renewable and Sustainable Energy*, vol. 9, no. 1, Jan. 2017.
- [107] A. M. S. Al-Bayati, F. Mancilla-David, and J. L. Domínguez-García, “Aggregated models of wind farms: Current methods and future trends,” *NAPS 2016 - 48th North American Power Symposium, Proceedings*, Nov. 2016.
- [108] L. M. Fernández, F. Jurado, and J. R. Saenz, “Aggregated dynamic model for wind farms with doubly fed induction generator wind turbines,” *Renewable Energy*, vol. 33, no. 1, pp. 129–140, Jan. 2008.
- [109] F. Liu, J. Ma, W. Zhang, and M. Wu, “A Comprehensive Survey of Accurate and Efficient Aggregation Modeling for High Penetration of Large-Scale Wind Farms in Smart Grid,” *Applied Sciences 2019, Vol. 9, Page 769*, vol. 9, no. 4, p. 769, Feb. 2019.
- [110] L. Li, T. Wang, and X. Wang, “Dynamic equivalent modeling of wind farm with DDPMSG wind turbine generators,” *POWERCON 2014 - 2014 International Conference on Power System Technology: Towards Green, Efficient and Smart Power System, Proceedings*, pp. 2908–2914, Dec. 2014.
- [111] L. Kocewiak, “Harmonics in large offshore wind farms — Aalborg University’s Research Portal,” Aalborg University, 2012.
- [112] D. E. Kim and M. A. El-Sharkawi, “Dynamic equivalent model of wind power plant using an aggregation technique,” *IEEE Transactions on Energy Conversion*, vol. 30, no. 4, pp. 1639–1649, Dec. 2015.
- [113] M. Ding and Q. Zhu, “Equivalent modeling of PMSG-based wind power plants considering LVRT capabilities: electromechanical transients in power systems,” *SpringerPlus*, vol. 5, no. 1, pp. 1–15, Dec. 2016.
- [114] Q. Zhu, M. Ding, and P. Han, “Equivalent Modeling of DFIG-Based Wind Power Plant Considering Crowbar Protection,” *Mathematical Problems in Engineering*, vol. 2016, 2016.
- [115] W. Li, P. Chao, X. Liang, D. Xu, and X. Jin, “An Improved Single-Machine Equivalent Method of Wind Power Plants by Calibrating Power Recovery Behaviors,” *IEEE Transactions on Power Systems*, vol. 33, no. 4, pp. 4371–4381, Jul. 2018.
- [116] W. Li, P. Chao, X. Liang, J. Ma, D. Xu, and X. Jin, “A Practical Equivalent Method for DFIG Wind Farms,” *IEEE Transactions on Sustainable Energy*, vol. 9, no. 2, pp. 610–620, Apr. 2018.
- [117] N. Wang, J. Li, P. Wang, Z. Zhang, W. Hu, J. Li, and Q. Huang, “A novel method for wind farm equivalence based on multi-objective optimization,” *Asia-Pacific Power and Energy Engineering Conference, APPEEC*, vol. 2018-Octob, pp. 353–358, Dec. 2018.
- [118] W. Yi, “Applicability and Improvement of Common-Used Equivalent Methods for Wind Farms,” Accessed: Jul. 08, 2022. [Online]. Available: <https://www.semanticscholar.org/paper/Applicability-and-Improvement-of-Common->

Used-for-Yi/18de154b3651c352a438f185280610b7746e32f9.

- [119] S. Zhao, N. K. C. Nair, and N. M. Vong, "Coherency-based equivalencing method for large wind farms," *2009 IEEE Power and Energy Society General Meeting, PES '09*, 2009.
- [120] P. O. Fernandes and Â. P. Ferreira, "Probabilistic clustering of wind energy conversion systems using classification models," *Lecture Notes in Computer Science (including subseries Lecture Notes in Artificial Intelligence and Lecture Notes in Bioinformatics)*, vol. 9156, pp. 549–560, 2015.
- [121] E. Muljadi and C. P. Butterfield, "Dynamic Simulation of a Wind Farm With Variable-Speed Wind Turbines," *Journal of Solar Energy Engineering*, vol. 125, no. 4, pp. 410–417, Nov. 2003.
- [122] Q. Wei, R. G. Harley, and G. K. Venayagamoorthy, "Dynamic modeling of wind farms with fixed-speed wind turbine generators," *2007 IEEE Power Engineering Society General Meeting, PES*, 2007.
- [123] K. Luo, W. Shi, and J. Qu, "Multi-machine equivalent model parameter identification method for double-fed induction generator (DFIG)-based wind power plant based on measurement data," *The Journal of Engineering*, vol. 2017, no. 13, pp. 1550–1554, Jan. 2017.
- [124] C. Andrés García, L. M. Fernández, F. Jurado, C. Carlos, and A. García, "Evaluating reduced models of aggregated different doubly fed induction generator wind turbines for transient stabilities studies," *Wind Energy*, vol. 18, no. 1, pp. 133–152, Jan. 2015.
- [125] L. M. Fernández, C. A. García, J. R. Saenz, and F. Jurado, "Equivalent models of wind farms by using aggregated wind turbines and equivalent winds," *Energy Conversion and Management*, vol. 50, no. 3, pp. 691–704, Mar. 2009.
- [126] L. Ye, R. Rao, Y. Zhang, W. Zhong, Y. Yao, and Y. Ju, "Dynamic equivalent modeling approach of wind power plant with PMSG-WTGs," *IEEE Power and Energy Society General Meeting*, vol. 2018-Janua, pp. 1–5, Jan. 2018.
- [127] B. Djath, J. Schulz-Stellenfleth, and B. Cañadillas, "Impact of atmospheric stability on X-band and C-band synthetic aperture radar imagery of offshore windpark wakes," *Journal of Renewable and Sustainable Energy*, vol. 10, no. 4, p. 043301, Jul. 2018.
- [128] T. Ahsbahs, N. G. Nygaard, A. Newcombe, and M. Badger, "Wind Farm Wakes from SAR and Doppler Radar," *Remote Sensing 2020, Vol. 12, Page 462*, vol. 12, no. 3, p. 462, Feb. 2020.
- [129] A. Penã, P. E. Réthoré, and M. P. Van Der Laan, "On the application of the Jensen wake model using a turbulence-dependent wake decay coefficient: the Sexbierum case," *Wind Energy*, vol. 19, no. 4, pp. 763–776, Apr. 2016.
- [130] G. Hassan, "GH WindFarmer Wind Farm Design Software 4.0 Wind Energy Experts," Accessed: Aug. 08, 2022. [Online]. Available: [www.garradhassan.com](http://www.garradhassan.com).
- [131] L. Lanzilao and J. Meyers, "A new wake-merging method for wind-farm power prediction in the presence of heterogeneous background velocity fields," *Wind Energy*, vol. 25, no. 2, pp. 237–259, Feb. 2022.
- [132] A. Niayifar and F. Porté-Agel, "Analytical Modeling of Wind Farms: A New Approach for Power Prediction," *Energies 2016, Vol. 9, Page 741*, vol. 9, no. 9, p. 741, Sep. 2016.
- [133] M. Bastankhah and F. Porté-Agel, "A new analytical model for wind-turbine wakes," *Renewable Energy*, vol. 70, pp. 116–123, Oct. 2014.

- [134] X. Gao, H. Yang, and L. Lu, "Optimization of wind turbine layout position in a wind farm using a newly-developed two-dimensional wake model," *Applied Energy*, vol. 174, pp. 192–200, Jul. 2016.
- [135] L. Parada, C. Herrera, P. Flores, and V. Parada, "Wind farm layout optimization using a Gaussian-based wake model," *Renewable Energy*, vol. 107, pp. 531–541, Jul. 2017.
- [136] C. R. Shapiro, G. M. Starke, C. Meneveau, and D. F. Gayme, "A Wake Modeling Paradigm for Wind Farm Design and Control," *Energies 2019, Vol. 12, Page 2956*, vol. 12, no. 15, p. 2956, Aug. 2019.
- [137] F. Blonde and M. Cathelain, "An alternative form of the super-Gaussian wind turbine wake model," *Wind Energy Science*, vol. 5, no. 3, pp. 1225–1236, Sep. 2020.
- [138] J. Schreiber, A. Balbaa, and C. L. Bottasso, "Brief communication: A double-Gaussian wake model," *Wind Energy Science*, vol. 5, no. 1, pp. 237–244, Feb. 2020.
- [139] A. Keane, P. E. O. Aguirre, H. Ferchland, P. Clive, and D. Gallacher, "An analytical model for a full wind turbine wake," *Journal of Physics: Conference Series*, vol. 753, no. 3, p. 032039, Sep. 2016.
- [140] T. Ishihara and G. W. Qian, "A new Gaussian-based analytical wake model for wind turbines considering ambient turbulence intensities and thrust coefficient effects," *Journal of Wind Engineering and Industrial Aerodynamics*, vol. 177, pp. 275–292, Jun. 2018.
- [141] P. B. S. Lissaman, "Energy Effectiveness of Arbitrary Arrays of Wind Turbines," <https://doi.org/10.2514/3.62441>, vol. 3, no. 6, pp. 323–328, May 2012.
- [142] K. R. and A. Z. S. Voutsinas, "On the Analysis of Wake Effects in Wind Parks," 1990. <https://www.jstor.org/stable/43749429> (accessed Aug. 08, 2022).
- [143] J. A. Perez-Rua, M. Stolpe, K. Das, and N. A. Cutululis, "Global Optimization of Offshore Wind Farm Collection Systems," *IEEE Transactions on Power Systems*, vol. 35, no. 3, pp. 2256–2267, May 2020.
- [144] "Nexans - MV Underground Power Cables." <https://pl.nexans.com/en/products/Outdoor-energy-cables/MV-underground-power-cables.html> (accessed Sep. 09, 2022).
- [145] S. Ma, H. Geng, G. Yang, and B. C. Pal, "Clustering-Based Coordinated Control of Large-Scale Wind Farm for Power System Frequency Support," *IEEE Transactions on Sustainable Energy*, vol. 9, no. 4, pp. 1555–1564, Oct. 2018.
- [146] M. Ali, I. S. Ilie, J. V. Milanovic, and G. Chicco, "Wind farm model aggregation using probabilistic clustering," *IEEE Transactions on Power Systems*, vol. 28, no. 1, pp. 309–316, 2013.
- [147] S. Wierzchoń and M. Kłopotek, *Modern Algorithms of Cluster Analysis*, 1st ed. 20., vol. 34. Cham: Springer, 2018.
- [148] V. V. Srinivas, S. Tripathi, A. R. Rao, and R. S. Govindaraju, "Regional flood frequency analysis by combining self-organizing feature map and fuzzy clustering," *Journal of Hydrology*, vol. 348, no. 1–2, pp. 148–166, Jan. 2008.
- [149] F. Nie, Z. Zeng, I. W. Tsang, D. Xu, and C. Zhang, "Spectral embedded clustering: A framework for in-sample and out-of-sample spectral clustering," *IEEE Transactions on Neural Networks*, vol. 22, no. 11, pp. 1796–1808, Nov. 2011.
- [150] X. He, H. Geng, G. Yang, X. Zou, and Y. Li, "Equivalent modelling of wind farm for small-signal stability analysis in weak power system," *The Journal of Engineering*, vol. 2017, no. 13, pp. 1388–1393, Jan. 2017.

- [151] X. He, H. Geng, and G. Yang, "Dynamic Equivalent Modeling of Wind Power Plants for Various Timescale Small Signal Stability Analyses," *IEEE Power and Energy Society General Meeting*, vol. 2019-Augus, Aug. 2019.
- [152] C. Bauchage, "Lecture Notes on k-Means Clustering," 2013. Accessed: Aug. 11, 2022. [Online]. Available: [https://www.researchgate.net/publication/262800457\\_Lecture\\_Notes\\_on\\_k-Means\\_Clustering\\_I](https://www.researchgate.net/publication/262800457_Lecture_Notes_on_k-Means_Clustering_I).
- [153] C. Broderick, "Rate of Change of Frequency (RoCoF) withstand capability," ENTSO-E, Brussels, Tech. Rep., 2018. Accessed: Aug. 25, 2022. [Online]. Available: [https://energy-charts.de/power\\_de.htm](https://energy-charts.de/power_de.htm).
- [154] M. Sarkar, M. Altin, P. E. Sørensen, and A. D. Hansen, "Reactive Power Capability Model of Wind Power Plant Using Aggregated Wind Power Collection System," *Energies* 2019, Vol. 12, Page 1607, vol. 12, no. 9, p. 1607, Apr. 2019.

# **Appendices**

## Appendix A. Grid-forming control with new current limitation

As demonstrated in Chapter 1 and repeated in Fig. A.1, the voltage reference generation in a grid-forming control can be implemented with a combination of the TVR, the VI and the CSA. The TVR is responsible for the damping of the grid poles, while the VI and the CSA are for the current limitation.

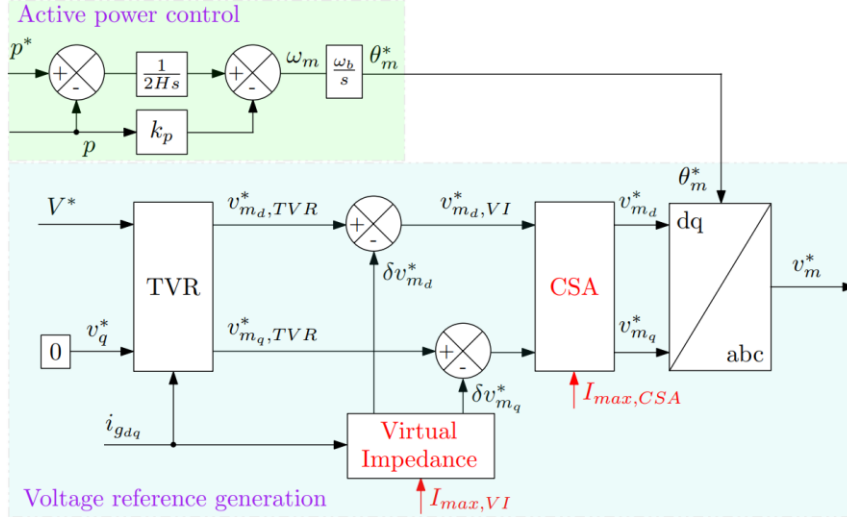


Fig. A.1. Grid-forming control with TVR, VI and CSA

There is also another possibility to implement a grid-forming control. The idea is to add a quasi-static model of the converter connection impedance in order to obtain the current references. In its turn, current references can be treated by the current limitation block and then converted to the voltage references with a current controller. The grid-forming control in such form is shown in Fig. A.2.

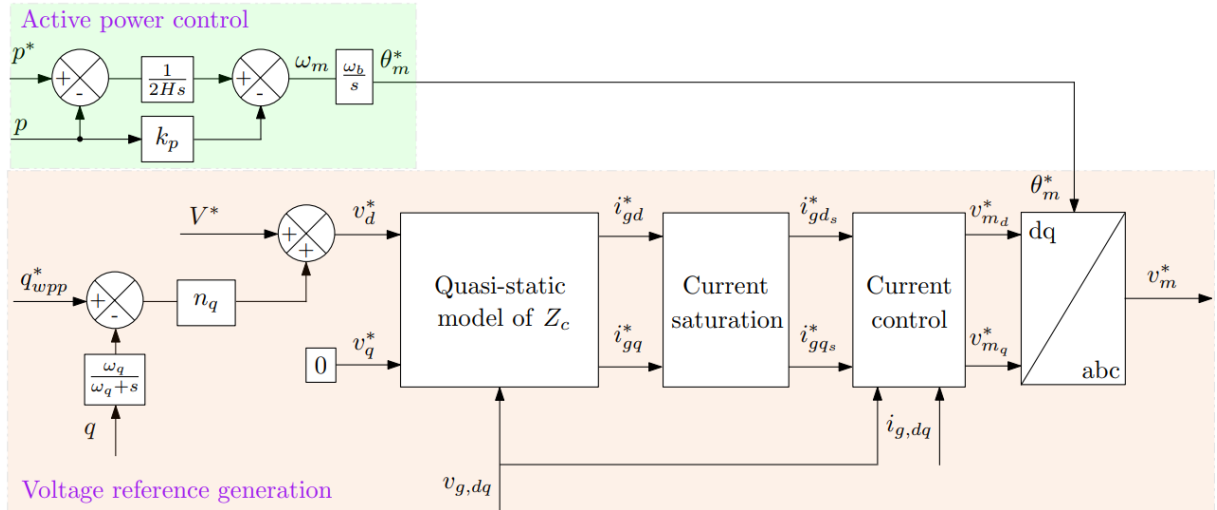


Fig. A.2. Grid-forming control with a quasi-static model of a converter connection impedance

The quasi-static model can be expressed as:

$$\begin{pmatrix} i_{gd}^* \\ i_{gq}^* \end{pmatrix} = \begin{pmatrix} r_c & -x_c \\ x_c & r_c \end{pmatrix}^{-1} \begin{pmatrix} v_{md}^* - v_{gd} \frac{\omega_f}{s + \omega_f} \\ v_{mq}^* - v_{gq} \frac{\omega_f}{s + \omega_f} \end{pmatrix} \quad (\text{A.1})$$

As it is shown in Equation A.1, the measurement of the grid voltage is processed with a LPF.

In order to limit the output converter current, the current saturation is added between the quasi-static model and the current control. The logic of the current saturation block is the following:

$$\text{if } \sqrt{i_{gd}^{*2} + i_{gq}^{*2}} > I_{sat} \rightarrow \text{sat} = 1 \quad (\text{A.2})$$

$$\text{if } \text{sat} = 1 \rightarrow \begin{cases} i_{gd_s}^* = \frac{i_{gd}^*}{\sqrt{i_{gd}^{*2} + i_{gq}^{*2}}} I_{sat} \\ i_{gq_s}^* = \frac{i_{gq}^*}{\sqrt{i_{gd}^{*2} + i_{gq}^{*2}}} I_{sat} \end{cases} \quad (\text{A.3})$$

$$\text{if } \text{sat} = 0 \rightarrow \begin{cases} i_{gd_s}^* = \frac{i_{gd}^*}{\sqrt{i_{gd}^{*2} + i_{gq}^{*2}}} I_{sat} \\ i_{gq_s}^* = \frac{i_{gq}^*}{\sqrt{i_{gd}^{*2} + i_{gq}^{*2}}} I_{sat} \end{cases}$$

The current loop in Fig. A.2 generates the voltage references and allows damping the grid poles, so the transient virtual resistance (TVR) is not required. The current controller has to be very fast in order to keep controlling the active power with the voltage angle,  $\theta_m$ .

The current controller can be described with the following equations:

$$v_{mdq}^* = (i_{gdq}^* - i_{gdq}) K_{pcc} \mp x_c i_{gdq} + v_{gdq} \quad (\text{A.4})$$

where  $K_{pcc} = \frac{3x_c}{\tau_{cc}}$  is the proportional gain,  $\tau_{cc}$  is the settling time.

Moreover, the reactive power droop is added to the voltage set-point generation. It includes the filtered measurement of the reactive power and the reactive power reference that comes from a centralized reactive power controller explained in Appendix .

## Appendix B. Centralized reactive power control

A centralized reactive power controller is used in order to involve wind turbines in the task of the voltage support. The controller defines the reactive power to supply to the grid and then commands GSCs of each wind turbine to provide a part of the total demand.

Such a controller can be implemented with a classical combination of a Q(V) droop and a PI controller as shown in Fig. B.1. The droop regulator generates the reactive power reference,  $q_{pcc}^*$ , that has to be supplied to the PCC. To command each GSC of a wind turbine to provide a certain amount of reactive power, it is also necessary to take the reactive power losses in the main transformers into account. For this reason, a PI controller is added to generate the reactive power reference,  $q_{wpp}^*$ , that is to be delivered to the WPP bus.

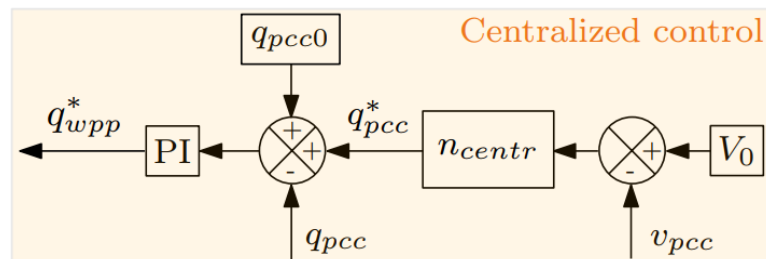


Fig. B.1. Centralized reactive power controller

The parameters of the centralized controller are provided in Chapter 3.

However, since each GSC has its own current and voltage limits, the centralized controller also has to include the limitation of the reactive power reference. The block diagram of the controller is modified in Fig. B.2.

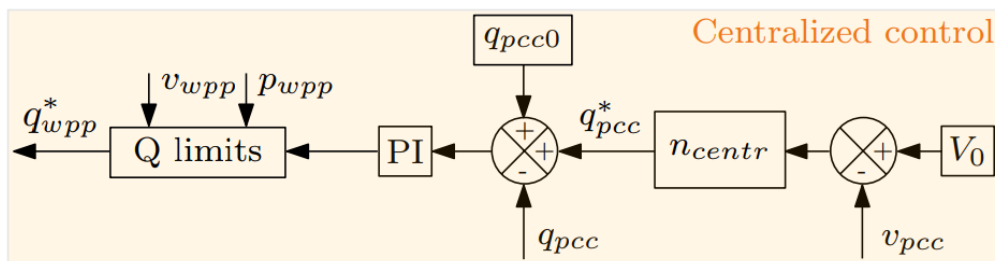


Fig. B.2. Centralized reactive power controller with limits

These limits can be derived in real-time for a specific operating point. They depend on the bus voltage and the active power supplied. Usually, the combination of the voltage and current limits forms a PQ capability diagram. The process of deriving a PQ diagram is exemplified as follows.

- **Derivation of a PQ diagram for a wind turbine.**

The GSC of a grid-connected wind turbine has its limits related to a) voltage and b) current. These limits form the shape of a PQ diagram at the point of the wind turbine connection.

- a) GSC voltage limit

As presented in Chapter 1, the GSC is connected to the grid with a connection impedance that is a step-up transformer. The converter voltage at the LV side is  $V_m$ , and the voltage at the HV side is  $V_g$ . The impedance of a transformer is  $Z_c = R_c + jX_c$ .

The active and reactive power supplied to the HV side and its relationship with voltage and current are expressed as:

$$P + jQ = V_g e^{j\theta_g} I^* \quad (\text{B.1})$$

where  $\theta_g$  is the voltage angle at the HV side,  $I$  is the current flow through a connection impedance.

From Equation B.1 the current flowing to the HV side is defined as:

$$I = \frac{V_m e^{j\theta_m} - V_g e^{j\theta_g}}{Z_t} \quad (\text{B.2})$$

Combining Equations B.1 and B.2, the following relation can be obtained:

$$\left( P + \frac{V_g R_t}{R_t^2 + X_t^2} \right)^2 + \left( Q + \frac{V_g^2 X_t}{R_t^2 + X_t^2} \right)^2 = \left( \frac{V_g V_m}{\sqrt{R_t^2 + X_t^2}} \right)^2 \quad (\text{B.3})$$

By rearranging Equation B.3, the reactive power output constrained by the converter voltage can be expressed as a relation of the active power, the voltage at the LV side, and the voltage at the HV side:

$$Q_V = \sqrt{\left( \frac{V_g V_m}{\sqrt{R_t^2 + X_t^2}} \right)^2 - \left( P + \frac{V_g R_t}{R_t^2 + X_t^2} \right)^2} - \frac{V_g^2 X_t}{R_t^2 + X_t^2} \quad (\text{B.4})$$

From Equation B.4 it is then possible to derive the maximum reactive power that can be injected or absorbed by the GSC of a wind turbine taking into account fixed limits of the converter voltage by substituting  $V_m$  with a minimum and maximum converter voltage.

$$Q_{V,inj,max} = \sqrt{\left( \frac{V_g V_{m,max}}{\sqrt{R_t^2 + X_t^2}} \right)^2 - \left( P + \frac{V_g R_t}{R_t^2 + X_t^2} \right)^2} - \frac{V_g^2 X_t}{R_t^2 + X_t^2} \quad (\text{B.5})$$

$$Q_{V,abs,max} = \sqrt{\left( \frac{V_g V_{m,min}}{\sqrt{R_t^2 + X_t^2}} \right)^2 - \left( P + \frac{V_g R_t}{R_t^2 + X_t^2} \right)^2} - \frac{V_g^2 X_t}{R_t^2 + X_t^2} \quad (\text{B.6})$$

#### b) GSC current limit

Considering the maximum current of the GSC, the relation of the active and reactive power at the HV side can be expressed as:

$$P + jQ = (V_g I_{max})^2 \quad (B.7)$$

where  $I_{max}$  is the maximum allowable GSC current.

Hence, the reactive power limitation due to maximum converter current can be acquired in the form below:

$$Q_I = \pm \sqrt{(V_g I_{max})^2 - P^2} \quad (B.8)$$

From Equation E.8, the maximum reactive power injection and absorption are presented:

$$Q_{I,inj,max} = \sqrt{(V_g I_{max})^2 - P^2} \quad (B.9)$$

$$Q_{I,abs,max} = -\sqrt{(V_g I_{max})^2 - P^2} \quad (B.10)$$

Considering that the voltage at HV side is  $V_g = 1 pu$  and the active power interval is in between 0.1 – 1 pu, the voltage and current limits can be drawn as in Fig. B.3.

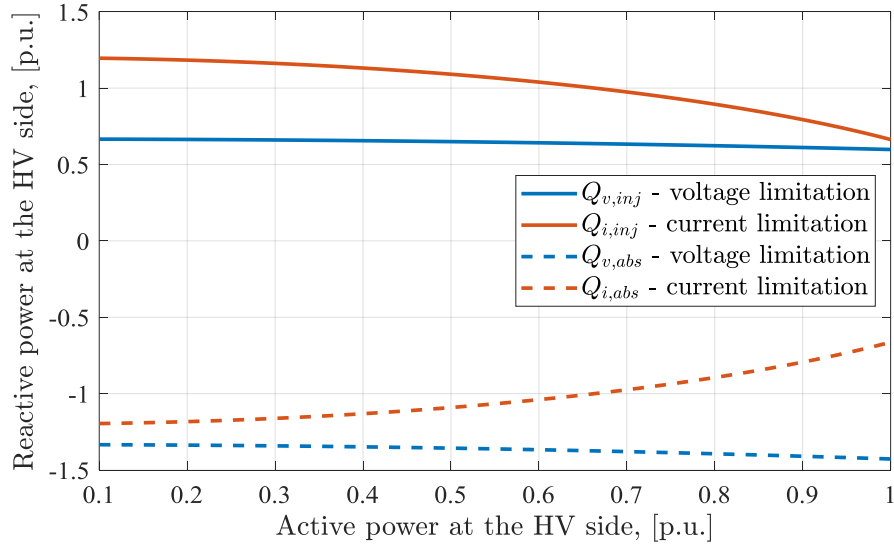


Fig. B.3. Voltage and current limits at HV side with  $V_g = 1 pu$

As can be seen from Fig. B.3, the reactive power injection is mostly impacted by the converter voltage limit whereas the reactive power absorption depends on the current limit. Voltage and current limits can be combined in order to calculate the PQ capability diagram at the HV side:

$$Q_{inj,max} = \min (Q_{V,inj,max}, Q_{I,inj,max}) \quad (B.11)$$

$$Q_{abs,max} = \max (Q_{V,abs,max}, Q_{I,abs,max}) \quad (B.12)$$

The PQ diagram at the HV side of the wind turbine package transformer is shown in Fig. B.4.



$$Q_{abs,max} = \max(Q_{V,abs,max}, Q_{I,abs,max}) + V_{wpp}^2 B_{cab,eq} \quad (\text{B.14})$$

where  $B_{cab,eq} = C_{eq}\omega_b$  is the collector network' susceptance.

The PQ diagram at the WPP bus is presented in Fig. B.6 with  $V_{wpp} = 1 pu$ . As it can be noticed, the reactive power limits do not significantly differ from the PQ diagram of a single wind turbine. This is because the electrical topology of the collector network has a minor influence on the reactive power losses in a WPP.

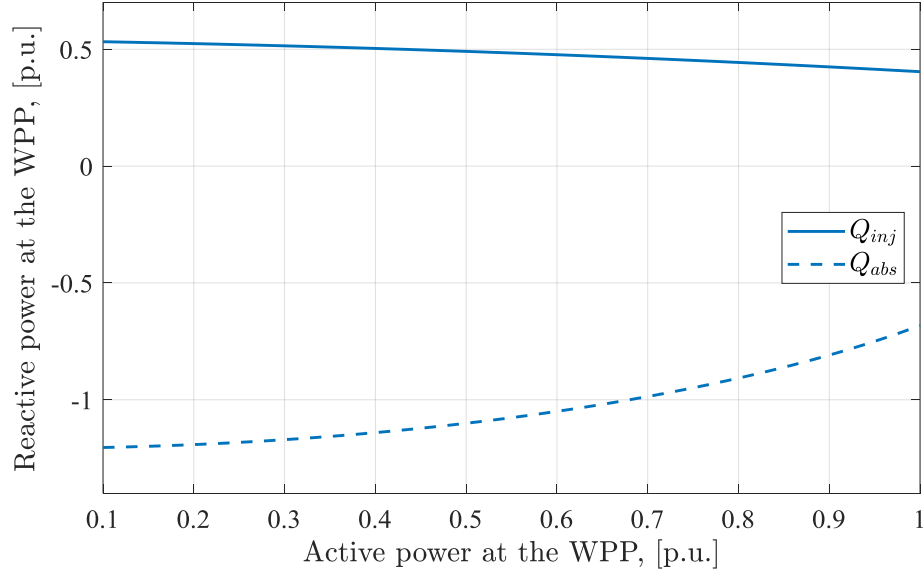


Fig. B.6. PQ capability diagram at the WPP bus with  $V_{wpp} = 1 pu$

The described PQ capability diagram is a very useful tool to estimate the available reactive power that can be potentially supplied or absorbed from the grid if needed. As explained, it can also be deployed to limit the reactive power reference generated by a centralized reactive power controller. The derived PQ capability diagram shows the theoretical limits of a WPP. The theoretical limits of a WPP' PQ diagram have to cover the requirements defined in the grid codes of a specific TSO. So, usually the power references limitations of centralized power controllers rely on the grid code-defined PQ capability diagram. Nevertheless, in this thesis, the limitations of the centralized reactive power controller rely on the theoretical limits defined as in Fig. B.6.

## **AC Connection of Wind Farms to Transmission System: from Grid-Following to Grid-Forming**

Wind power plants (WPPs) constitute a significant share of the renewable energy sources interfaced to the grid with a power electronic converter. Till now, nearly all of these converters are connected to the grid in grid-following mode. Over the next years, at least some of them, are expected to switch to grid-forming mode.

The grid-forming control differs from a classical grid-following control. Therefore, in order to make a Type-4 wind turbine function in grid-forming mode, a significant modification in the control configuration of the back-to-back converter is required. This appropriate control modification in turn creates a strong coupling between the grid-forming converter and the mechanical part of the wind turbine. This coupling induces several negative effects on the operation of the wind turbine. The major effect is a fast variation of the generator' electromagnetic torque, resulting in increased torsional vibrations induced in the wind turbine drivetrain. Therefore, to mitigate this effect, the impact of the grid-forming control on the wind turbine is investigated and possible solutions for vibration damping are proposed.

A grid-forming WPP is an interesting mean to improve power system stability. However, to analyze a grid-forming WPP connected to a transmission system, the use of its dynamic equivalent model is typically required. Standard equivalent models cannot be reliable in all possible wind conditions. For this reason, in this thesis, the aggregation of a WPP is developed by taking into account the heterogeneous nature of the wind distribution within a WPP. In addition, an algorithm that recommends the equivalent model to be used in each wind condition is proposed. The verification of the aggregation methodology and the recommendation algorithm is carried out on the case study of an existing WPP.

**Keywords:** transmission network, grid-forming, wind turbines, vibrations damping, wind farm, aggregation

## **Connexion en AC de grandes fermes éoliennes au réseau de transport: d'un raccordement en source de courant au raccordement en source de tension**

Des centrales éoliennes (WPPs) constituent une part significative des sources d'énergies renouvelables interfacées au réseau électrique avec les convertisseurs électroniques de puissance. Jusqu'à présent, presque tous ces convertisseurs sont connectés au réseau en mode de fonctionnement appelé grid-following. Dans les années à venir, au moins certains d'entre eux passeront au mode de fonctionnement appelé grid-forming.

Le contrôle d'un convertisseur en grid-forming est différent d'un contrôle classique en grid-following. Par conséquent, afin de faire fonctionner une éolienne de Type-4 en grid-forming, il est nécessaire de modifier la configuration de commande du convertisseur en tête-bêche. La modification appropriée de la commande crée un fort couplage entre le convertisseur grid-forming et la partie mécanique de l'éolienne. Ce couplage induit plusieurs effets négatifs sur le fonctionnement de l'éolienne. Le principal effet est la variation rapide du couple électromagnétique de la génératrice, qui entraîne une augmentation des vibrations de torsion induites dans le système d'entraînement mécanique d'une éolienne. Afin d'atténuer cet effet, l'impact d'un contrôle grid-forming sur une éolienne est étudié et des solutions possibles pour l'amortissement des vibrations sont proposées.

Une WPP grid-forming est un moyen intéressant d'améliorer la stabilité du système électrique. Cependant, pour analyser une WPP connecté au réseau de transport d'électricité, il est nécessaire d'utiliser son modèle équivalent dynamique. Les modèles standard équivalents ne peuvent pas être fiables dans toutes les conditions de vent possibles. Pour cette raison, dans cette thèse, l'agrégation d'une WPP est développée en tenant compte de la nature hétérogène de la distribution du vent. De plus, l'algorithme qui recommande le modèle équivalent optimal à utiliser dans chaque condition de vent est proposé. La vérification de la méthodologie d'agrégation et de l'algorithme de recommandation d'un modèle équivalent optimal est effectuée sur l'étude de cas d'une WPP existant.

**Mots-clés** : réseau de transport d'électricité, grid-forming, éoliennes, amortissement des vibrations, parc éolien, agrégation